



National Library
of Canada

Acquisitions and
Bibliographic Services Branch

395 Wellington Street
Ottawa, Ontario
K1A 0N4

Bibliothèque nationale
du Canada

Direction des acquisitions et
des services bibliographiques

395, rue Wellington
Ottawa (Ontario)
K1A 0N4

Your file Votre référence

Our file Notre référence

NOTICE

The quality of this microform is heavily dependent upon the quality of the original thesis submitted for microfilming. Every effort has been made to ensure the highest quality of reproduction possible.

If pages are missing, contact the university which granted the degree.

Some pages may have indistinct print especially if the original pages were typed with a poor typewriter ribbon or if the university sent us an inferior photocopy.

Reproduction in full or in part of this microform is governed by the Canadian Copyright Act, R.S.C. 1970, c. C-30, and subsequent amendments.

AVIS

La qualité de cette microforme dépend grandement de la qualité de la thèse soumise au microfilmage. Nous avons tout fait pour assurer une qualité supérieure de reproduction.

S'il manque des pages, veuillez communiquer avec l'université qui a conféré le grade.

La qualité d'impression de certaines pages peut laisser à désirer, surtout si les pages originales ont été dactylographiées à l'aide d'un ruban usé ou si l'université nous a fait parvenir une photocopie de qualité inférieure.

La reproduction, même partielle, de cette microforme est soumise à la Loi canadienne sur le droit d'auteur, SRC 1970, c. C-30, et ses amendements subséquents.

UNIVERSITY OF ALBERTA

Processes and Simulation for Advanced Integrated Circuit Metallization

BY

Steven K. Dew



A thesis submitted to the Faculty of Graduate Studies and Research in partial fulfillment of the requirements for the degree of Doctor of Philosophy

DEPARTMENT OF ELECTRICAL ENGINEERING

Edmonton, Alberta

Fall 1992



National Library
of Canada

Acquisitions and
Bibliographic Services Branch

395 Wellington Street
Ottawa, Ontario
K1A 0N4

Bibliothèque nationale
du Canada

Direction des acquisitions et
des services bibliographiques

395, rue Wellington
Ottawa (Ontario)
K1A 0N4

Your file *Votre référence*

Our file *Notre référence*

The author has granted an irrevocable non-exclusive licence allowing the National Library of Canada to reproduce, loan, distribute or sell copies of his/her thesis by any means and in any form or format, making this thesis available to interested persons.

L'auteur a accordé une licence irrévocable et non exclusive permettant à la Bibliothèque nationale du Canada de reproduire, prêter, distribuer ou vendre des copies de sa thèse de quelque manière et sous quelque forme que ce soit pour mettre des exemplaires de cette thèse à la disposition des personnes intéressées.

The author retains ownership of the copyright in his/her thesis. Neither the thesis nor substantial extracts from it may be printed or otherwise reproduced without his/her permission.

L'auteur conserve la propriété du droit d'auteur qui protège sa thèse. Ni la thèse ni des extraits substantiels de celle-ci ne doivent être imprimés ou autrement reproduits sans son autorisation.

ISBN 0-315-77420-7

Canada



GENUS

Steve Dew,
238 Civil/Electrical Building
Department of Electrical Engineering
University of Alberta
Edmonton

August 31, 1992

Re: Reprint permission

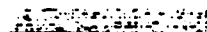
Dear Steve,

I checked with my publisher for reprint allowance of figure 2.16 out of the book Chemical Vapor Deposition of Tungsten and Tungsten Silicides for VLSI/ULSI Applications in your PhD thesis. Mr. George Narita from Noyes Publications has no problem with this as long you reference the book in an appropriate fashion.

If possible I would like to obtain a copy of relevant chapters of your thesis which may be of importance for future reprints of the book.

Sincerely yours,

John E.J. Schmitz, Ph.D.


THIN FILM DIVISION

Genus, Inc.
515 Ellis Street
Mountain View, CA 94043
TEL 415-960-1120
FAX 415-961-0614

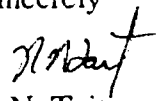
S.K. Dew,
Dept. Electrical Engineering
University of Alberta
Edmonton, AB, Canada
T6G 2G7

September 1, 1992

Dear Mr. Dew,

I hereby grant you permission to reproduce Figure 1.5 from my Ph.D. thesis from the University of Alberta, and to make use of the figure in your own thesis.

Sincerely



R.N. Tait

UNIVERSITY OF ALBERTA

RELEASE FORM

NAME OF AUTHOR: Steven K. Dew

TITLE OF THESIS: Processes and Simulation for Advanced Integrated Circuit
Metallization

DEGREE: Doctor of Philosophy

YEAR THIS DEGREE GRANTED: 1992

Permission is hereby granted to the University of Alberta Library to reproduce single copies of this thesis and to lend or sell such copies for private, scholarly or scientific research purposes only.

The author reserves all other publication and other rights in association with the copyright in the thesis, and except as hereinbefore provided neither the thesis nor any substantial portion thereof may be printed or otherwise reproduced in any material form whatever without the author's prior written permission.



Steven K. Dew

1214 Bednesti Crescent

Prince George, B.C.

V2M 4E9

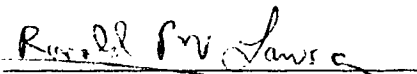
August 31, 1992

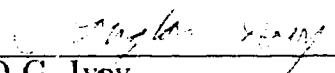
UNIVERSITY OF ALBERTA

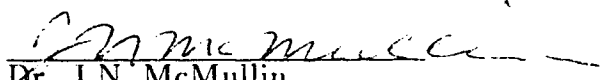
FACULTY OF GRADUATE STUDIES AND RESEARCH

The undersigned certify that they have read, and recommend to the Faculty of Graduate Studies and Research for acceptance, a thesis entitled Processes and Simulation for Advanced Integrated Circuit Metallization submitted by Steven K. Dew in partial fulfillment of the requirements for the degree of Doctor of Philosophy.


Dr. M.J. Brett


Dr. R.P.W. Lawson


Dr. D.G. Ivey


Dr. J.N. McMullin


Dr. D.J. Thomson

August 24, 1992

Abstract

As microelectronic device dimensions continue to scale to smaller sizes, metallization faces ever greater challenges arising from the degradation of step coverage, the increase in electromigration, and the growing importance of the intrinsic microstructure of the metal films. In order to meet some of these challenges, a number of advanced metallization processes have been proposed involving optimized sputter distributions, bias sputtering, high temperature deposition, or metal chemical vapour deposition. Each of these processes has both advantages and limitations which must be better understood before it can be applied in a production environment.

In order to facilitate this understanding, this thesis presents the development of thin film growth simulation tools suitable for studying and optimizing several of the advanced metallization techniques. Specifically discussed are the development of the SIMSPUD simulation for predicting realistic sputter distributions and the extension of the SIMBAD model to alloy sputtering, bias sputtering, high temperature deposition, and refractory metal chemical vapour deposition. Experimental verification of each of these models is presented along with examples of applications for each of the advanced metallization processes mentioned above.

Acknowledgement

First, I must express my gratitude to my research supervisor, Dr. M.J. Brett. He was always present when ideas and guidance were needed, but also willing to let me pursue my own directions. Also instrumental were the assistance and encouragement of Dr. T. Smy of Carleton University and Dr. R.N. Tait (now at the Alberta Microelectronic Centre). In addition, the assistance of Graham McKinnon, Alan Mitchell, Glen Fitzpatrick, Yan Loke and the other staff of the Alberta Microelectronic Centre were of considerable importance. Much of this work depends on the very high quality electron microscopy performed by George Braybrook, whom I must also acknowledge.

I am grateful for the constant moral support from my family and friends, and especially from Leslie Grant. Finally, I would like to thank the Alberta Microelectronic Centre, the Natural Sciences and Engineering Research Council, the University of Alberta, the Alberta Heritage Fund, and the Micronet Network of Centres of Excellence for their generous financial support, as well as Professors R.P.W. Lawson and D.G. Ivey for their helpful discussions and ideas.

Table of Contents

1	Introduction	1
1.1	Metallization	2
1.2	Metallization Techniques	5
1.3	Scaling Metallization to Smaller Dimensions	8
1.4	Film Microstructure	11
1.4.1	Origin of Microstructure	15
1.5	Advanced Metallization Techniques	18
2	Simulation of Thin Film Deposition	20
2.1	Types of Models	22
2.1.1	Molecular Dynamics	22
2.1.2	Atomistic Models	23
2.1.3	String Algorithms	23
2.1.4	Continuum Models	25

2.1.5	Ballistic Deposition	25
2.2	SIMBAD	26
3	Sputter Distributions	32
3.1	Introduction	32
3.2	Sputter Distributions and Film Properties	33
3.3	The SIMSPUD Model	35
3.3.1	Algorithmic Details	42
3.4	Experimental Verification of SIMSPUD	45
3.5	Applications of SIMSPUD	50
3.5.1	Target-Substrate Separation	50
3.5.2	Swept Field Magnetrons	55
3.5.3	Alloy Sputtering	58
3.6	Summary	61
4	Bias Sputtering	62
4.1	Introduction	62
4.2	SIMBAD Bias Sputtering Model	66
4.3	Experimental Verification	73

4.4	Applications of SIMBAD Bias Sputtering Model	82
4.4.1	Effects of Bias Voltage	82
4.4.2	Effects of Target-Substrate Separation	83
4.4.3	Initial Protective Layer Use	85
4.5	Summary	87
5	High Temperature Deposition	88
5.1	Introduction	88
5.2	SIMBAD High Temperature Model	89
5.2.1	Capillarity	90
5.2.2	Assumptions	92
5.3	Model Verification	93
5.4	Applications of SIMBAD High Temperature Model	97
5.4.1	Temperature and Step Coverage	98
5.4.2	Effect of Aspect Ratio	99
5.4.3	High Temperature Bias Sputtering	101
5.5	Summary	103
6	Refractory Chemical Vapour Deposition	104

6.1	Introduction	104
6.2	CVD Microstructure	108
6.3	SIMBAD CVD Model	110
6.3.1	Sticking Coefficient	111
6.3.2	Incident Angular Distribution	112
6.4	Model Verification	115
6.5	Applications of SIMBAD CVD	119
6.5.1	Effects of Sticking Coefficient	119
6.5.2	Effects of Pressure	122
6.5.3	Selective Deposition	123
6.6	Summary	125
7	Conclusions and Recommendations	126
7.1	Conclusions	126
7.1.1	Sputter Distributions	126
7.1.2	Bias Sputtering	127
7.1.3	High Temperature Deposition	128
7.1.4	Refractory Metal CVD	128

7.2 Recommendations for Further Work	129
Bibliography	131
Appendices	151
A Quasi-3D SIMBAD	151
E SIMSPUD Program Organization	157
C SIMBAD Program Organization	159

List of Tables

1.1	Scale of Integration	1
3.2	Conditions for Pinhole Experiments	47
4.3	Bias Sputtering Deposition Conditions	74
6.4	CVD Tungsten Deposition Conditions	117

List of Figures

1.1	Trend in Minimum Feature Size	3
1.2	Conventional Metallization Scheme	4
1.3	DC Magnetron Sputtering System	7
1.4	Step Coverage Definition	9
1.5	Step Coverage vs. Feature Size	10
1.6	Planarized Multilevel Scheme	12
1.7	Examples of Film Microstructure	13
1.8	Structure Zone Models	17
2.9	SAMPLE Depiction	24
2.10	SIMBAD Algorithm	27
2.11	Anomalous Facetting	29
2.12	SIMBAD Output	31
3.13	Effects of Angular Distribution on Film Properties	34

3.14	Diagram of SIMSPUD Algorithm	37
3.15	Diagram of Collision	39
3.16	Dependence of Cross-Section on Energy	41
3.17	Coordinate Transform to Project to Two Dimensions	43
3.18	Pinhole Experiment Setup	46
3.19	Pinhole Experiment Results for Aluminum	48
3.20	Pinhole Experiment Results for Copper	49
3.21	Film Thickness Uniformity	51
3.22	Relative Deposition Rate	52
3.23	Step Coverage Effects	53
3.24	Mean Incident Energy	54
3.25	Swept Magnetron Film Thickness Uniformity	56
3.26	Off-Axis Deposition	57
3.27	Compositional Variation Over Topography	59
3.28	Compositional Variation Across the Wafer	60
4.29	Effects of Resputtering	63
4.30	Description of Bias Sputtering	65

4.31 Ion Trenching	68
4.32 Angular Dependence of Sputter Yield	69
4.33 Resputter Emission Angular Distribution	70
4.34 Surface Normal Algorithm	72
4.35 Deposition Rate vs. Bias Voltage	75
4.36 Deposition Rate vs. Ion Flux	76
4.37 Tungsten Film Without Bias	77
4.38 Tungsten Film With Bias	78
4.39 Thicker Film With Bias	80
4.40 Ion Damage	81
4.41 Step Coverage vs. Bias Voltage	83
4.42 Step Coverage vs. Target-Substrate Separation	84
4.43 Step Coverage vs. Protection Layer Thickness	86
5.44 Surface Potential Search	91
5.45 Effect of Temperature	95
5.46 Effect of Temperature on Fill Factor	97
5.47 Effect of Temperature on Step Coverage	98

5.48 Effect of Aspect Ratio at High Temperature	100
5.49 High Temperature Bias Sputtering	102
6.50 Single Wafer CVD Reactor	105
6.51 Tungsten Plug Technology	107
6.52 Coordinate Transform to Project to Two Dimensions	115
6.53 Comparison Between Experiment and SIMBAD CVD	116
6.54 Effect of Sticking Coefficient	120
6.55 Coverage vs. Sticking Coefficient	121
6.56 Effect of Pressure	123
6.57 Selective Deposition	124
A.58 Quasi-3D Projection Geometry	152
A.59 Quasi-3D Via Result	155
A.60 Quasi-3D Trench Result	156
B.61 SIMSPUD Program Sequence	153
C.62 SIMBAD Program Sequence	161

List of Symbols

SIMBAD	-	SIMulation by BALListic Deposition
SIMSPUD	-	SIMulation of SPUtter Distributions
VLSI	-	Very Large Scale Integration
ULSI	-	Ultra Large Scale Integration
SEM	-	Scanning Electron Microscope
UHV	-	Ultra High Vacuum
CVD	-	Chemical Vapour Deposition
rf,dc	-	radio frequency, direct current
T_m	-	melting temperature
ζ	-	column orientation angle
Ω	-	solid angle
ρ	-	radial position in cylindrical coordinates
ϕ	-	azimuthal position angle in cylindrical coordinates
θ	-	incident flux direction angle from the vertical
$f_{\Theta}(\theta)d\theta$	-	incident flux angular distribution
γ	-	azimuthal direction angle (Ch. 3,6)
	-	surface energy (tension) (Ch. 5)
$S(\rho)$	-	sputter target erosion profile
λ	-	free path between collisions
λ_m	-	mean free path between collisions

σ	- collision cross-section
E, E_i	- particle and ion energies
E_b	- binding energy
$f_P, f_\Omega, f_E, f_\Lambda$	- spatial, trajectory, energy, and free path distributions
m, m_g	- sputtered and gas particle masses
r, r_g	- sputtered and gas particle radii
$g(\theta)d\theta$	- emission angular distribution
$a, (d)$	- impact parameter (maximum)
V_t, V_b	- target and substrate bias voltages
$\alpha, (\alpha_{cm})$	- polar scattering angle (centre-of-mass frame)
β	- azimuthal scattering angle
p	- gas pressure
kT	- thermal energy
ξ	- a uniform random value between 0 and 1
Γ_f, Γ_i	- film and ion disc flux
$D, (D_o)$	- (intrinsic) diffusivity
Q_s	- activation energy for surface diffusion
τ	- effective lifetime of mobile particle on film surface
L	- surface diffusion length
$\mu, (\mu_o)$	- chemical potential (of a flat surface)
V	- atomic volume
κ	- surface curvature
\hat{e}	- surface normal
ℓ	- surface path length

s	- sticking coefficient
R_d, R_i, R_r	- desorption, impingement, and reaction rates
\mathcal{F}	- flux density
h	- height above substrate
$G(h)$	- scattering density
$n(h)$	- number density
J	- diffusion current
η	- two dimensional projection angle

Chapter 1

Introduction

Since the invention of the transistor in 1947, [1] the application of microelectronics has become one of the most potent technological forces in modern society. This ongoing phenomenon has been driven by the dramatic improvement in integrated circuit capabilities. As more and more components are fabricated onto a single silicon 'chip', it becomes capable of more sophisticated functions and can be produced at lower cost per function. Table 1.1 charts the progression from Kilby's first integrated circuit in 1958 [1] through successive stages of integration until today, with the start of production of 16 megabit memory chips by IBM, [2] we are at the beginning of ultra large scale integration (ULSI). [5,8]

Year	Scale of Integration	Number of Components
1958	small (SSI)	1-10
1962	medium (MSI)	$10-10^3$
1969	large (LSI)	10^3-10^5
1975	very large (VLSI)	10^5-10^7
1992	ultra large (ULSI)	10^7+

Table 1.1: Scale of integration, number of corresponding components and approximate year of achievement. There is considerable diversity in the definitions of the transition points between the classes of integration. [3-7] Because of this, rounded median values are used in this table.

These increased capabilities have only been possible through a sustained improvement in manufacturing technology – especially with respect to reducing the size of features on the integrated circuit. Figure 1.1 illustrates the exponential decrease in the minimum feature size over the last three decades which improvements in manufacturing have enabled. The benefits of such miniaturization include not only increased density and functionality, but also increased speed and reduced cost per function. [3]

It is almost taken for granted that this dramatic trend will continue over the next decade [8] which implies reaching features of $0.1 - 0.2 \mu\text{m}$ by the year 2000. However, extending conventional manufacturing techniques toward this goal will become increasingly difficult. An obvious example of this is the use of optical lithography which is approaching the fundamental limits of the wavelengths of light used. [9] In fact, sustaining the trend of scaling to smaller dimensions presents challenges in almost all areas of microelectronics fabrication. One area where this is especially true is metallization, [10] which is the principle focus of this thesis.

1.1 Metallization

Metallization is the task of depositing the conductive materials that provide inputs, outputs, power, and interconnections to the active devices of an integrated circuit. [18] This requires choosing the optimal combination of both material and deposition process for every aspect of this task. Figure 1.2 shows a hypothetical multilevel metallization structure which demonstrates many of the elements of metallization such as contact layers, barrier layers, gates, contact and interlevel vias, and horizontal runners. The difficulty of forming such increasingly complex structures is worsened

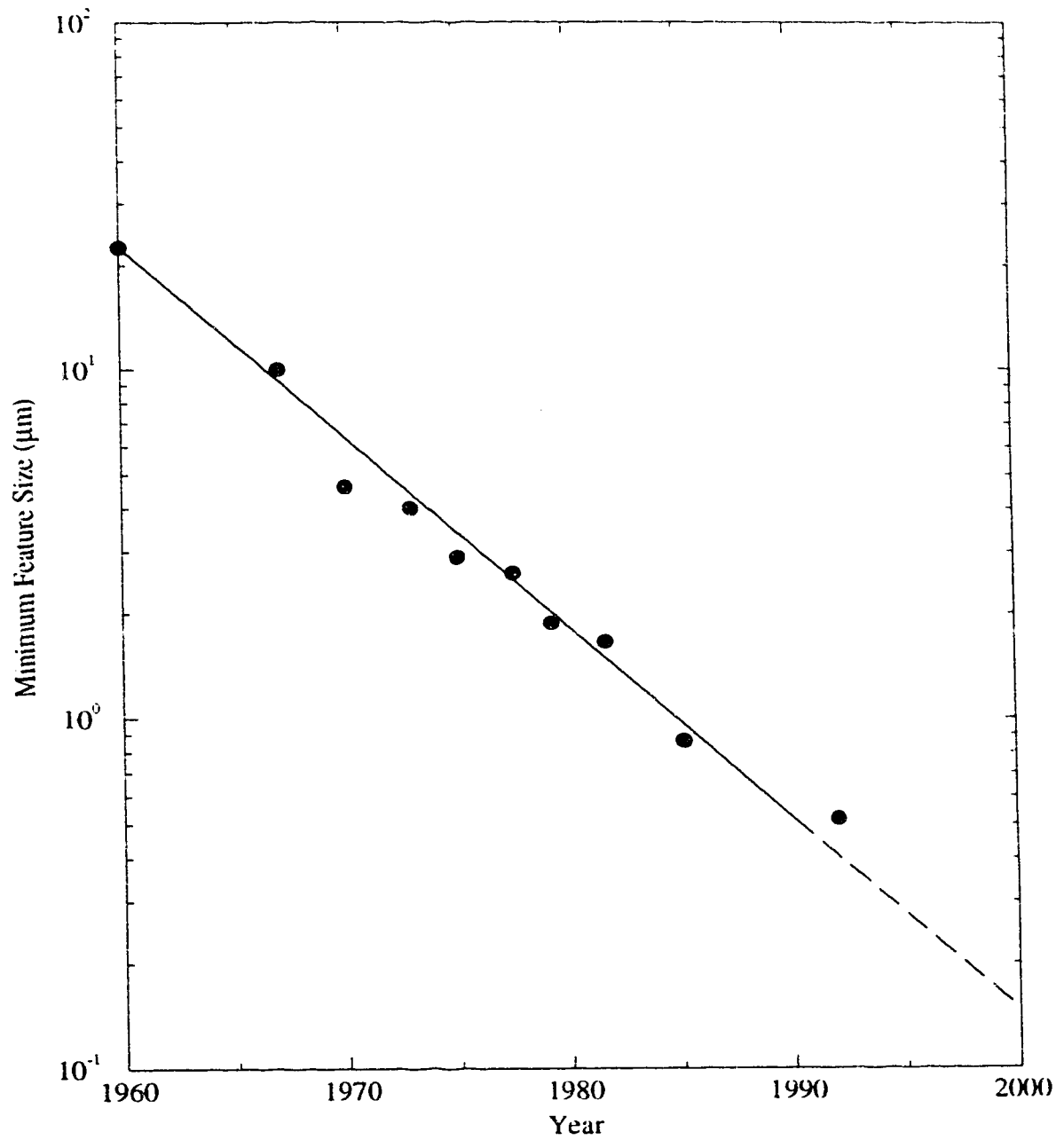


Figure 1.1: Plot of minimum feature size on representative integrated circuits over recent decades. [2,3] The dashed line shows the extrapolation of this trend to the year 2000.

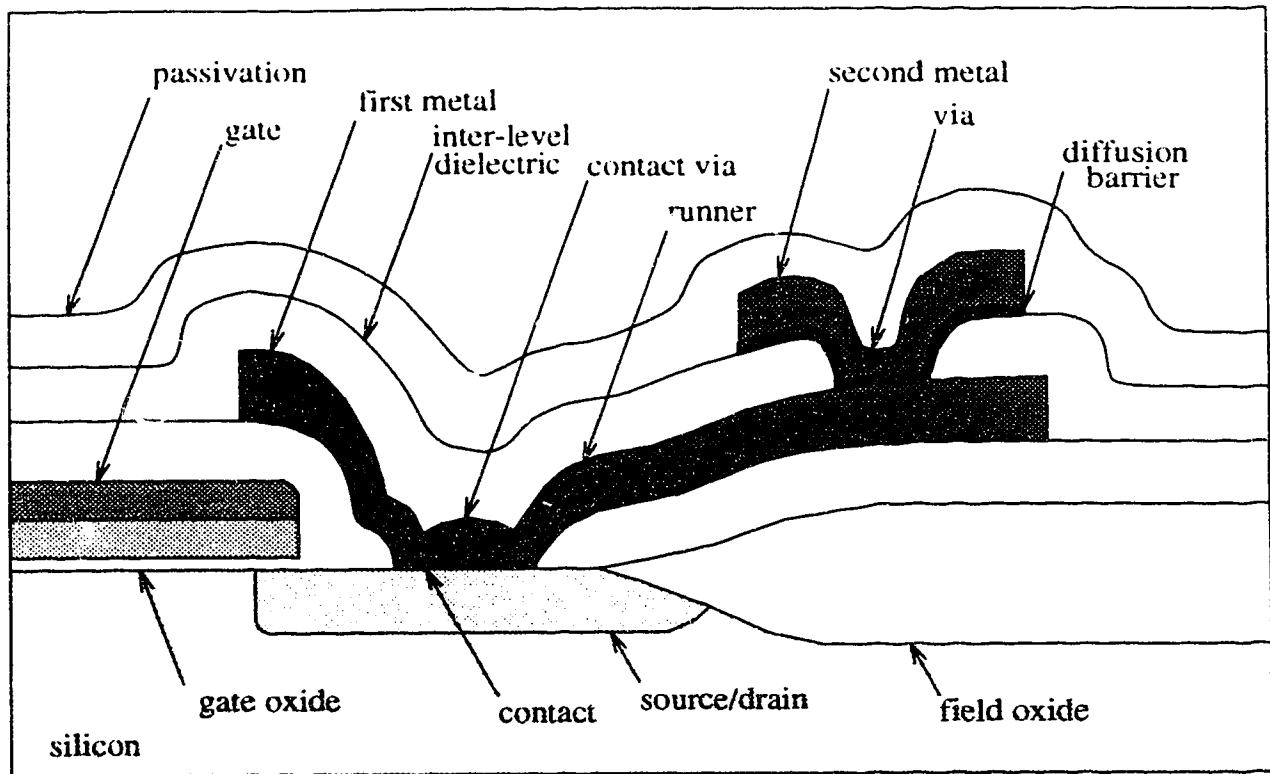


Figure 1.2: Cross-section of a hypothetical MOS structure with a two level metallization scheme. Various elements of metallization are identified. Typical integrated circuit stratification and topography is demonstrated. [12, 14] Currently, up to five levels of metallization are employed. [19]

by the severe topography.

The criteria of a good metallization material are effectiveness (low resistivity in vias and runners, low contact resistance in contact layers, low permeability in diffusion barriers), reliability (low electromigration and film stress), compatibility (no undesirable interactions with surrounding materials), manufacturability (ease of deposition, patterning, and etching over topography, good adhesion, high yield, stability during subsequent process steps) and low cost. [18]

There are currently no ideal material choices. At present, aluminum is the dominant material because it is effective, inexpensive, and manufacturable. However, even with the addition of small amounts of copper to reduce electromigration and of silicon to reduce interactions with the junctions, there are concerns about aluminum's reliability and compatibility. [15] Tungsten is a more reliable material with very low electromigration and reasonably well established manufacturability, but its higher resistivity make it less effective. [15] Copper is both effective and reliable, but it is less compatible with other materials and less manufacturable due to problems with deposition and etching. [20,21] This lack of an optimal material makes it likely that a combination of metals will be used in complementary roles. This hybrid approach, of course, further increases the complexity and cost of metallization.

1.2 Metallization Techniques

In the past, evaporation was the primary technique for depositing metallization layers. [22] It is a relatively simple and inexpensive process involving heating the source material (by ohmic or electron beam heating) in a vacuum system until it has a substantial vapour pressure. This vapour then condenses on the (much cooler) substrate to form the metal film. [16,17] However, despite the simplicity of this technique, problems with step coverage (see below for a discussion of step coverage) has limited its use in most advanced applications today. [22]

Currently, the dominant deposition process is dc magnetron sputtering. [23] (See Figure 1.3 for a schematic diagram of this process.) This is also a vacuum deposition technique, but, in contrast to evaporation, the flux of condensing metal is generated

by the recoil of high energy ions striking the metal target. [16] One important result of this difference is that sputtered flux is much more energetic than evaporated flux. This difference has an important impact on film properties. [16,23]

In dc magnetron sputtering, the ions are created in a glow discharge plasma which results from applying a large negative potential to the target in the presence of a low pressure working gas (usually argon which is intentionally added to the vacuum system). [16,22,24] This potential also serves to extract positive gas ions from the plasma and accelerate them into the target. Magnets are arranged behind the target to confine the plasma [22, 25] and thereby enhance the efficiency of the process. Typical sputtering pressures are 1–10 mTorr¹ for magnetron systems. [24] Because the sputtered flux is generally from a more distributed source (the target) than evaporation, the step coverage of sputtered films is generally much better. The ramifications of flux distribution and step coverage will be discussed to a greater extent in Chapter 3.

Another deposition technique which is becoming increasingly important to metallization is chemical vapour deposition (CVD). [23, 26] In this process, gaseous reactants are introduced into a chamber containing the substrate to be coated. Thermal or plasma activation initiates a surface reaction on the substrate whose solid product species is the material being deposited. Chemical vapour deposition has long been used in microelectronics fabrication for growing dielectric and polysilicon layers, but its application to metallization is recent. [26] The reaction precursor source is transported by diffusion processes and not limited by line-of-sight. The source is, therefore,

¹In this work, pressure is reported in units of Torr to conform to industry convention. The SI unit of pressure is the pascal. There are approximately 133 Pa in 1 Torr

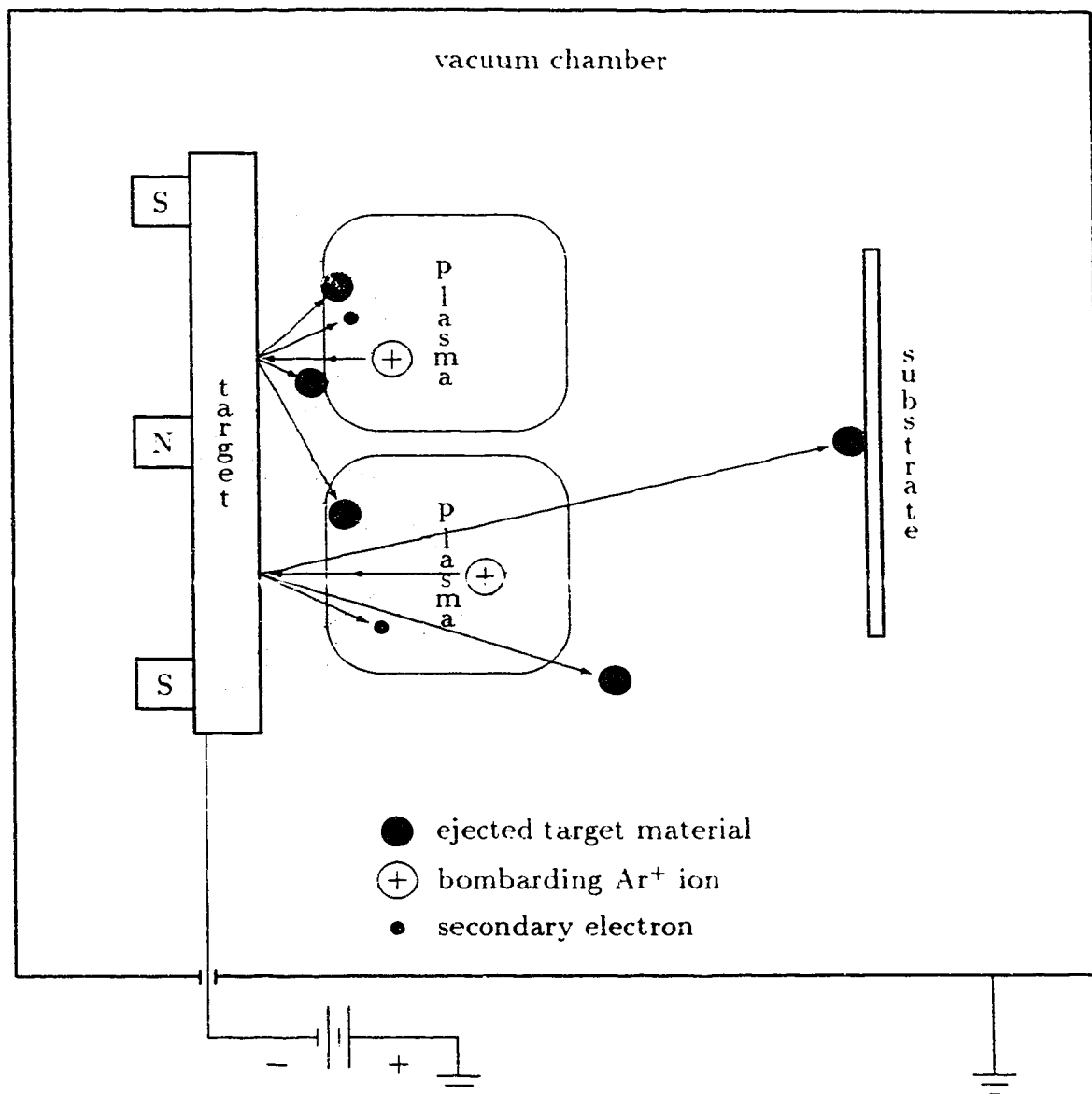


Figure 1.3: Schematic diagram of a dc magnetron sputtering system. The vacuum chamber is filled with low pressure argon gas. A potential is applied to the metal target which creates a glow discharge plasma. Ions from the plasma are accelerated into the target and cause target material (for example, Al or Al-Si-Cu alloy) to be ejected. Magnets confine the plasma near the target for greater efficiency.

usually well distributed and CVD step coverage can be much better than for evaporation or sputtering. [26] This deposition technique will be discussed in greater detail in Chapter 6.

1.3 Scaling Metallization to Smaller Dimensions

A number of fundamental difficulties arise for a metallization scheme, such as Figure 1.2, as dimensions scale below the current levels. The most important of these problems are high current density, poor step coverage, cross-talk, and the intrinsic film microstructure. [18,29,13] To a large extent, these problems are inter-related.

The increased current density results from the reduced cross section of the conducting paths as their dimensions decrease. This can lead to long term reliability problems due to a process called electromigration — particularly with aluminum alloys which are currently used. Electromigration is a thermally activated diffusion process whereby, at high current densities, the conducting material is literally carried away by the current. [27] This results in the conductor becoming depleted of material in some regions (leading to open circuit failures) and forming bridges in regions where material collects (leading to short circuits). Large aluminum grain size or the addition of small amounts of copper help reduce this problem, [27] but with continued scaling, electromigration will remain a serious problem.

The problems of electromigration are compounded by poor step coverage. Step coverage is a measure of the ability of a process to deposit films uniformly over topography. It is usually defined as the ratio of minimum sidewall coverage to the nominal film

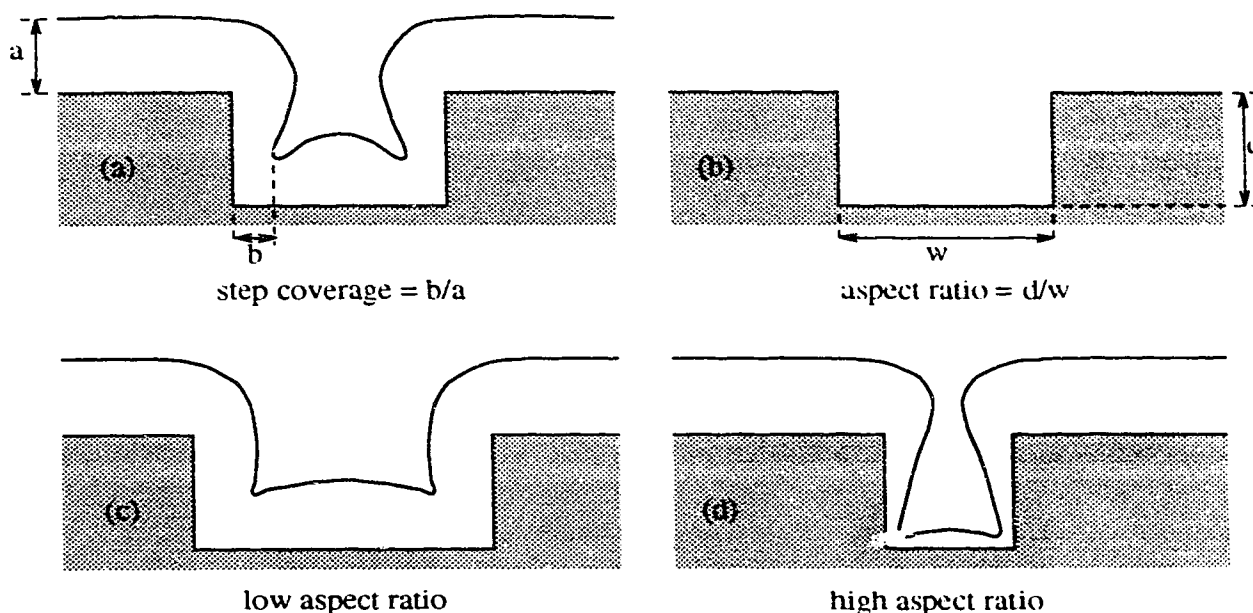


Figure 1.4: Definitions of the step coverage of a film deposited over topography (a) and of the aspect ratio of that topography (b). Step coverage generally degrades as aspect ratio increases from (c) to (d).

thickness on the top surface. (See Figure 1.4a.) For conventional metallization (sputtering), step coverage is degraded as devices scale to smaller sizes because dimensions are reduced primarily in the plane of the wafer since the thickness of the dielectric between metal layers cannot be scaled as quickly and still maintain adequate electrical isolation. [29] This means that the aspect ratio (Figure 1.4b.) increases, and it becomes more difficult to uniformly coat inside topographical features. (See Figure 1.4c and 1.4d) Figure 1.5 clearly illustrates this trend for films deposited over a $1\text{ }\mu\text{m}$ deep trench with varying widths. Relatively good coverage is obtained for $2\text{--}3\text{ }\mu\text{m}$ wide features, but step coverage falls off very rapidly in the high aspect ratio sub-micron range which is currently of interest. [11] (The factors which determine step coverage will be discussed in greater detail in Chapter 3.)

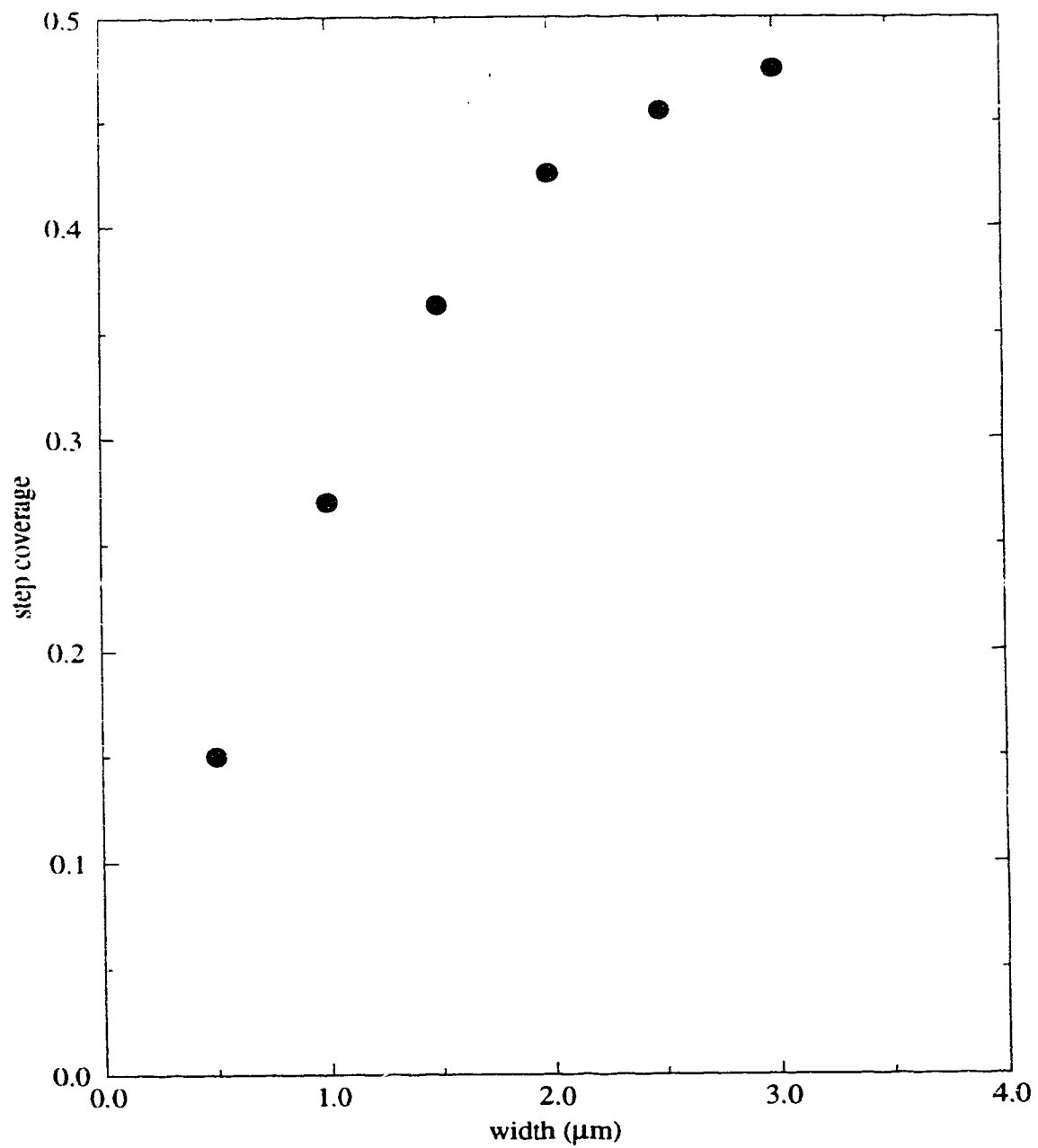


Figure 1.5: Variation in step coverage with feature width for a 1 μm deep trench with vertical sidewalls. [11] While absolute coverage depends on substrate geometry and a number of system parameters, the trend toward very poor step coverage above an aspect ratio of 1 is consistent for all conventional sputter systems.

Of course, any decrease in step coverage means that current densities down sidewalls are increased which compounds the electromigration problems there. In addition, the reduced metal coverage increases the resistance. This is undesirable since it increases capacitance delays (resulting in slower circuits) and it increases ohmic heating which, once again, increases thermally activated electromigration. Of course, in extreme cases, step coverage will reach zero and an open circuit failure will result.

Another scaling problem encountered in metallization is increased cross-talk and line delay which result as conducting lines become closer together under continued scaling. [29] To avoid this, multilevel metallization schemes are employed where extra levels of conducting lines (separated by layers of dielectric material) are stacked vertically to reduce line densities in any horizontal plane. In order to accomplish this, a thick dielectric layer is usually used to planarize (bring all topography to a constant level) before each additional metallization layer. [15] (See Figure 1.6) As a result of this planarization, very high aspect ratio vias are required to interconnect some of these layers. This, of course, increases problems with step coverage. [15]

1.4 Film Microstructure

One problem that metallization is increasingly encountering as dimensions scale further is the intrinsic microstructure of metallization layers. Microstructure refers to the internal structure and inhomogeneities of the film. Typically, deposited metal films are polycrystalline and composed of a matrix of roughly cylindrical columns which extend through the film. [14,28] The orientation of these columns is dependent on the incident angle of flux relative to the substrate normal. [30] Because the surface

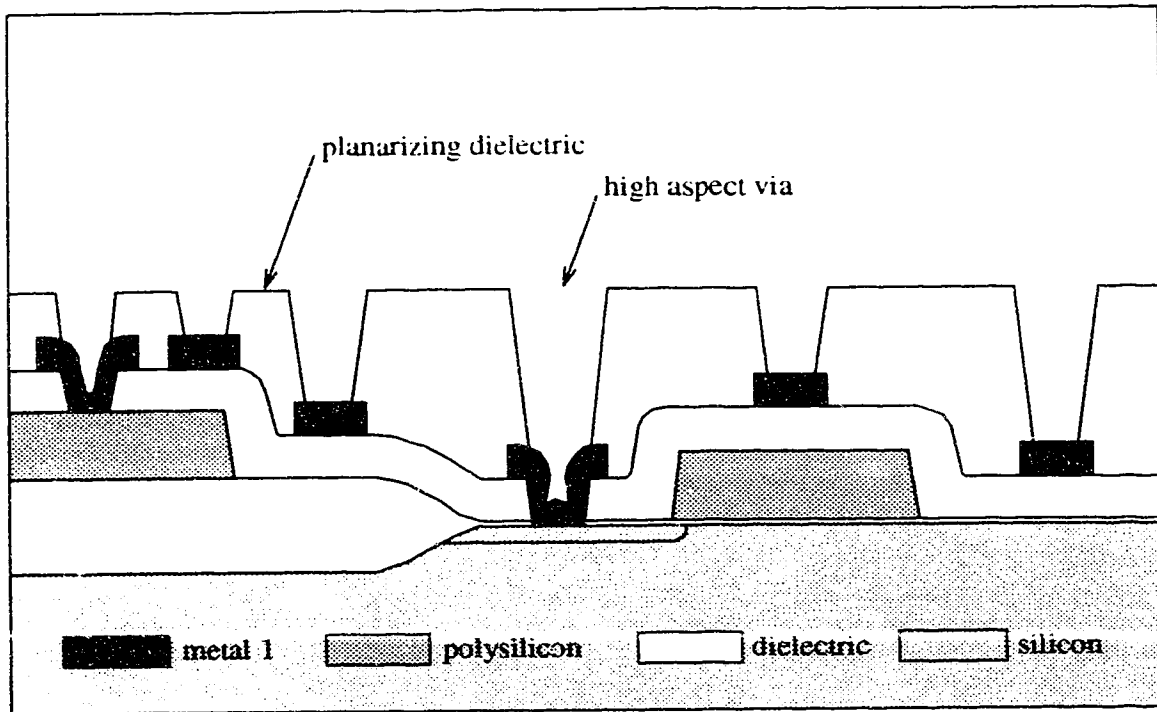


Figure 1.6: Planarized multilevel topography prior to deposition of the second metal layer. The thick planarizing dielectric layer creates very high aspect ratio vias.

normal varies substantially over integrated circuit topography, this columnar structure can become complex. Not surprisingly, it has an increasingly important impact on film properties as device dimensions approach those of the microstructure.

Figure 1.7 shows examples of two films which have been sputter deposited over topography and which demonstrate pronounced microstructural features. Figure 1.7a is a scanning electron micrograph (SEM) of a molybdenum film deposited over silicon dioxide steps on a silicon wafer. (The film has been lightly etched to highlight the structure.) The film columns can be seen radiating from the tops of the steps, and between steps, the columns are oriented perpendicularly to the substrate. Not surprisingly, such columnar structure can result in anisotropic film properties and

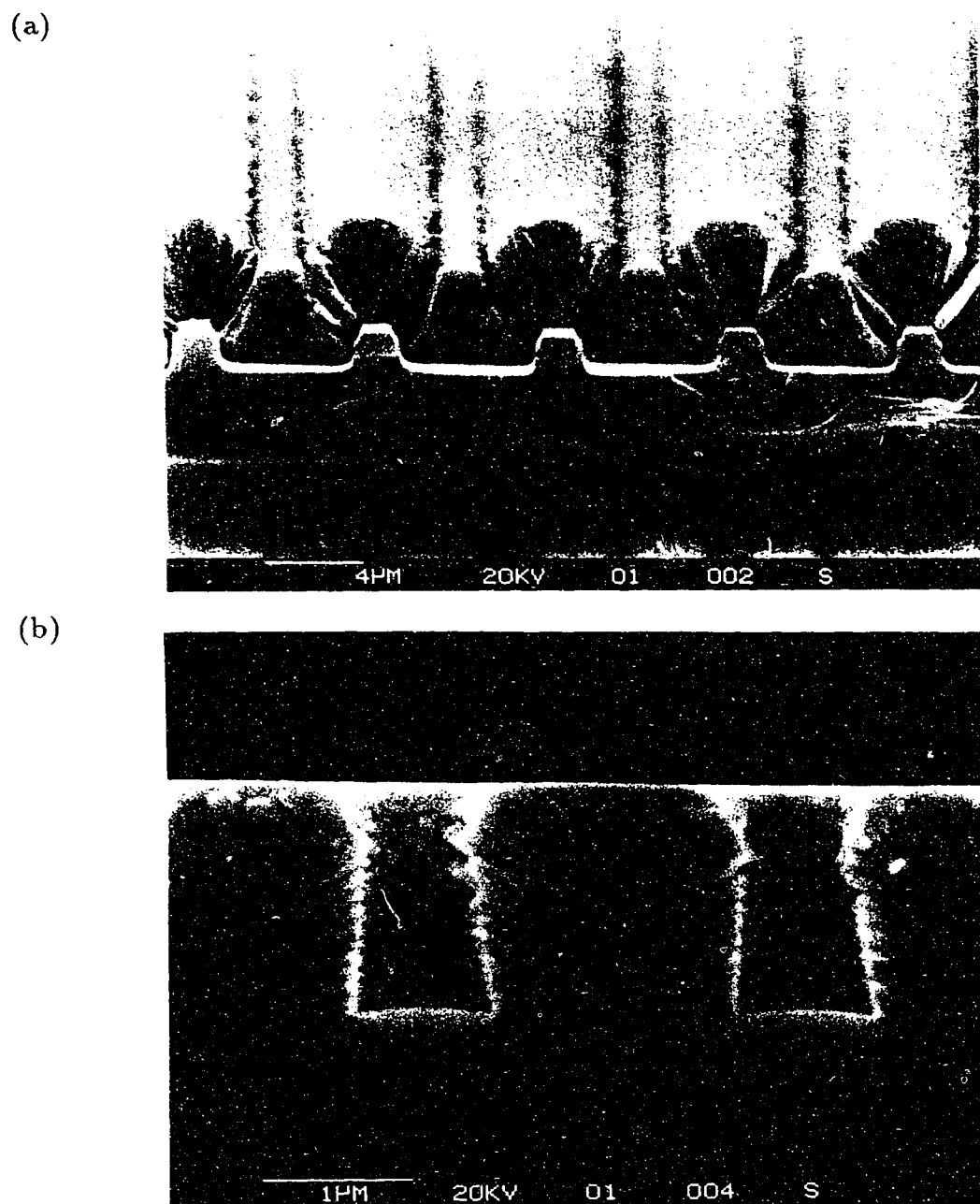


Figure 1.7: Cross-sectional electron micrographs of (a) a molybdenum film sputtered over silicon dioxide steps on a silicon wafer and (b) a titanium film deposited over a pair of vias etched into silicon dioxide on silicon. Microstructural features such as columns, voids, low density regions, and poor step coverage are visible.

g) films higher resistivity than that found in the corresponding bulk material. In addition to the columns, a very pronounced void can be seen extending out of the top corners of the step. Clearly, such a void makes the film discontinuous and would present a serious problem for current flow over the step.

Figure 1.7b shows a tungsten film deposited over a pair of contact vias (round holes which provide a connection path for the metal film through the silicon dioxide to the underlying silicon). As discussed earlier, the step coverage over them is quite poor (about 10% in this case) due to the high aspect ratio. In addition, it can be seen that the film on the sidewalls of the vias is porous and of lower density than the film on the top surface. One consequence of this lower density is a higher resistivity along the sidewall – in the very area where there are already concerns about high resistance due to poor step coverage. This makes these areas doubly at risk for electromigration failure.

In fact, the microstructure is also of interest to electromigration for a more general reason. Since electromigration is a diffusion process, it is more likely to occur along surfaces and grain or column boundaries where activation energies for diffusion are lower than for bulk material. [27, 78] Therefore, charting these boundaries and their orientation to current flow is important for predicting likely electromigration behaviour.

A microstructure feature that is of concern to subsequent integrated circuit fabrication steps is the surface roughness. It is difficult to uniformly expose photoresist over a metal surface that is rough due to problems with depth of field and notching. [22] It is also difficult to uniformly deposit subsequent layers upon such a surface. Since the

microstructure of one layer can propagate into the layer deposited on top of it, it is important to maintain as smooth a surface as possible.

Film microstructure also affects gate metallization, since it can affect the film's stopping power during implantation which is critical for forming self-aligned structures. [13] In addition, the columnar structure can trap impurities along column boundaries which then degrade gate performance. [15]

1.4.1 Origin of Microstructure

The columnar microstructure arises primarily from growth instabilities due to self-shadowing. [33] Any region of the film which has grown slightly higher than its neighbours will intercept a greater proportion of the incident film flux and hence grow more quickly — eventually shadowing the neighbouring regions entirely and creating a film column. These instabilities are at least partly offset by the effects of surface diffusion (and grain boundary and bulk diffusion at higher temperatures) which tends to redistribute material from the fast growing regions to the slower ones. [33]

Typically, films initially nucleate as a collection of small islands. [28, 31, 32] Often these film islands form around substrate defects, but even a perfect crystal can have island nucleation — depending on the respective interfacial energies of the substrate and film. [33] These nuclei gradually grow together and eventually the film becomes continuous, but this process creates the perturbations which initiate columnar growth.

Self-shadowing is determined by geometrical considerations. Diffusion, however, is determined by material properties and temperature. [78] Consequently, the relative importance of these competing mechanisms is shifted by changing the temperature.

For evaporated films, this relation was recognized by Movchan and Demchisin in their Structure Zone Model. [34] The model (see Figure 1.8a) identified three distinct classes of structures which were determined by the substrate temperature during growth relative to the melting temperature of the film material. At low temperatures, surface diffusion is minor and shadowing dominates. The resulting zone 1 structure is porous, with separated microcrystalline columns and low overall density. At higher temperatures (up to about one-half the melting temperature), surface diffusion causes the broader, more densely packed columns of zone 2. At even higher relative temperatures, grain-boundary diffusion, bulk diffusion and grain growth become more important to the structure. In this zone 3 structure, the columns are replaced by large polycrystals. [28]

Thornton extended this work to sputtered films by incorporating the effects of pressure during deposition. [36–38] (See Figure 1.8b) The higher pressures involved moderate the energy of the (initially much more energetic) sputtered atoms through collisions with the gas molecules while travelling between the target and substrate. Since high adatom energy raises the effective film surface temperature, both the pressure and temperature are considered in Thornton's model to determine the characteristic film structure. Another factor that must be considered for sputtered films is the effect of other energetic particles which are also generated by the sputtering process and which can bombard the film. It is believed that these particles are responsible for the formation of the zone T structure of dense, fibrous columns intermediate to zones 1 and 2. [38]

These structure zone models are useful for providing a qualitative understanding of the origin of thin film microstructure. This is valuable information since, as discussed

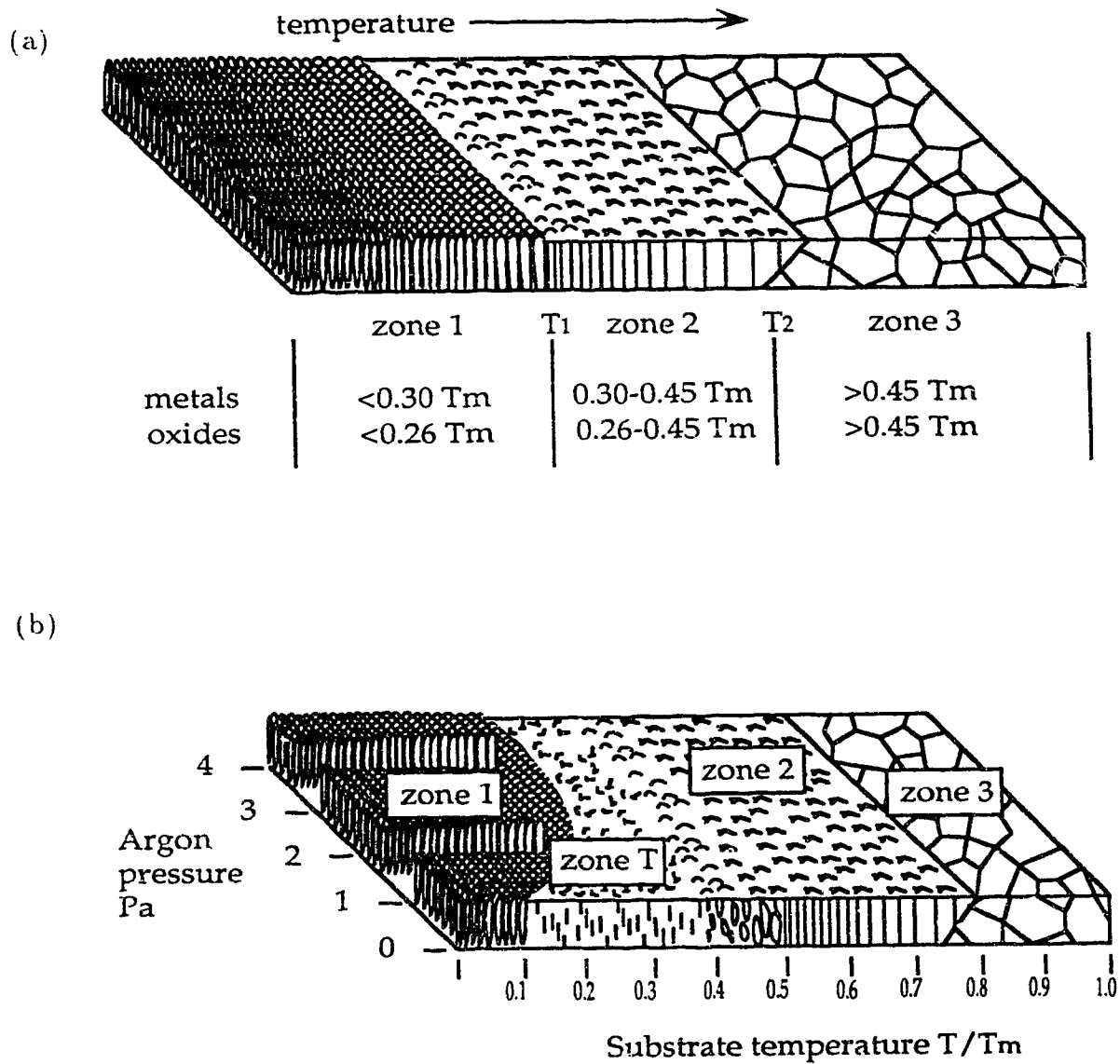


Figure 1.8: Movchan and Demchisin proposed a three zone structure model (a) for evaporated films based on the ratio of absolute substrate temperature to film melting temperature (T_m). Thornton extended this model (b) to sputtering by accounting for the effects of sputtering gas pressure. (Figure used with permission of R.N. Tait. [35])

above, the microstructure of metallization layers can have an important impact on their performance in advanced metallization applications.

1.5 Advanced Metallization Techniques

In order to alleviate some of the problems discussed above (particularly those due to poor step coverage), several advanced techniques for metallization have been proposed. These include [23,22]

1. use of optimized sputter distributions
2. bias sputtering
3. high temperature aluminum deposition
4. metal chemical vapour deposition

All of these approaches have a marked effect on both the step coverage and microstructure of the metallization layers. The relative costs and complexities of these four approaches increase in the order presented. However, as will be demonstrated in the following chapters, the effectiveness of these approaches (particularly with respect to step coverage) also increases in the same order. Therefore, a trade-off must be made between cost and effectiveness.

This thesis investigates each of these four advanced metallization processes in Chapters 3 through 6, respectively. One goal of this work is to determine the key parameters to each process and their effect on the step coverage and microstructure of the resulting film. Since a thorough experimental analysis of all of these techniques would be

prohibitively expensive in terms of cost and time, the primary vehicle for performing this analysis is through simulation studies. Since no completely suitable simulation tools are currently available, the second, and perhaps more important, goal of this work is to develop such tools as are required to investigate and help optimize each of these proposed advanced metallization processes.

The organization of the remainder of this work is as follows: Chapter 2 reviews the existing simulation tools and their suitability for simulating advanced metallization techniques. Emphasis of this chapter is on the SIMBAD model and how it might be extended to achieve the desired goal. Chapters 3 through 6 each discuss the model development and then the experimental and simulation results for one of the proposed metallization processes listed above. Finally, Chapter 7 summarizes these results and presents the conclusions of this thesis as well as recommendations for further work. The Appendices discuss aspects of the simulation algorithm and program organization.

Chapter 2

Simulation of Thin Film Deposition

The goal of simulating metallization processes is to provide realistic and useful depictions of the resulting films at lower cost and/or faster than is possible through experimental means. Another benefit of simulation is it can often assist fundamental understanding of the process at a level not possible through experiments. However, due to the abstractions and approximations that must be made to develop a workable model, it is not possible to guarantee that simulation results will accurately reflect reality. For this reason, simulation can supplement and complement experimentation, but cannot completely replace it. Wherever feasible, experimental verification and calibration are required.

The requirements of the metallization simulation needed for advanced metallization processes are

- capability to simulate a variety of deposition techniques
- ability to represent arbitrary sub-micron substrate topography
- ability to depict step coverage and film microstructure
- high speed and low cost of execution

The best computing platform for such a simulation is probably an engineering workstation since it represents an acceptable compromise between cost and performance and is likely to be readily available to the metallization engineer or process developer who would be most interested in process simulation. Supercomputers are undoubtedly capable of more detailed depictions, but their rarity and high cost can make them less attractive than experimentation. On the other hand, personal computers are cheap and prevalent, but their more limited performance may not be adequate for detailed simulation requirements.

One common approximation made by many thin film process models is to reduce the problem from three to two dimensions. This can make an enormous difference to computational requirements since only $N^{2/3}$ elements need be considered, rather than N . This reduces both the computational and the memory requirements of the simulation. In addition, many of the geometric calculations are much simpler in two dimensions which further decreases execution times. However, there are legitimate concerns about the validity of this dimensional reduction in some situations. [39-41] Strictly speaking, this approximation is only valid under circumstances when there is a symmetry which reduces the dimension of the problem. This would be the case for deposition over long features of constant cross-section (such as trenches or steps) or features which are cylindrically symmetric (such as round vias). Fortunately, this subset of features is still very useful for testing the effectiveness of deposition techniques over advanced integrated circuit topographies.

2.1 Types of Models

There have been several approaches to simulating thin film growth which have varying levels of detail. At one extreme are the atomic-level models such as molecular dynamics and atomistic Monte Carlo models, which account for the positions and interactions of every individual atom. At the other end of the spectrum are the continuum and string algorithm models which only account for the position and development of the gross film surface. Somewhere in between are ballistic deposition models, which use abstractions of the film material which are larger than atomic size, but provide greater detail than string algorithms. This section will explore the suitability of each of these types of models to meet the simulation requirements stated above.

2.1.1 Molecular Dynamics

Two or three dimensional molecular dynamics models compute the forces between all combinations of interacting atoms and solve the resulting equations of motion. [42] This very detailed approach is quite useful for modeling inter-atomic processes such as recrystallization, epitaxy, and stress generation. [43–46] Unfortunately, most practical applications to ULSI fabrication, even in two dimensions, involve on the order of 10^8 atoms.¹ Since the positions and velocities of each of these must be calculated for each time step and stored in memory, application of molecular dynamics simulations

¹ Assuming a simulation region of $2\mu\text{m}$ by $2\mu\text{m}$ and an atomic density of aluminum, [47] this gives $(0.0002\text{ cm})^2 \times ((2.702\text{ g/cm}^3) \times (6.022 \times 10^{23}\text{ atoms/mole}) / (26.98\text{ g/mole}))^{2/3} = 6.2 \times 10^7\text{ atoms}$

on this scale leads to enormous computational requirements. Furthermore, the appropriate time scale for the dynamics of inter-atomic interactions is sub-nanosecond, while typical film depositions occur over at least several minutes. [42,43] This means some 10^{11} time steps are needed to model a deposition realistically. These enormous computational requirements seriously limit the widespread application of molecular dynamics simulations as process development tools.

2.1.2 Atomistic Models

Atomistic Monte Carlo simulations are similar in scale to molecular dynamics models, but avoid the time scale problems by requiring only one time step per atom added to the film. This is accomplished by assuming a greater degree of independence between atoms and making some assumptions about equilibrium conditions. [42,46,48] However, there is still the limitation that even representing very small ULSI structures requires a very large number of atoms. Therefore, even though they can provide detailed microstructure information, the necessary computing requirements of atomistic Monte Carlo and molecular dynamics models effectively limit their application in integrated circuit process simulation.

2.1.3 String Algorithms

String advancement models, such as the popular SAMPLE [49] from the University of California at Berkeley or SPEEDIE [50] from Stanford University, represent only the surface of the film at relatively coarse resolution and in only two dimensions. Consequently, these models are very practical to implement on current computers.

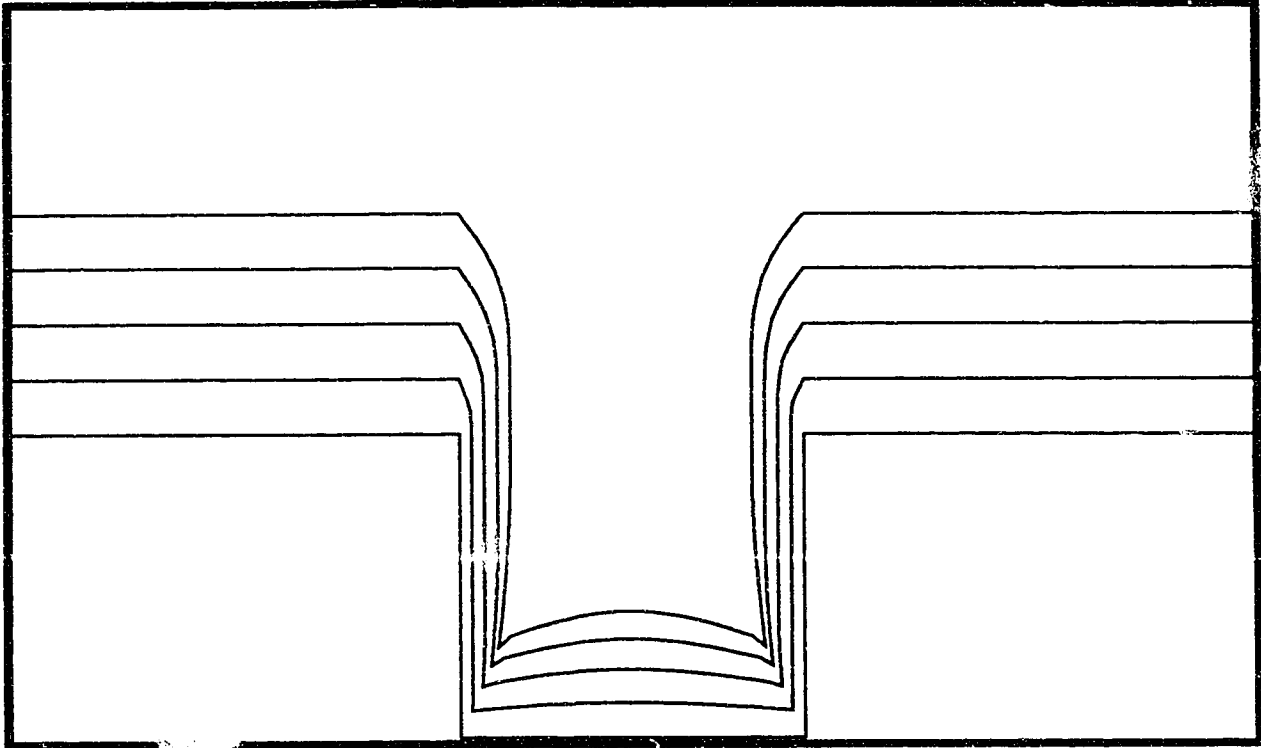


Figure 2.9: SAMPLE depiction of a film deposited over a via. Surface profiles from various stages of growth are shown.

The film surface is modeled in cross-section as a continuous line composed of line segments, called strings — each of which is advanced as the film grows in accordance with the calculated flux reaching it. [41] These simulations can execute very quickly and can be quite useful for predicting film coverage over various topographical features. (See Figure 2.9) This simplicity and speed have resulted in string algorithms being extensively used in commercial products such as *DEPICTTM* [51] or *SSAMPLE*. [52] Recently, this concept has been extended to a full three dimensional model to increase its applicability. [41] However, by their nature, string algorithm models treat the film as homogeneous and, hence, they can provide no information about the internal microstructure. Since knowledge of this microstructure is important for

predicting the performance of ULSI metal films, string algorithms are not well suited for the proposed advanced metallization simulations, either.

2.1.4 Continuum Models

Like string algorithms, continuum models represent only the film surface but at a higher level of resolution. This surface evolves according to nonlinear analytic models which try to account for surface diffusion and shadowing. [53–57] These models do qualitatively reproduce the growth instabilities which lead to the columnar microstructure, and can be very fast and efficient to execute in two dimensions. However, significant approximations are usually required to make solutions of the mathematics tractable. [54–56] Also, the deterministic analytic models may not be well suited for capturing the essential features of nucleation which is principally a stochastic process. [30] Thus far, these models have not been applied to simulating deposition over integrated circuit topography.

2.1.5 Ballistic Deposition

Originally applied to thin film deposition by Henderson, [58] ballistic deposition models are similar to the atomistic Monte Carlo models except that in order to make the execution time and memory requirements reasonable, they deal with abstract particles which correspond to chunks of film material much larger than individual atoms. These particles represent a statistical average of many atoms each with similar trajectories and energies. The size of these particles is chosen so that they are much smaller than the microstructural features they are supposed to illustrate, but large enough

such that sufficiently few are needed to keep the simulation times practical. [43,58,59]

Since these particles are abstractions of the actual deposition process, the rules governing their interactions and incorporation into the growing film are not as intuitive as for atomistic models. (For instance, to model diffusion, one must consider factors such as film curvature and not simple random lattice site hopping.) Possibly as a consequence of this, there have been few applications of ballistic deposition to technologically important processes such as integrated circuit fabrication. [60,66] Nonetheless, such models are capable of both the microstructure-level representation and practical application to advanced metallization processes. The SIMBAD model [66] has probably the greatest suitability in this regard.

2.2 SIMBAD

The basic SIMBAD (SIMulation by BALListic Deposition) model was developed by Professor M. Brett at the University of Alberta, [61–63] and has been extended to simulate a variety of thin film properties and processes. [64–77] The primary purpose of the program is to provide step coverage and microstructure depictions of films deposited over integrated circuit topography. SIMBAD is a two-dimensional simulator which is capable of providing cross-sectional depictions in reasonable times (as little as a few minutes) on a typical engineering workstation (Sun SPARCstation 2).

In the SIMBAD algorithm, the film is represented by the aggregation of 10^4 to 10^5 identical hard discs. These discs represent statistically averaged physical particles such as atoms, molecules, or ions, which have similar trajectories and impact points.

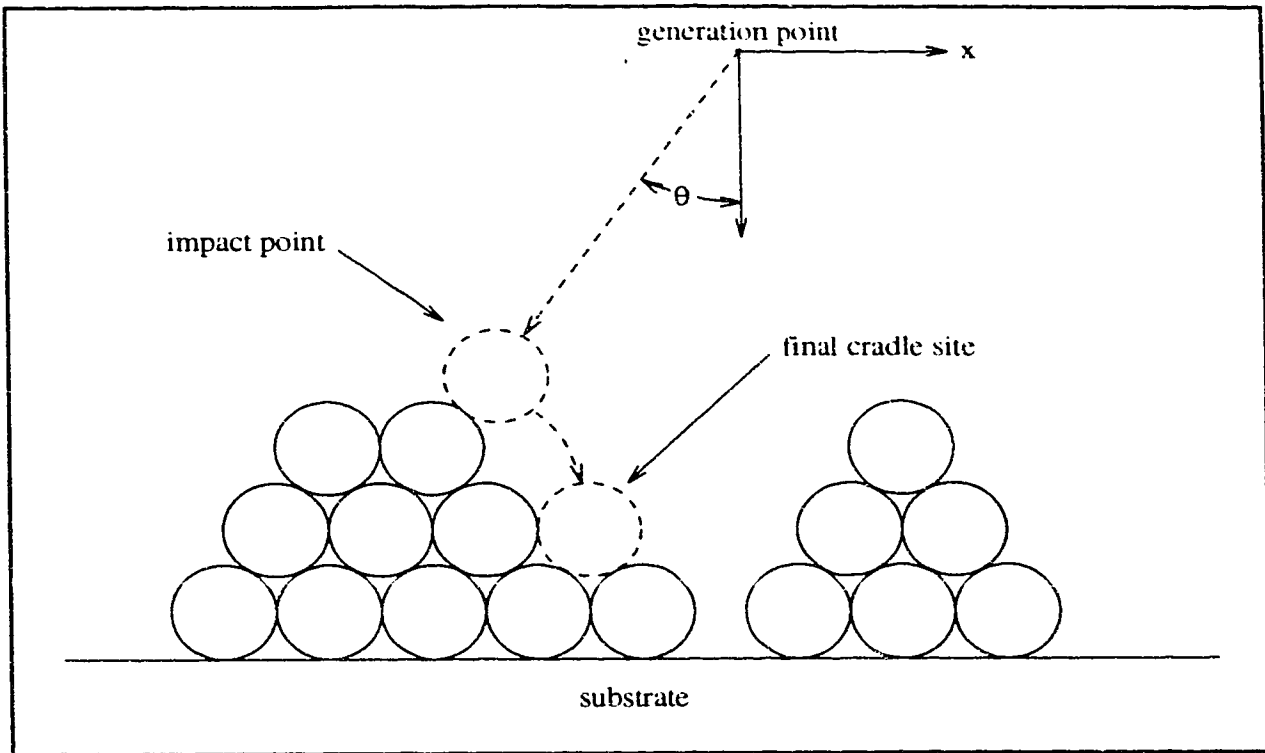


Figure 2.10: Schematic description of the SIMBAD algorithm. Discs are launched from a random position just above the substrate with a trajectory given by an angle randomly generated from the appropriate angular distribution. They diffuse from their impact points to sites which maximize coordination with other discs within a maximum searching range.

Shadowing and surface diffusion, which primarily determine film columnar microstructure, are incorporated into SIMBAD in a two-stage algorithm. (See Figure 2.10). Periodic boundary conditions are employed in this algorithm to prevent unwanted edge effects.

In the first stage of SIMBAD, the discs are serially and independently launched from random locations just above the substrate. (The exact distance above is unimportant provided that it is much less than the mean free path for collisions between the

depositing flux and the ambient gas. This restriction is lifted in the case of high pressure deposition as discussed in Chapter 6.) These discs have a trajectory determined randomly from an angular distribution which is dependent on the deposition process. Each disc follows a straight line trajectory until it strikes the substrate or a previously-deposited film disc. This ballistic stage of the algorithm intrinsically incorporates the effects of shadowing, both by the substrate topography and by the neighbouring film regions.

Surface diffusion is accounted for in the second stage of the algorithm. Once the impact point has been determined, the film surface is scanned in both directions up to a maximum diffusion length for the closest position which cradles against the largest number of previously-deposited discs (without overlapping any of them). This simple algorithm is efficient to implement and tends to reduce both local concentration gradients and local film curvature which are qualitatively the desired effects of short range surface diffusion. [78, 79] This diffusion algorithm is somewhat size-dependent, however, and if extended beyond a maximum range of about 6 disc diameters, it leads to unphysical surface facetting along the hexagonal, closest packed, planes. (See Figure 2.11) For reasonable resolution at ULSI dimensions, this limits the application of the basic SIMBAD algorithm to low and moderate deposition temperatures corresponding to zone I and II growth.

Grain growth effects are not currently modeled by SIMBAD. At the temperatures appropriate for SIMBAD depiction, film columns are generally polycrystalline. Assuming random grain orientation, any anisotropic effects of crystal orientation will be averaged out and, hence, will not affect column growth. (At higher temperatures, however, each column can become a single crystal and the grain and column structure

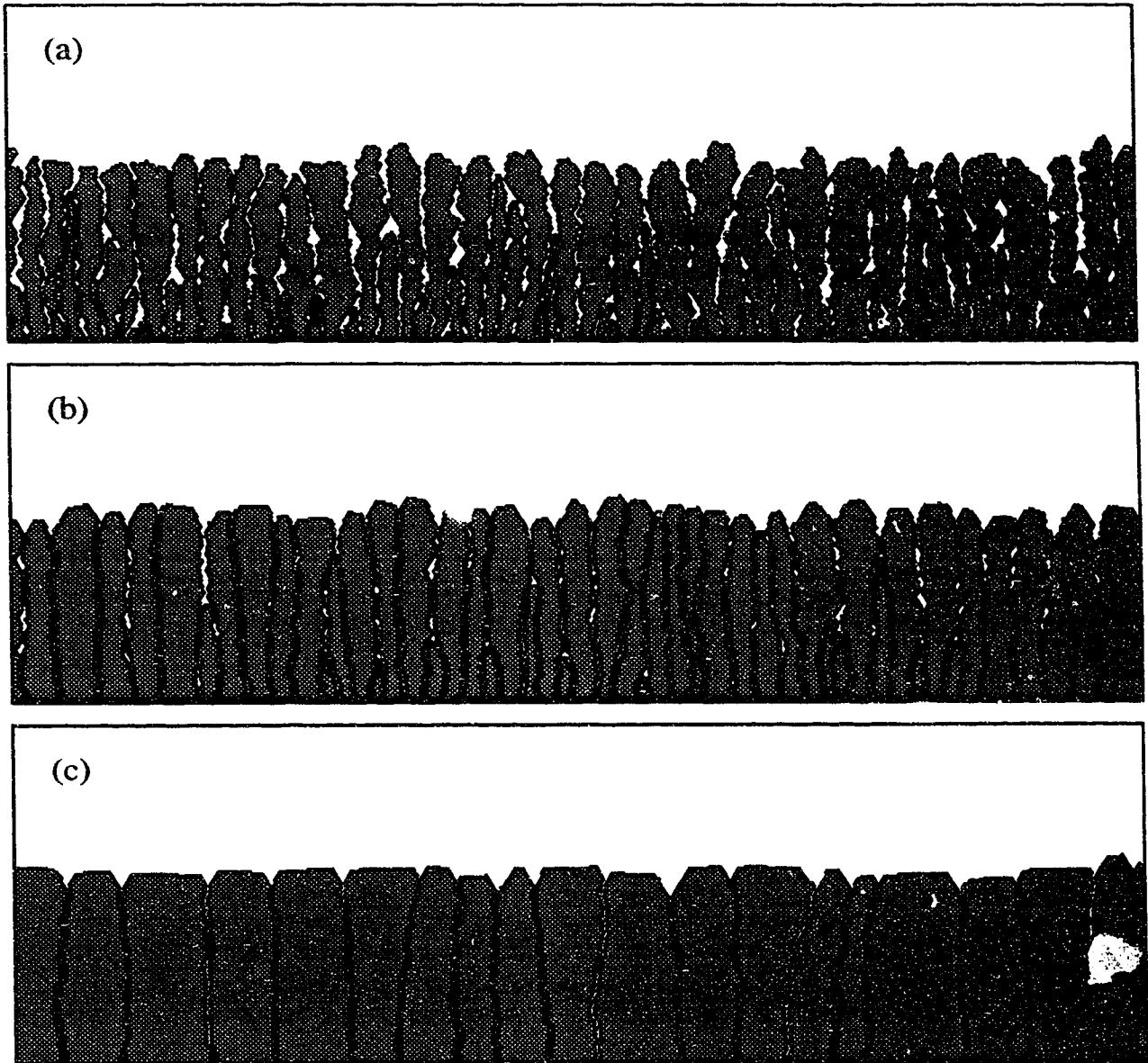


Figure 2.11: Anomalous faceting of column tops occurs for long diffusion lengths with the basic SIMBAD algorithm. Diffusion ranges of 2 disc diameters (a), 4 diameters (b), and 12 diameters (c) are shown. (For a typical ULSI topography simulation, a disc diameter would be 5–10 nm.) By (c), only 0° and $\pm 60^\circ$ surfaces tend to develop. This limits the current SIMBAD algorithm to relatively short diffusion ranges corresponding to low and moderate temperatures.

are equivalent.)

The inputs to SIMBAD are simply the initial topography profile, the angular distribution of the incident particles, the surface diffusion length, and the film thickness. (Additional parameters will be introduced in successive chapters.) The output of SIMBAD is a final film profile composed of the deposited discs. (See Figure 2.12a) In addition, since SIMBAD is a stochastic model, successive runs with different random seeds will generate slightly different representations of the film. Several of these can be averaged together to produce a density profile (See Figure 2.12b). This capability to generate density maps is a feature unique to SIMBAD. [65]

This conceptually simple model successfully captures most of the essential features of thin film step coverage and microstructure formation. (For example, compare Figure 2.12 with Figure 1.7) However, in order to extend this model to account for advanced metallization processes, several features must be added to SIMBAD. These include prediction of the appropriate angular distributions for different sputtering conditions, incorporation of the effects of ion bombardment during bias sputtering, extension of the diffusion model to longer lengths corresponding to higher temperatures, and incorporation of the effects of non-unity sticking in chemical vapour deposition. Each of these areas will be discussed in succeeding chapters.

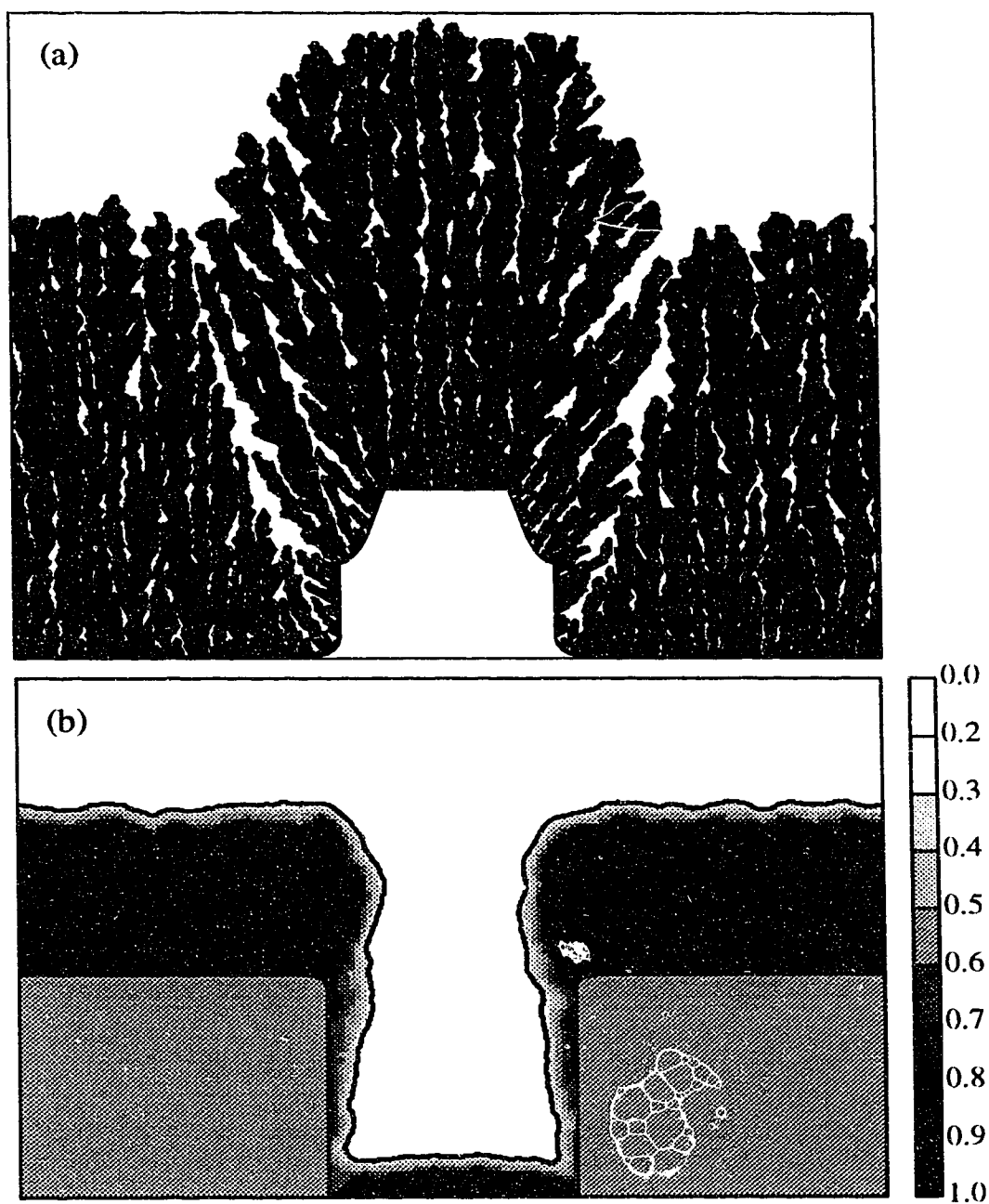


Figure 2.12: SIMBAD output formats. Film cross-section (a) showing columns and other microstructural features, and density map (b) showing density variations over topography. These results can be compared to the experimental photographs of Figure 1.7

Chapter 3

Sputter Distributions¹

3.1 Introduction

The properties of a sputter-deposited film are strongly dependent on characteristics of the flux arriving at the substrate. Film growth simulations, such as SIMBAD, can predict and help optimize such properties only if these characteristics of the incident flux are known. Since this information is tedious or difficult to measure experimentally, it is desirable to develop a model to predict these characteristics. SIMSPUD (SIMulation of SPUtter Distributions) is such a model, which provides information about the spatial flux density distribution and the angular and energy distributions of particles arriving at the substrate. This information can be used to determine relative deposition rates, thickness uniformity across a wafer, and, in conjunction with SIMBAD, step coverage and microstructure of the metallization layer under various deposition conditions. This information is important to determining throughput, yield, performance, and reliability of the metallization film.

SIMSPUD is a three-dimensional Monte Carlo vapour transport model. Similar models have been developed previously, but they have either been limited to provide

¹The material in this chapter has been accepted for presentation at the National Symposium of the American Vacuum Society, in November, 1992, and will be reviewed for subsequent publication in the Journal of Vacuum Science and Technology, A.

information only about the energy distribution [80-83] or spatial flux density; [84] have applied only to specific or unusual geometries; [85,86] have omitted the energy dependence in collision cross-section; [81,82,84,86,87] or have required a supercomputer for execution. [88] In addition to being efficient, versatile, and providing more information about sputter distribution characteristics, SIMSPUD has an important advantage of being readily integrated with a general film deposition model, such as SIMBAD.

3.2 Sputter Distributions and Film Properties

By modelling the transport of particles from generation at the target to deposition at the substrate, SIMSPUD can directly predict uniformity profiles and relative deposition rates. However, the angular and energy information produced by SIMSPUD must be passed to SIMBAD in order to provide step coverage and microstructure depictions. This information is used by SIMBAD to predict film properties in the following manner.

Step coverage is determined in SIMBAD by the interaction between the incident angular distribution and the substrate topography. For example, if the angular distribution is asymmetric, the coverage inside of topography will also be asymmetric. (See Figure 3.13a.) If the distribution is tightly focussed about the substrate normal, then the coverage along the bottom will be good, but sidewall coverage will be poor. (See Figure 3.13b.) If the distribution is too broad, much of the flux will exceed the maximum acceptance angle into the feature, and both poor sidewall and bottom coverage will result. (See Figure 3.13c.) Obviously, an intermediate situation would

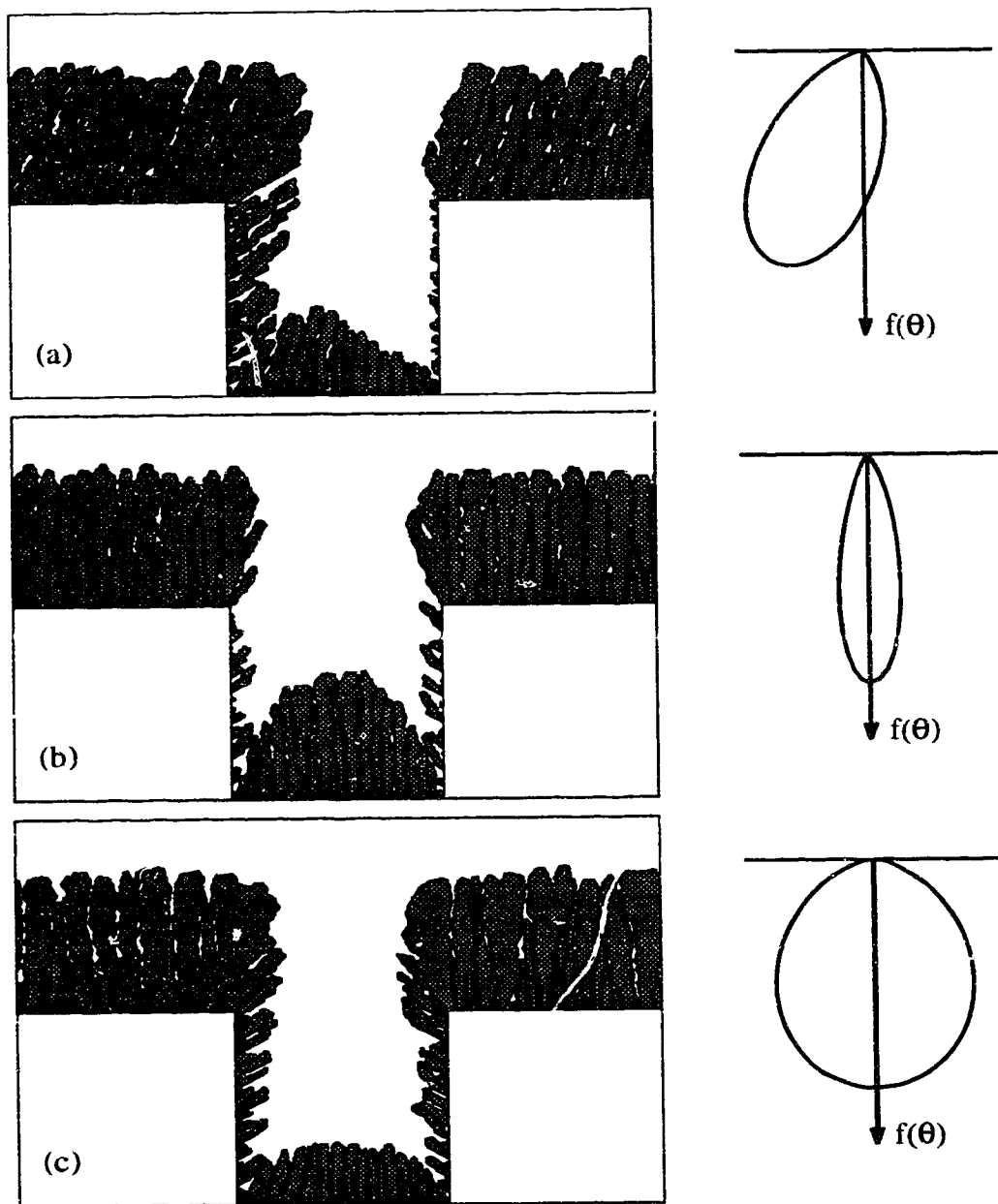


Figure 3.13: The effect of angular distribution on coverage and microstructure. An asymmetric distribution (a) causes uneven coverage and angled columns. A focused distribution (b) leads to narrow columns with good bottom coverage but poor sidewall coverage. A very broad distribution (c) creates broader columns and poor coverage throughout the feature.

be preferred.

The columnar microstructure is also affected by angular distribution since shadowing is an important component of microstructure development. Figure 3.13a also shows the tendency of columns to orient toward the direction of incident flux. For mono-angular flux (such as often found in evaporation) this is empirically given by the tangent rule [89]

$$\tan \zeta = \frac{1}{2} \tan \theta \quad (3.1)$$

where ζ is the column angle from the local surface normal and θ is the incident flux angle. For diffuse sources, the column angle would depend on weighting this relation by the angular distribution, $\int_{\theta}(\theta)d\theta$.

Figure 3.13b and c also show that focused angular distributions lead to narrower columns with greater intercolumn gaps on angled surfaces than do broader distributions. The column shape is also affected by the energy distribution, since higher mean incident energy will increase the effective temperature of the growing film and, hence, increase surface diffusion and column width (as can be seen in Figure 2.11).

3.3 The SIMSPUD Model

As mentioned above, SIMSPUD is a three-dimensional Monte Carlo simulation which provides distribution information about the sputtered atoms arriving at the substrate. In order to accomplish this, SIMSPUD must incorporate the effects of two events. First, the generation of sputtered atoms at the target with appropriate spatial, angular and energy distributions must be considered. Then, SIMSPUD must account for

the evolution of those distributions as the particles move from the target to the substrate. This second phase is complicated by scattering events between the sputtered particles and the argon gas. The amount of scattering can vary considerably because sputtering generally occurs in the threshold pressure regime between molecular (where gas collisions rarely occur) and Knudsen (where collisions are important) behaviour. [90] Hence, a small change in gas pressure can substantially change the importance of gas scattering. At low sputtering pressures, the flux experiences very few collisions and arrives at the substrate with high energy and unmodified angular distributions. Higher pressures cause significant energy loss to the sputtering gas and broadened angular distributions.

The sequence of the SIMSPUD model is shown schematically in Figure 3.14. Sputtered particles (usually atoms) are generated at the target surface, typically in a spatially nonuniform manner. Magnetron sources, especially, have a high sputtered atom flux density variation due to the localized plasma confinement. To account for this variation, SIMSPUD uses a sputter density function which is inferred directly from the depth of the erosion pattern on a used target. Obviously, different erosion patterns must be input for different magnetron source configurations and target materials. For simplicity, a planar target with cylindrical symmetry is assumed. (This corresponds to the most common sputtering source geometry.) The simulation input is then a radial erosion depth profile, $S(\rho)$. Simulated atoms are generated randomly on the target at a position, P , given in cylindrical coordinates by $P(\rho_o, \phi_o, z_o)$ where $z = z_o$ corresponds to the target separation from the substrate at $z = 0$, and (ρ_o, ϕ_o) are determined from the random distribution

$$f_P(\rho, \phi) d\rho d\phi = C_P \rho S(\rho) d\rho d\phi \quad (3.2)$$

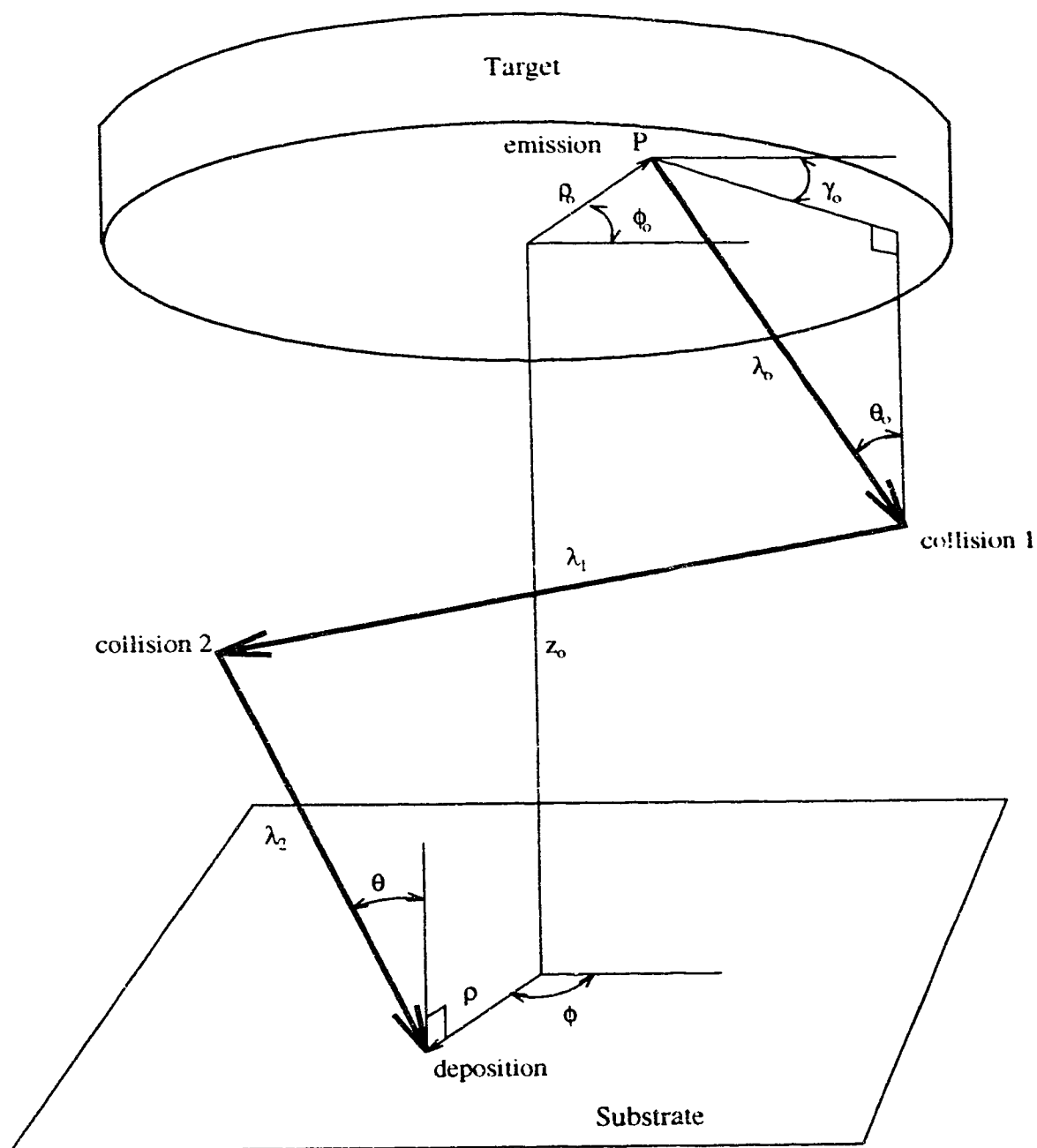


Figure 3.14: Schematic description of the SIMSPUD algorithm. Sputtered atoms are emitted from the target at coordinates (ρ_o, ϕ_o, z_o) with a trajectory (θ_o, γ_o) and energy E_o . They follow straight line trajectories, possibly suffering collisions with the process gas en route to the substrate.

where C_P is a normalization constant.

The angle of atom emission, (θ_o, γ_o) , is randomly chosen from the distribution [84]

$$f_{\Omega}(\theta, \gamma) d\theta d\gamma = C_{\Omega} g(\theta) \sin \theta d\theta d\gamma \quad (3.3)$$

where C_{Ω} is a normalization constant and $g(\theta)$ is the emission angle distribution function which is given from simple theory by [82]

$$g(\theta) = \cos \theta \quad (3.4)$$

However, emission is often complicated by the type and grain structure of the target, and the type, energy, and angle of incidence of the sputtering ion. [91,92] For this reason, an arbitrary empirical emission function, $g(\theta)$ can be input into SIMSPUD.

The energy distribution of sputtered atoms can be approximated by the Thompson model developed from collision-cascade theory: [82]

$$f_E(E) dE = C_E \frac{1 - (m + m_g) \times ((E_b + E)/(4m_g m E_i))^{1/2}}{E^2 (1 + E_b/E)^3} dE \quad (3.5)$$

where m_g and m are the masses of the gas molecules and sputtered atoms, respectively; E_b is the binding energy of the target material; E_i is the energy of the incident ions, and C_E is a normalization constant. The ion energy is, itself, derived from a distribution [93,94] which depends on the dc target voltage, V_t . For a magnetron discharge, this distribution is highly peaked near the target voltage and Turner *et al.* [85] argue that it is sufficient to use an averaged value of E_i in determining f_E . For a typical magnetron plasma, the average ion energy was determined to be [94]

$$E_i = 0.733 q V_t \quad (3.6)$$

where q is the electronic charge.

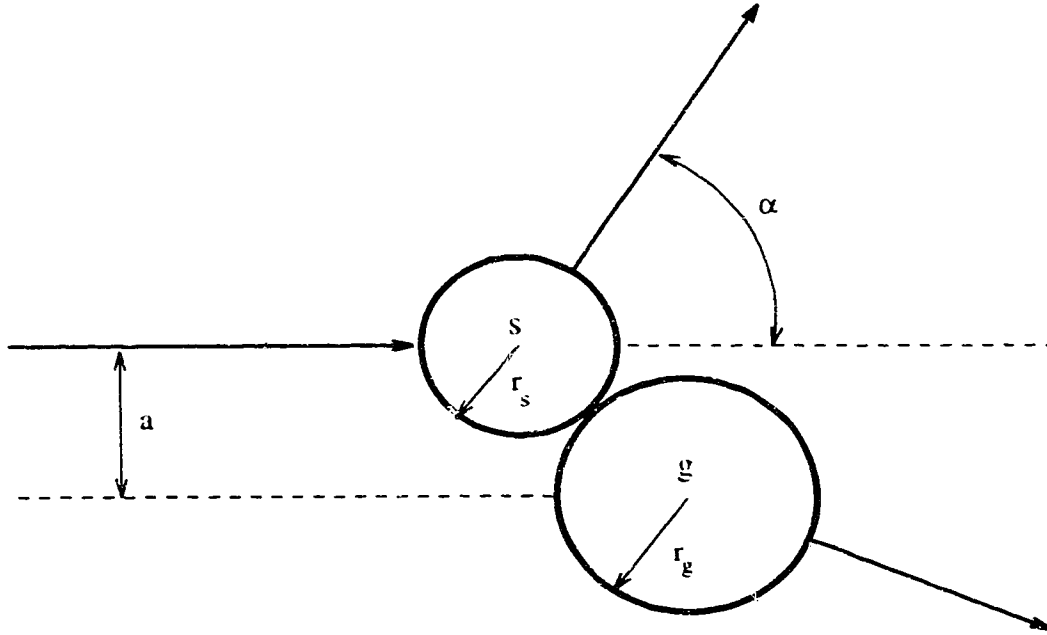


Figure 3.15: Diagram of collision between the sputtered atom (s) incident from the left, and the stationary gas atom (g). The impact parameter, a , determines the scattering angle, α from the initial trajectory.

Ejected particles are assumed to travel a distance, λ , in a straight line between collisions with gas molecules. The free path between collisions, λ , is determined randomly from a Poisson distribution: [80]

$$f_{\lambda}(\lambda)d\lambda = \frac{d\lambda}{\lambda_m} e^{-\lambda/\lambda_m} \quad (3.7)$$

where λ_m is the mean free path.

To simplify calculation of the collision angle (the angle of deviation from the initial trajectory), a binary elastic hard-sphere collision model is used. The scattering angle in the centre-of-mass reference frame for such a model is given by [96,84]

$$\alpha_{cm} = \pi - 2 \arcsin(a/d) \quad (3.8)$$

where a is the collision impact parameter and $d = r_s + r_g$ is the maximum radius

at which the sputtered and gas atoms interact. (The out-of-plane scattering angle, β , is randomly chosen from the interval $[0, 2\pi]$.) This is translated to the laboratory reference frame by the relation [96]

$$\tan \alpha = m_g \sin \alpha_{cm} / (m + m_g \cos \alpha_{cm}) \quad (3.9)$$

For an elastic interaction, the fractional energy change for each collision is given by [84]

$$\frac{E_{final}}{E_{initial}} = \frac{m^2 + m_g^2 - 2mm_g(1 - 2(\frac{a}{d})^2)}{(m + m_g)^2} \quad (3.10)$$

For the hard sphere-model, the impact parameter is equal to the distance from the trajectory of the incident particle to the centre of the gas particle. (See Figure 3.15) It is randomly distributed according to

$$f_a(a)da = \frac{2}{d^2} \begin{cases} a da & , a \leq d \\ 0 & , a > d \end{cases} \quad (3.11)$$

In order to determine a new trajectory (θ', γ') after the collision, the scattering angles must be rotated from relative to absolute coordinates. [97]

$$\cos \theta' = \cos \theta \cos \alpha - \sin \theta \sin \alpha \cos \beta \quad (3.12)$$

$$\cos \gamma' = (\cos \theta \cos \gamma \sin \alpha \cos \beta - \sin \gamma \sin \alpha \sin \beta + \sin \theta \cos \gamma \cos \alpha) / \sin \theta' \quad (3.13)$$

The mean free path between collisions depends on the gas pressure (p) and thermal energy (kT) according to

$$\lambda = \frac{kT}{p\sigma} \quad (3.14)$$

where σ is the collision cross-section. Robinson [98] has shown that σ is energy-dependent and an empirical fit to his computed values in the range of interest to

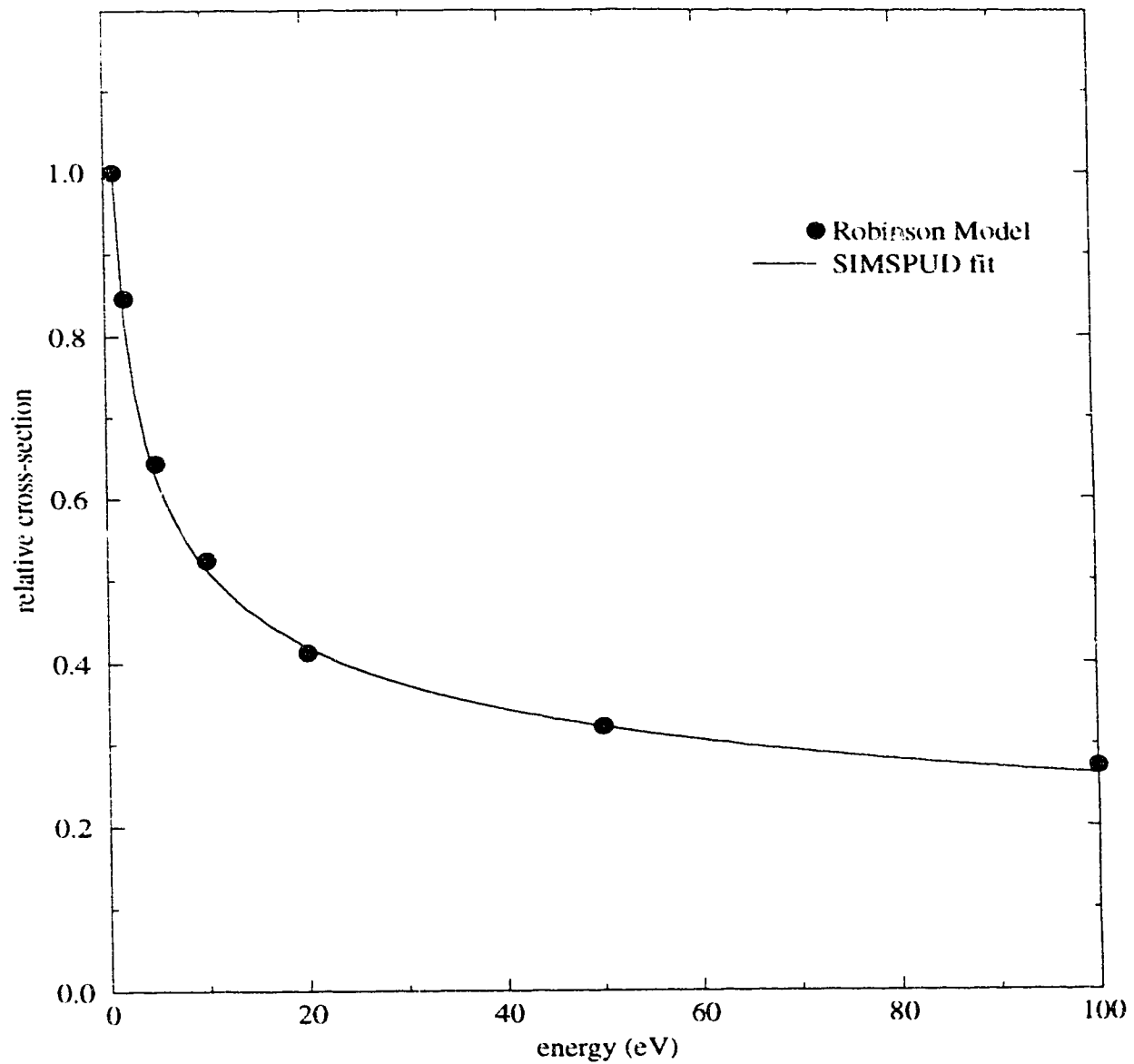


Figure 3.16: Dependence of σ on E in the regime of interest to sputtering according to the model of Robinson. [98] Also shown is the empirical fit used by SIMSPUD, $\sigma(E) = \sigma(E_0)(\frac{E}{E_0})^{-0.29}$.

sputtered particles (1 eV to 200 eV) shows that this dependence can be approximated (at least in the case of Ar-Ar collisions) by a power law: (See Figure 3.16)

$$\sigma(E) = \sigma(E_o) \left(\frac{E}{E_o} \right)^{-0.29}, E > E_o \quad (3.15)$$

where $E_o = 1$ eV. This is the energy below which the particle is presumed to be virtually thermalized, and σ can be approximated using [99,82]

$$\sigma_t = \pi(1 + m/m_g)^{0.5}(r_{st} + r_{gt})^2 \quad (3.16)$$

where r_{st} and r_{gt} are the radii of the thermalized sputtered atoms and gas atoms, respectively.

Only collisions between the sputtered atoms and gas molecules are considered in this model. Collisions with other sputtered atoms or with argon ions or with high energy neutrals are much less frequent [99] and have, therefore, been ignored. Another assumption is that the working gas is homogeneous and at uniform pressure. This ignores the pressure variations which can occur during sputtering due to gas heating. [83]

3.3.1 Algorithmic Details

Using the relations developed above, SIMSPUD can follow the generation and motion of large numbers of atoms from the target to the substrate. Particles that travel behind the target or outside the simulation volume (defined by a cylinder of radius much larger than the target or substrate radii, or the target-substrate separation) are presumed to be deposited onto the chamber walls. Particle trajectories that extend beyond the substrate plane are projected back onto that plane and considered deposited. Histograms can be collected on the energies and incident angles of deposited

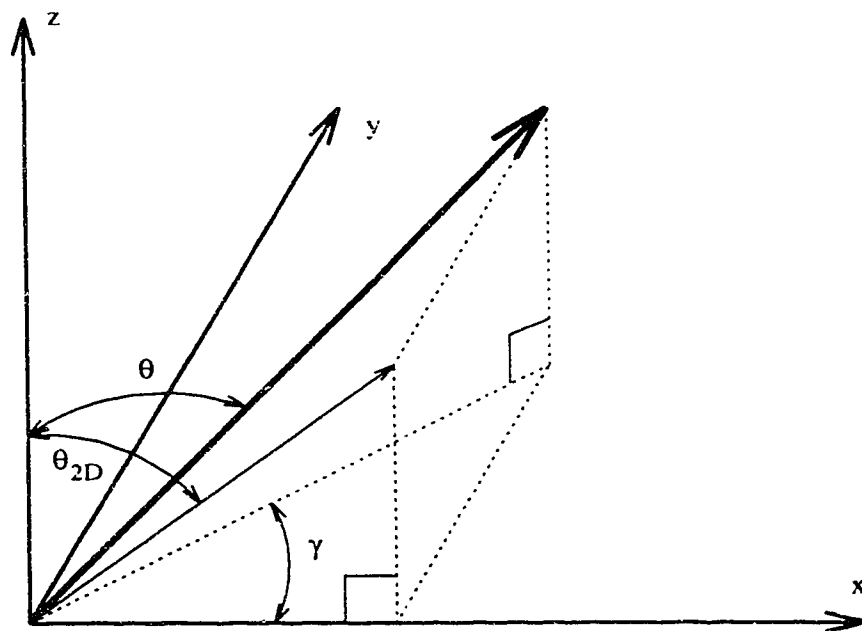


Figure 3.17: Coordinate system for projecting SIMSPUD angular distributions into two dimensions. Particle trajectories are projected onto the x-z plane.

particles falling within a particular region of the substrate plane to estimate angular and energy distributions. Similarly, the radius of particle impact can be binned to determine thickness uniformity, and collection efficiency (number of deposited atoms divided by the number of generated ones) can be computed to measure relative deposition rates. (See Appendix B for description of the SIMSPUD program organization.)

Since SIMBAD is a two-dimensional model, the SIMSPUD angular distribution may require projection into two dimensions before use in SIMBAD. This would be the case for simulating deposition into a long trench, for example, but not for cylindrically symmetric vias (See Appendix A). This projection is accomplished through a coordinate change as shown in Figure 3.17 where

$$\tan \theta_{2D} = \tan \theta \cos \gamma \quad (3.17)$$

A Monte Carlo simulation, such as SIMBAD, depends on generating long sequences of uncorrelated pseudo-random numbers. The algorithm used by SIMSPUD is by Press *et al.* [100] and employs a linear congruent generator with a shuffle table. This provides uniformly distributed pseudo-random values on the interval $[0,1)$. To generate a value, X , from an arbitrary distribution, $f(x)dx$, the uniform random values, ξ , must be mapped through the inverse function [101]

$$X = F^{-1}(\xi) \quad (3.18)$$

where F is the cumulative distribution function

$$F(x) = \int_0^x f(x')dx' \quad (3.19)$$

For user-specified distributions, such as f_P , the integral F is computed numerically and the inverse function is stored in a lookup table indexed by equally spaced values of $\xi_i \subseteq [0,1)$. Interpolation between $F^{-1}(\xi_i)$ for the values of ξ_i bracketing ξ gives the generated value of X . Generators for analytic distributions, such as f_λ , can usually be determined analytically. For example, $F_\lambda(\lambda) = 1 - e^{-\lambda/\lambda_m}$, so random values are given by $\Lambda = F_\lambda^{-1}(\xi) = -\lambda_m \ln(1 - \xi)$

The execution time of the SIMSPUD model is strongly dependent on the ratio z_o/λ_m which characterizes the number of collisions each deposited atom experiences. However, typical execution times are about 10–100 minutes on a Sun SPARCstation 2 workstation.

3.4 Experimental Verification of SIMSPUD

In order to verify the validity of the SIMSPUD model, or to calibrate an unknown parameter such as $\sigma(E_o)$, the simulation results can be compared to those of a pinhole experiment. This primarily tests the angular distribution, which tends to be the most sensitive distribution to parameter values and is the most important to determining many of the film properties.

In a pinhole experiment, (See Figure 3.18) a film is deposited through a small hole in a mask just above the substrate (preferably close enough to it that little scattering would occur between the mask and the substrate). The thickness profile of the resulting film is highly sensitive to the angular distribution arriving at the pinhole. This thickness profile can be directly measured using a profilometer (Tencor Alphastep 200) over steps in the film which have been etched using standard lithographic techniques. With minor modification, SIMSPUD can generate a profile which is directly comparable to the experimental pinhole result.

Figure 3.19a shows a comparison between an aluminum pinhole film deposited at a pressure of 5.1 mTorr and the corresponding SIMSPUD result. Table 3.2 shows the conditions and parameters used. Unfortunately, there are no established values for $\sigma(E_o)$, so this quantity was treated as an adjustable parameter in this comparison. Therefore, in order to make a fair test of the model, the experiment was repeated at 20.1 mTorr using the value of $\sigma(E_o)$ determined at 5.1 mTorr. (See Figure 3.19b). Clearly, there is very good agreement between the experimental and simulated results in both cases which confirms that the model scales correctly.

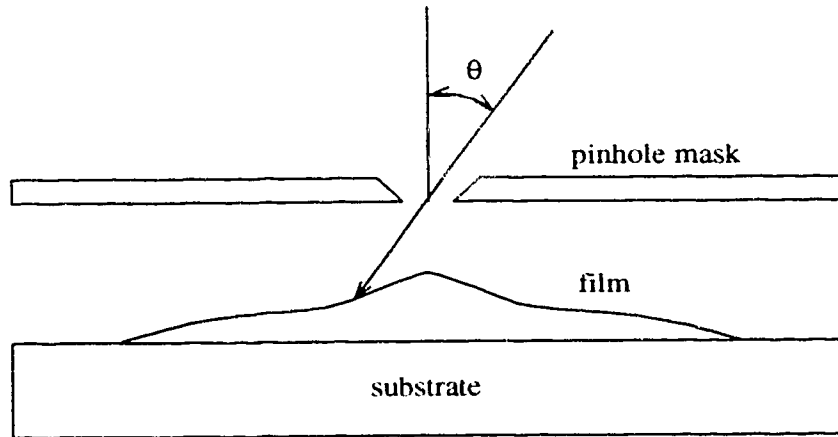


Figure 3.18: Diagram of the pinhole experiment. The thickness profile of the film is strongly dependent on the angular distribution arriving at the pinhole. (The film thickness is greatly exaggerated in this diagram.)

The curves at these two pressures show qualitatively different behaviour because at low pressure there is relatively little scattering and the peak in the pinhole image is off-axis, corresponding to the peak in the target erosion profile caused by the magnetic confinement. At the higher pressure, however, any memory of the sputtering distribution at the target is lost through numerous randomizing collisions in the gas. This shifts the distribution peak to a position along the substrate normal.

In order to test the generality of the SIMSPUD model, this verification process was identically repeated using copper. (See Figure 3.20) Once again, there is very good agreement between the experimental and SIMSPUD profiles. This high level of agreement between the simulation and experimental results makes it appropriate to employ the model in some applications which are of current interest.

Geometry	
Target diameter	5.0 ± 0.1 cm
Target-mask distance	4.78 ± 0.10 cm
Mask-substrate distance	1.34 ± 0.04 cm
Pinhole diameter	0.16 ± 0.01 cm
Pinhole taper	56°
Mask thickness	0.040 ± 0.003 cm
Experiment	
Power (all runs)	400 W
Base Pressure (all runs)	1.4×10^{-6} Torr
Gas flow (5.1 mTorr)	14.7 sccm
Gas flow (20.1 mTorr)	45.9 sccm
Mean voltage (aluminum, 5.1 mTorr)	161 V
Mean voltage (aluminum, 20.1 mTorr)	370 V
Mean voltage (copper, 5.1 mTorr)	458 V
Mean voltage (copper, 20.1 mTorr)	345 V
Substrate	silicon wafer
Model	
Thermal radius (aluminum)*	2.0 Å [47]
Thermal radius (copper)*	2.1 Å [47]
Thermal radius (argon)	1.82 Å [90]
Binding energy (aluminum)	3.39 eV [102]
Binding energy (copper)	3.49 eV [102]
Emission angular distribution (aluminum)	Tsuge [91]
Emission angular distribution (copper)	cosine
Cross-section at 1 eV (aluminum)	50 Å^2
Cross-section at 1 eV (copper)	21 Å^2

*Interpolated Van Der Waals radii

Table 3.2: Experimental conditions and model parameters for the aluminum and copper pinhole experiments. Depositions were performed at both 5.1 ± 0.2 mTorr and 20.1 ± 0.2 mTorr for each material.

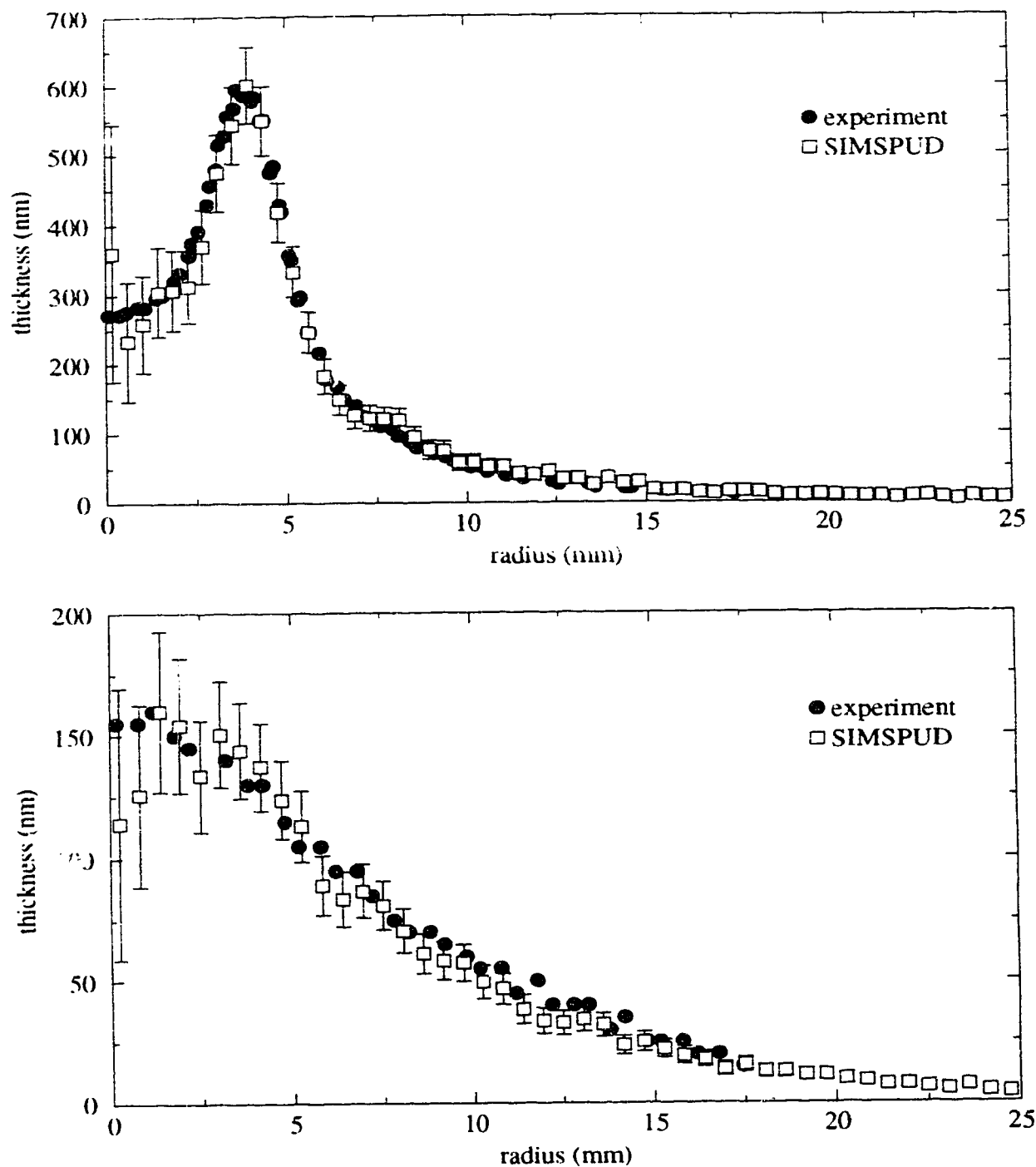


Figure 3.19: Comparison between experiment and model results for aluminum at 5.1 mTorr (top) and 20.1 mTorr (bottom). Error bars on the simulation values correspond to twice the standard deviation. Uncertainty in experimental values is typically less than 5 nm.

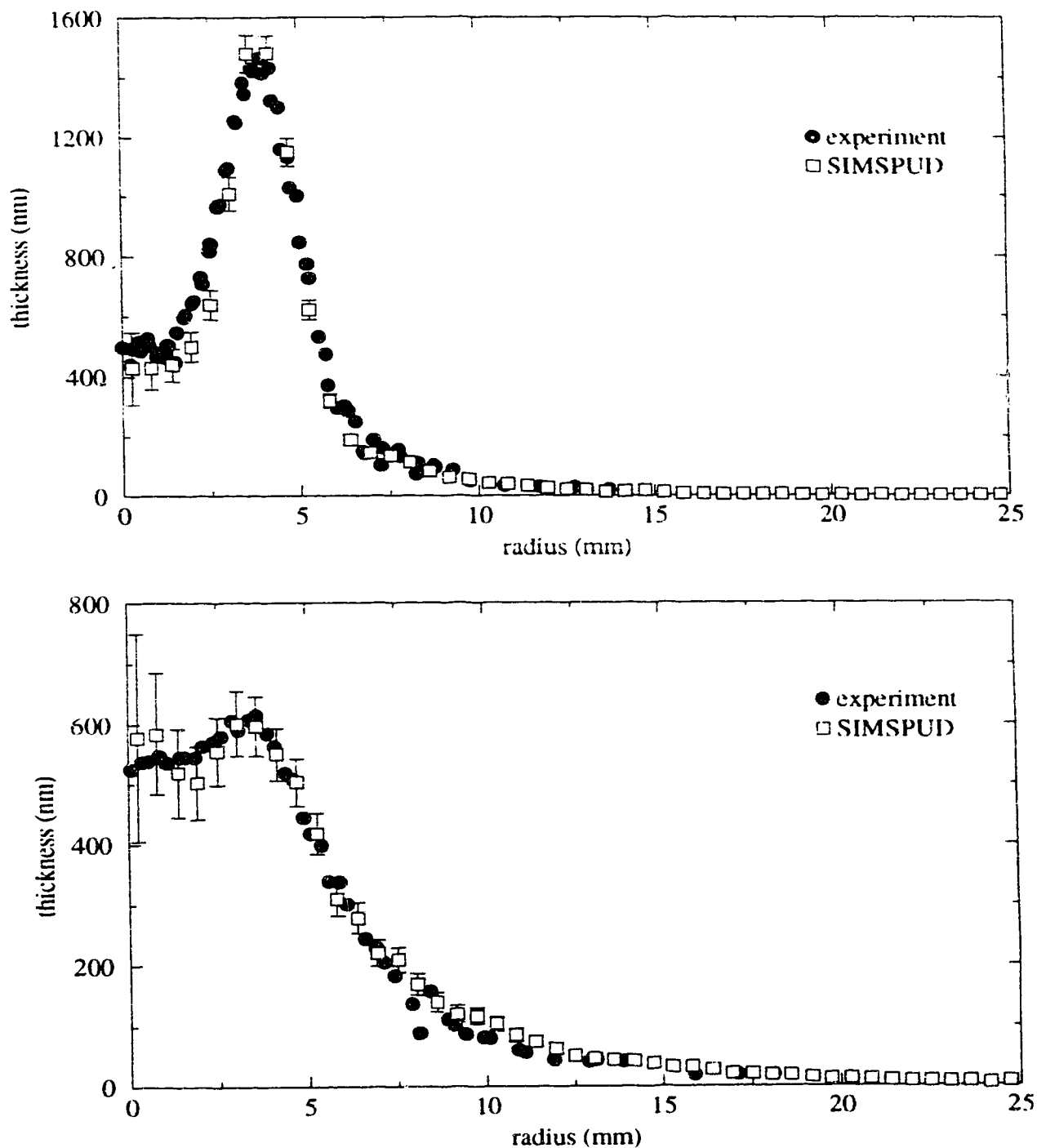


Figure 3.20: Comparison between experiment and model results for copper at 5.1 mTorr (top) and 20.1 mTorr (bottom). Error bars on the simulation values correspond to twice the standard deviation. Uncertainty in experimental values is typically less than 5 nm.

4 Applications of SIMSPUD

There are a variety of possible applications for SIMSPUD/SIMBAD. It can be used for designing magnetron sputtering sources, optimizing deposition parameters such as gas pressure or target-substrate separation, gauging the effects of substrate topography, or predicting film properties. Three examples of such applications are presented below to illustrate the usefulness of the model. The first examines the effect of target-substrate distance on film properties of interest in a production environment. The second looks at the effectiveness of a new magnetron design for uniform target erosion. The third example looks at compositional variations, which the model predicts will result when sputtering from an alloy target.

3.5.1 Target-Substrate Separation

The distance from the target to the substrate is a very important parameter because it determines how both geometric factors and gas scattering will affect the sputtering distributions. For example, Figure 3.21 shows the predicted relative film thickness variation across a 15 cm diameter wafer for a 20 cm aluminum magnetron system at a pressure of 5 mTorr. (These specifications correspond to typical production metallization conditions.) This variation is of concern in microelectronics fabrication because process tolerances are very tight and significant deviations in thickness will reduce yield and reliability. The figure shows that at short distances, such as 40 mm, the thickness profile mirrors the target erosion pattern and the wafer centre is not well coated. Near 60 mm, the film is at its most uniform with slight thinning near the periphery. Beyond 60 mm, the target starts to resemble a point source

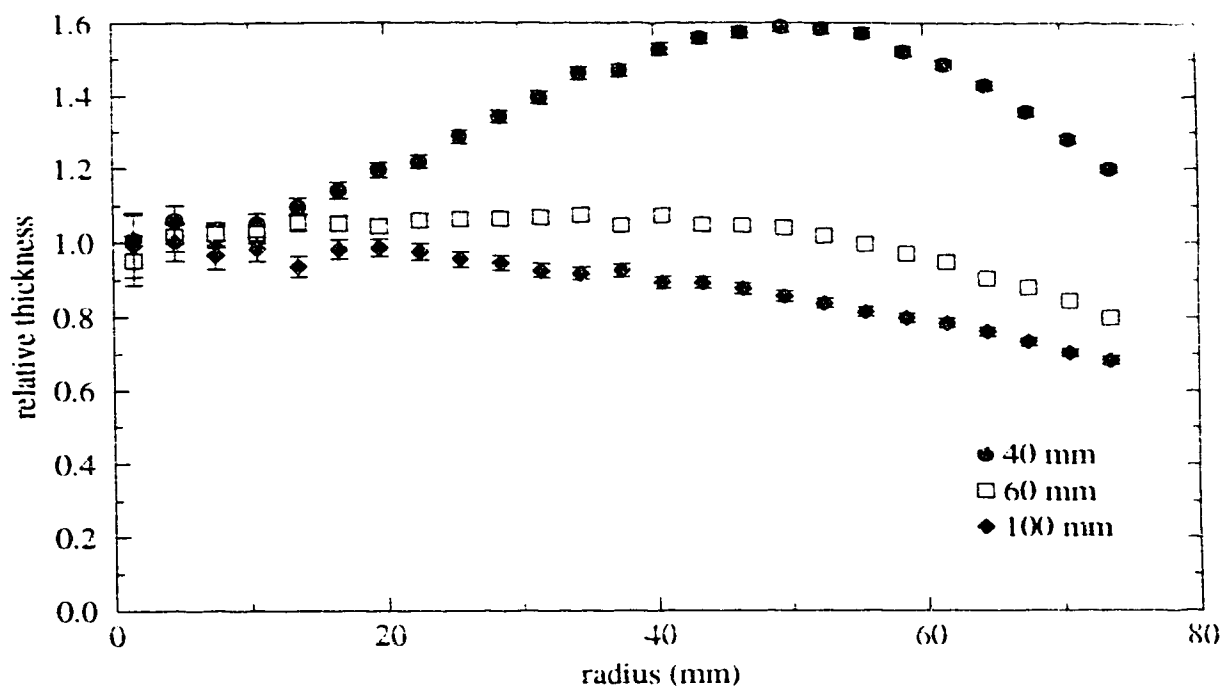


Figure 3.21: Radial film thickness profiles for a 20 cm magnetron source at 5 mTorr for three different target-substrate separations across a 15 cm wafer. Thicknesses are relative to the wafer centre. Error bars correspond to two standard deviations.

at the wafer, and the film thickness drops off monotonically from the centre. To obtain good uniformity outside of the optimal separation range requires substrate motion during deposition which adds cost and complexity to the system and usually generates particles inside the deposition chamber which can reduce yield. The exact value at which the optimal uniformity occurs will vary slightly with details of the target erosion profile and pressure, but this general behaviour is characteristic of conventional magnetron systems.

Another important consideration in a production setting is the deposition rate which affects throughput as well as film quality. Figure 3.22 shows the change in simulated deposition rate (at the wafer centre) with target-substrate separation. There is a

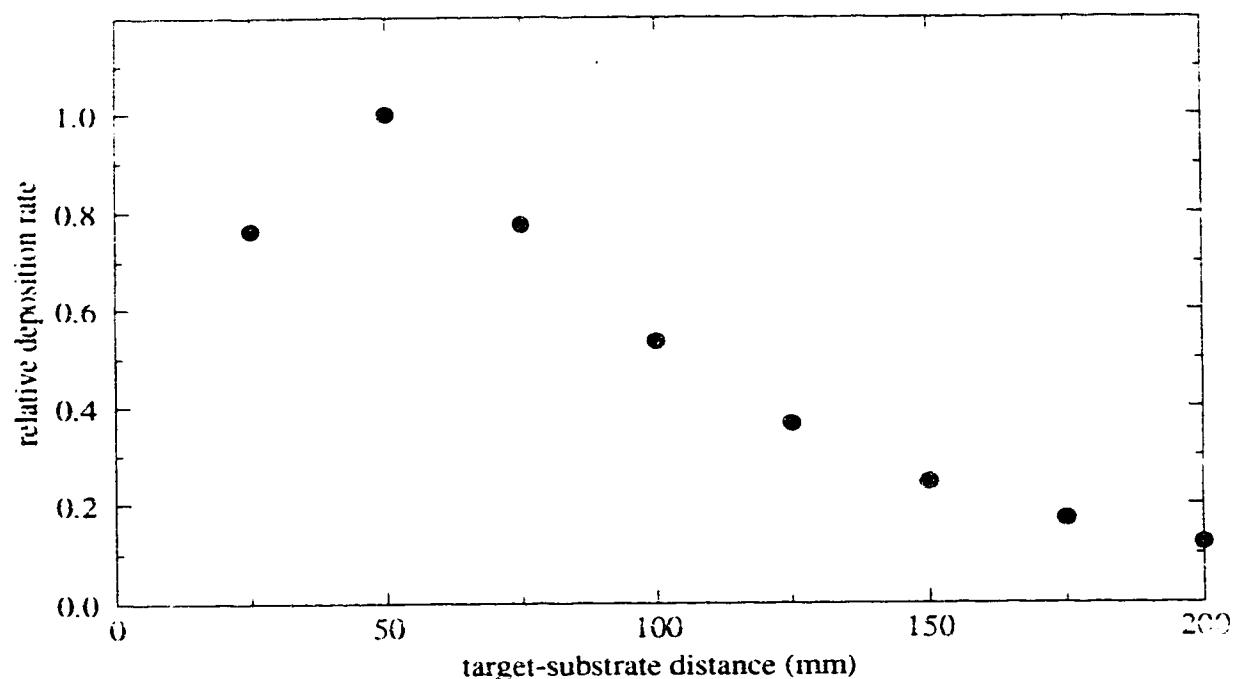


Figure 3.22: The effects of target-substrate distance on relative deposition rate.

substantial drop in deposition flux density as the distance increases due to losses out the sides to the chamber walls and to backscattering. The reason Figure 3.22 shows an initial increase in rate is because little flux can reach the wafer centre from the target erosion ring at very short distances.

Another important factor affecting yield and reliability is the sidewall (step) coverage for high aspect ratio topography. The variation of this with target-substrate distance for a 1:1 aspect trench is shown in Figure 3.23. At small separations, step coverage is poor because the incident angular distribution is too broad for much flux to travel well into the via. As the separation increases, the distribution narrows, and step coverage increases as more flux reaches the sidewalls at the critical regions near the bottom of the feature. As the distribution becomes too narrow, however, the sidewalls

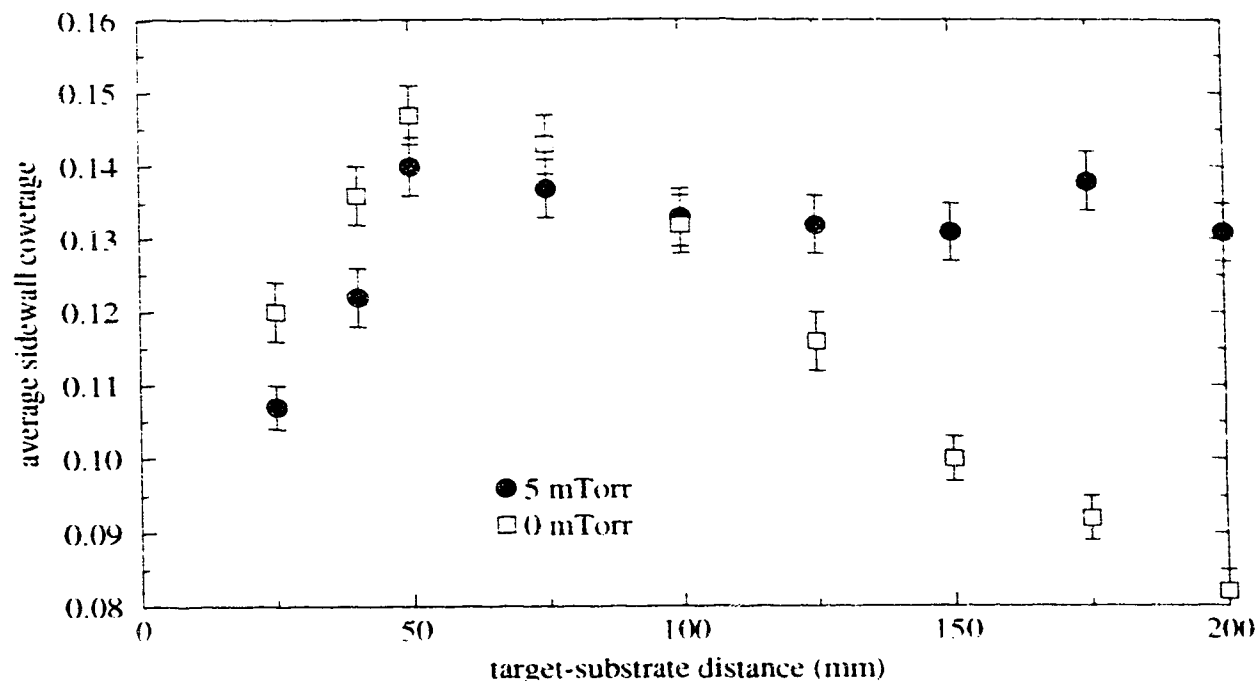


Figure 3.23: The effects of target-substrate distance on average sidewall coverage are shown for 5 mTorr pressure, 20 cm Al target, and 1:1 aspect ratio topography.

present a very small cross-section to the flux and coverage starts to fall off. Under the conditions examined here, however, this diminution is forestalled by increased gas scattering which tends to broaden the angular distribution at larger separations. The importance of this scattering to sustaining step coverage at larger separations can be seen by comparing with the zero pressure coverage (also shown in Figure 3.23), which peaks and then steadily drops as there is no scattering.

Another quantity that varies with target-substrate separation is the average energy of incident atoms. This is of interest to film quality since it affects microstructure factors such as column and grain size. As Figure 3.24 shows, the average energy decreases monotonically with distance as the average number of collisions with gas

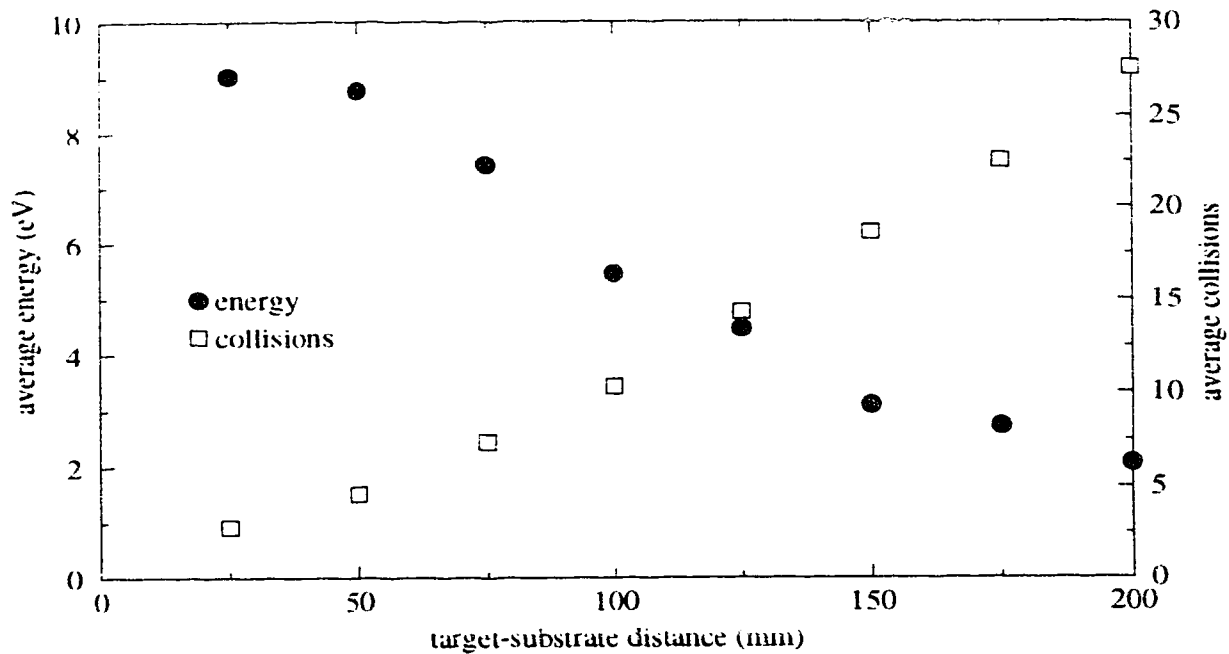


Figure 3.24: The effect of target-substrate distance on the average adatom energy (left axis) and average number of collisions with gas molecules (right axis).

molecules increases. The number of collisions is not linear with distance because, as the energy decreases, so does the mean free path between collisions due to the energy dependence of the collision cross-section.

In summary, for this application, the preferred target-substrate separation would be near 60 mm since this corresponds to almost peak deposition rate, uniformity, and step coverage, and still maintains a high average incident energy. However, this may be a fortuitous case, and different pressures, targets, or substrate topography may present less ideal solutions. Also, it should be pointed out that even the peak coverage obtained by optimizing the angular distribution is still poor. This implies that for this aspect ratio, either the sidewalls must be tapered (which dramatically improves step coverage but increases the effective size of the via) or one of the deposition processes

discussed in subsequent chapters will be required.

3.5.2 Swept Field Magnetrons

Recently, microelectronic equipment vendors have introduced magnetron sources which employ moving magnets to sweep the confined plasma across the target in order to obtain uniform target erosion. [103] This has the advantage of extending the target lifetime and providing a stable (flat) target surface profile at all times. However, the effects of this novel magnetron configuration on factors such as uniformity and step coverage have not been thoroughly examined. SIMSPUD and SIMBAD can be used to make some comparisons between the moving magnetron and conventional magnetron configurations.

For example, Figure 3.25 shows the variation in relative thickness across the wafer for a 20 cm aluminum target with a moving magnetron source. Profiles for three different target-substrate separations are shown which can be directly compared with those in Figure 3.21 for the conventional magnetron design. There is very little variation in thickness uniformity with target-substrate spacing for the new magnetron in comparison with the conventional one. This allows for greater flexibility in choosing the spacing to optimize another film property such as step coverage. On the other hand, the best uniformity that can be obtained with the moving magnetron is not as good as the best result with the conventional one. Conceivably, one could use SIMSPUD to tailor the swept magnet design so that the film uniformity could be improved further. (Of course, the erosion profile would then no longer be uniform.)

One important benefit of the new magnetron design is improved coverage uniformity

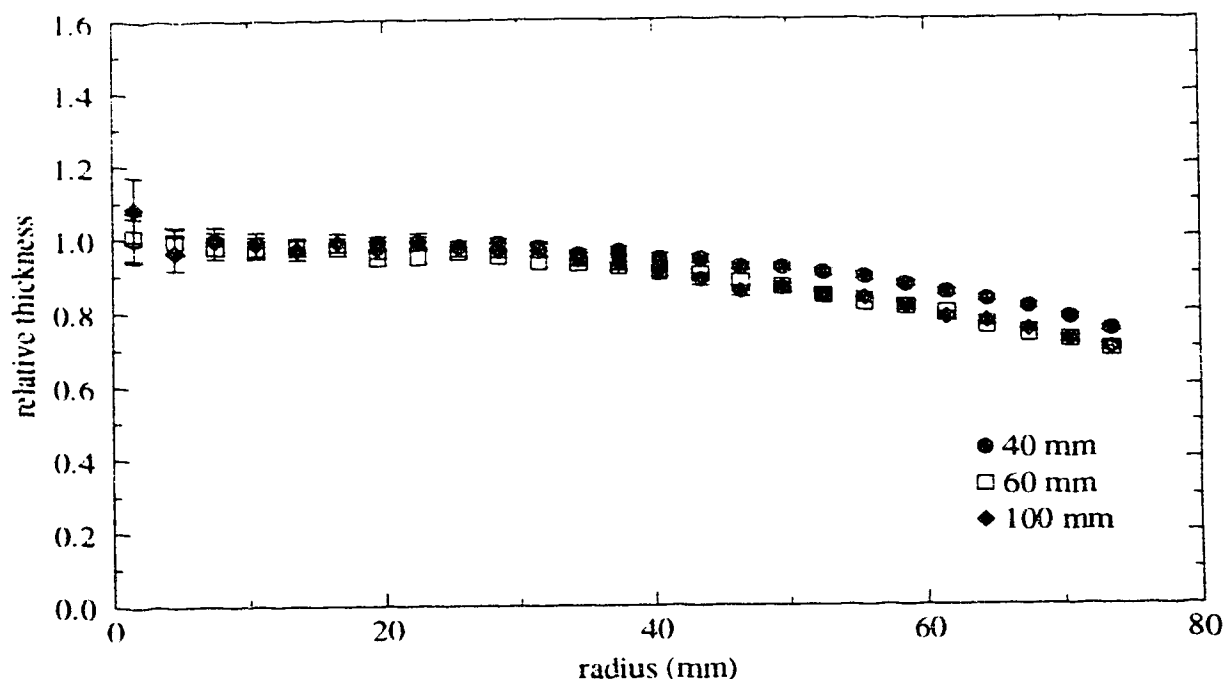


Figure 3.25: Radial film thickness profiles for a 20 cm swept field magnetron source at 5 mTorr for three different target-substrate separations for a 15 cm wafer. Error bars correspond to two standard deviations.

across the wafer. Typically, deposition off of the central axis of the sputter source results in asymmetric coverage. This reduces yield and reliability near the edge of the wafer and must be minimized as much as possible. Figure 3.26 shows that the off-axis coverage resulting from the moving magnetron (Figure 3.26a vs. b) is decidedly less asymmetric than that from the conventional one (c vs. d). The deposition conditions used for this figure are comparable to those used above (20 cm aluminum target, 50 mm target-substrate spacing, 5 mTorr pressure).

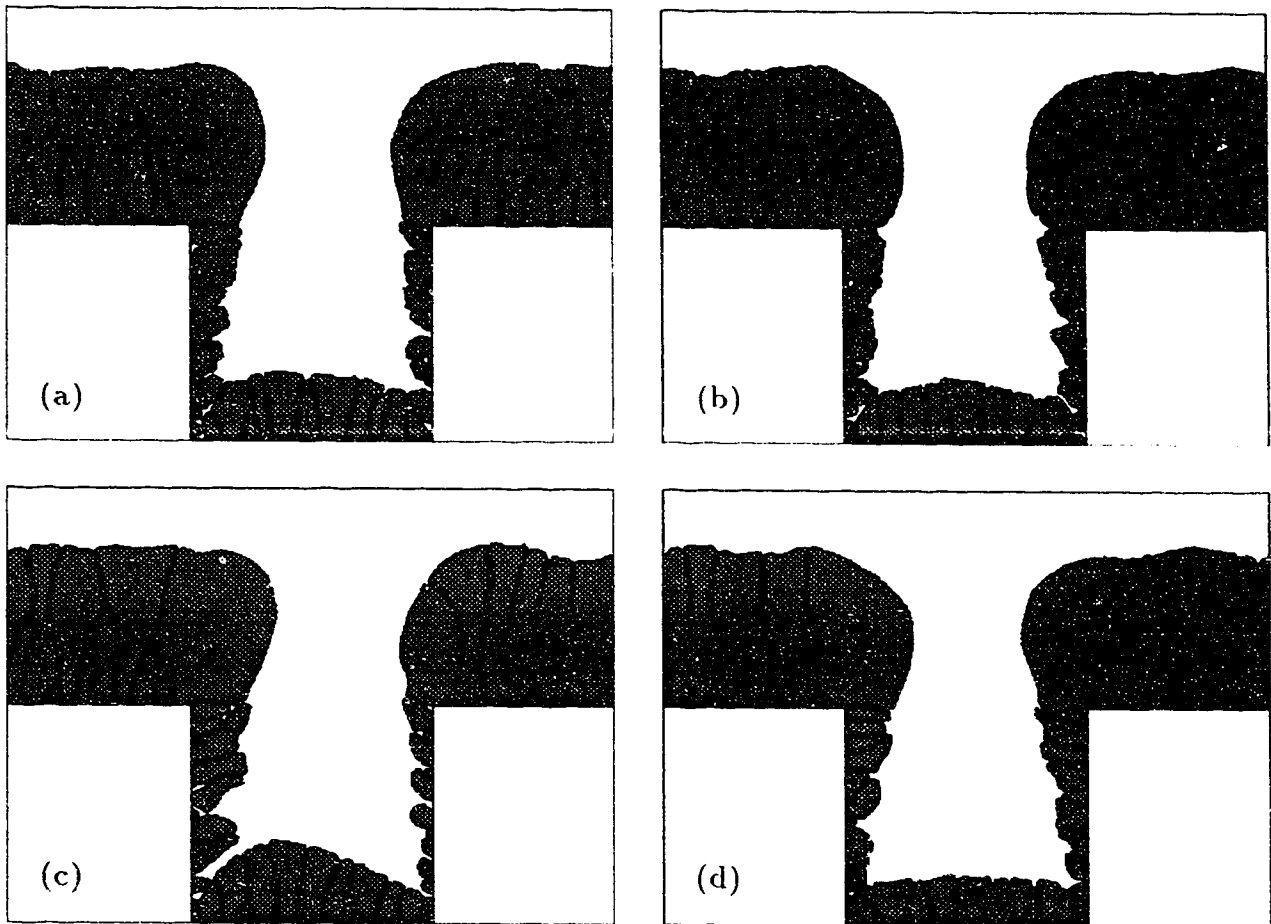


Figure 3.26: The effect of magnetron design on off-axis step coverage uniformity. Film deposited using a moving magnetron at radii of 70 mm (a) and 0 mm (b) can be compared with those from a conventional one at 70 mm (c) and 0 mm (d).

3.5.3 Alloy Sputtering

That the incident sputter distributions for copper and aluminum are different is evident from the simulation and experimental data shown in Figures 3.19 and 3.20. This suggests that aluminum and copper sputtered from an alloy target (such as is increasingly being used for metallization layers) would not necessarily be deposited in the same relative concentration across a wafer or over topography. If present, these compositional variations could be quite important to metallization reliability as electromigration resistance is sensitive to copper content. [14] Obviously, such compositional variations would not be limited just to aluminum-copper alloys. This effect would be expected for any alloy whose constituents have different scattering characteristics due to differences in atomic mass or collision cross-sections.

Figure 3.27 shows a map of simulated copper concentration in a Al-Cu(4%) alloy film deposited over a 1:1 aspect trench. (This nominal copper concentration is arbitrary. The simulated relative variations should be representative for any minority concentration.) The angular distributions used to generate this result correspond to the 5.1 mTorr results presented above. Pronounced variations in stoichiometry are clearly predicted under these conditions. In fact, the average sidewall concentration is reduced to $73 \pm 5\%$ of nominal, and along the bottom of the via it is raised to $126 \pm 5\%$. The minimum and maximum values at these locations would deviate even further from the desired composition. At the higher pressure of 20.1 mTorr, these values are slightly closer to the optimal at $90 \pm 5\%$ and $124 \pm 6\%$, respectively.

These simulation results are based on the assumption that the sputter distributions

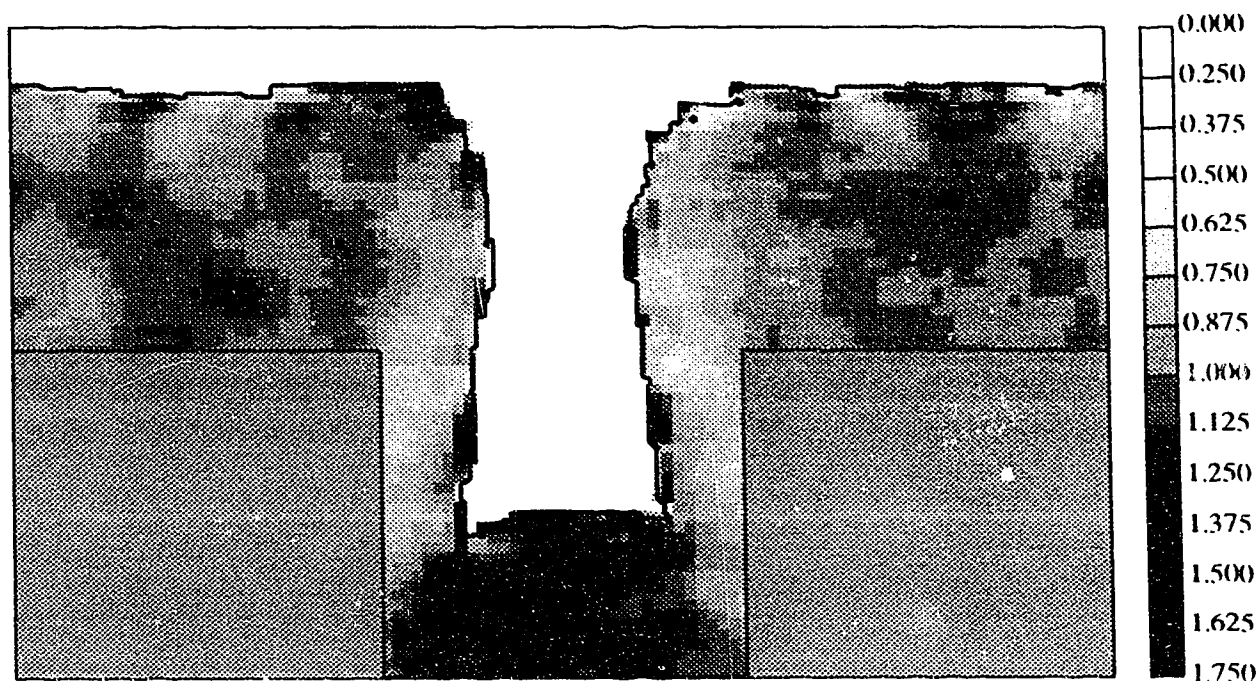


Figure 3.27: The simulated variation of copper concentration in a Al-Cu alloy film deposited over a 1:1 aspect feature. Sidewall concentration is reduced and bottom concentration is enhanced. The legend bar indicates percentage concentration.

for a compound target can be predicted by the superposition of the results for individual targets. While this is likely true for aluminum if there is only 4% copper in the alloy, it is much less clear that the emission properties of copper will be unaffected by the majority of aluminum. However, similar simulations using the emission angular distribution, $g(\theta)$, of aluminum for the copper in the alloy do yield similar results, which suggests that this effect is not primarily dependent on the emission conditions. Also not included in this simulation is the effect surface diffusion may have in redistributing the copper once it is deposited. At relatively high deposition temperatures, this may be a significant factor.

If composition varies over topography, it may also vary across the wafer — as has

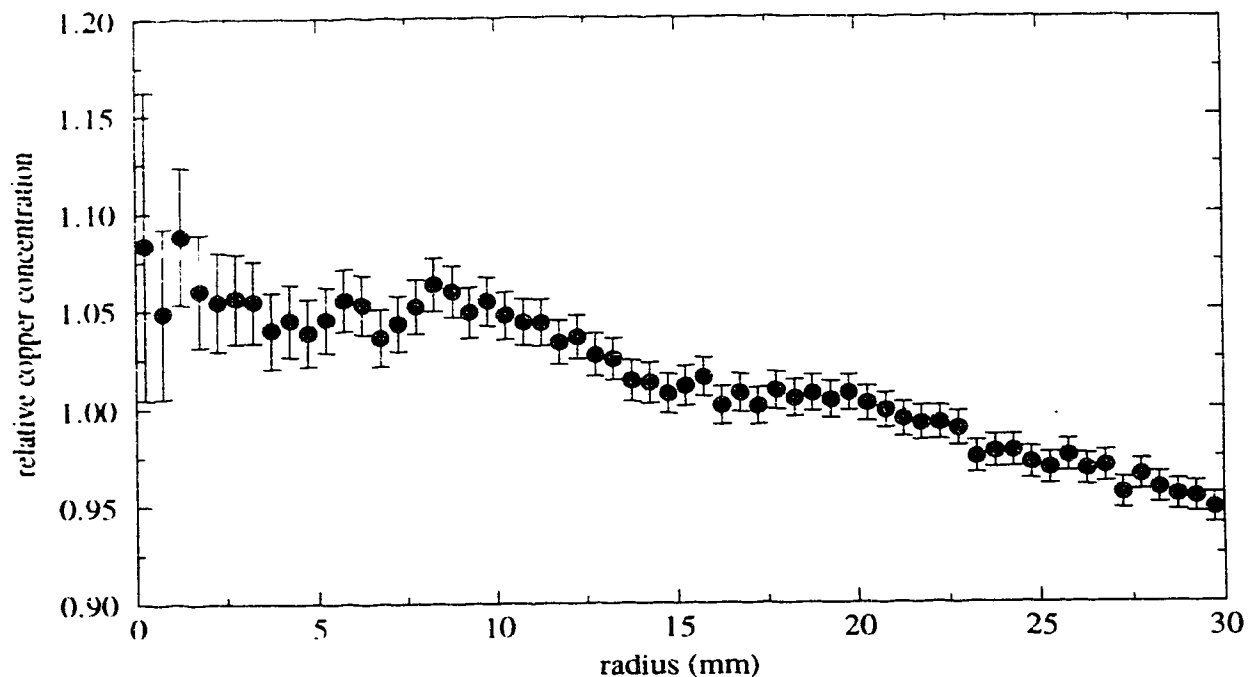


Figure 3.28: The predicted relative variation in copper concentration in a Al-Cu alloy film across a 6 cm wafer. The wafer centre is copper-rich while the edges are deficient in that element.

been suggested by Rossnagel. [83] Figure 3.28 shows this radial variation across a 6 cm wafer as predicted by SIMSPUD for the conditions described above at 5.1 mTorr. There is, indeed, a trend from excess copper in the centre of the wafer to a copper deficiency at the periphery. However, the magnitude for this variation is much less than that which is predicted for the variation over topography under the same conditions. Nonetheless, these two effects are additive, and variations across the wafer will exacerbate those over topography and contribute to premature electromigration failure.

3.6 Summary

The SIMSPUD model has been developed and verified experimentally using a pinhole image technique for both sputtered copper and aluminum. When combined with SIMBAD, the model provides a powerful tool for tailoring and optimizing sputtering distributions to improve coverage, uniformity, microstructure, and composition. The model predicts improved uniformity for moving magnetron sources over conventional ones, compositional variations for sputtered alloys, and an optimal target-substrate spacing for a typical production scenario. However, the model indicates that even optimized distributions cannot provide satisfactory coverage on vertical sidewalls as topography aspect ratios approach 1.

Chapter 4

Bias Sputtering¹

4.1 Introduction

As demonstrated in the previous chapter, it is possible to tailor sputter distributions to improve film properties such as step coverage. However, at higher topography aspect ratios, this approach becomes less effective and alternate ones must be developed to enhance coverage. One such technique which has had initial success in enhancing the coverage of metallization layers is bias sputtering. [104-107] Under ideal conditions, completely planarized features (completely filled to the top surface level) have been obtained. [104-106] Such planarization is attractive, not only because of the ideal conduction capabilities, but also because it makes subsequent photolithography and deposition simpler.

The key to bias sputtering is ion bombardment of the film during deposition. These ions cause resputtering of the film which reduces the net deposition rate. However, film atoms which are re-emitted from inside topography such as vias or trenches are likely to be intercepted and redeposited elsewhere inside the feature, whereas atoms resputtered from the top surface of the film are usually lost. This results in net enhancement of relative deposition rate inside topography, which generally improves

¹The material in this chapter has been published as references [72,73].

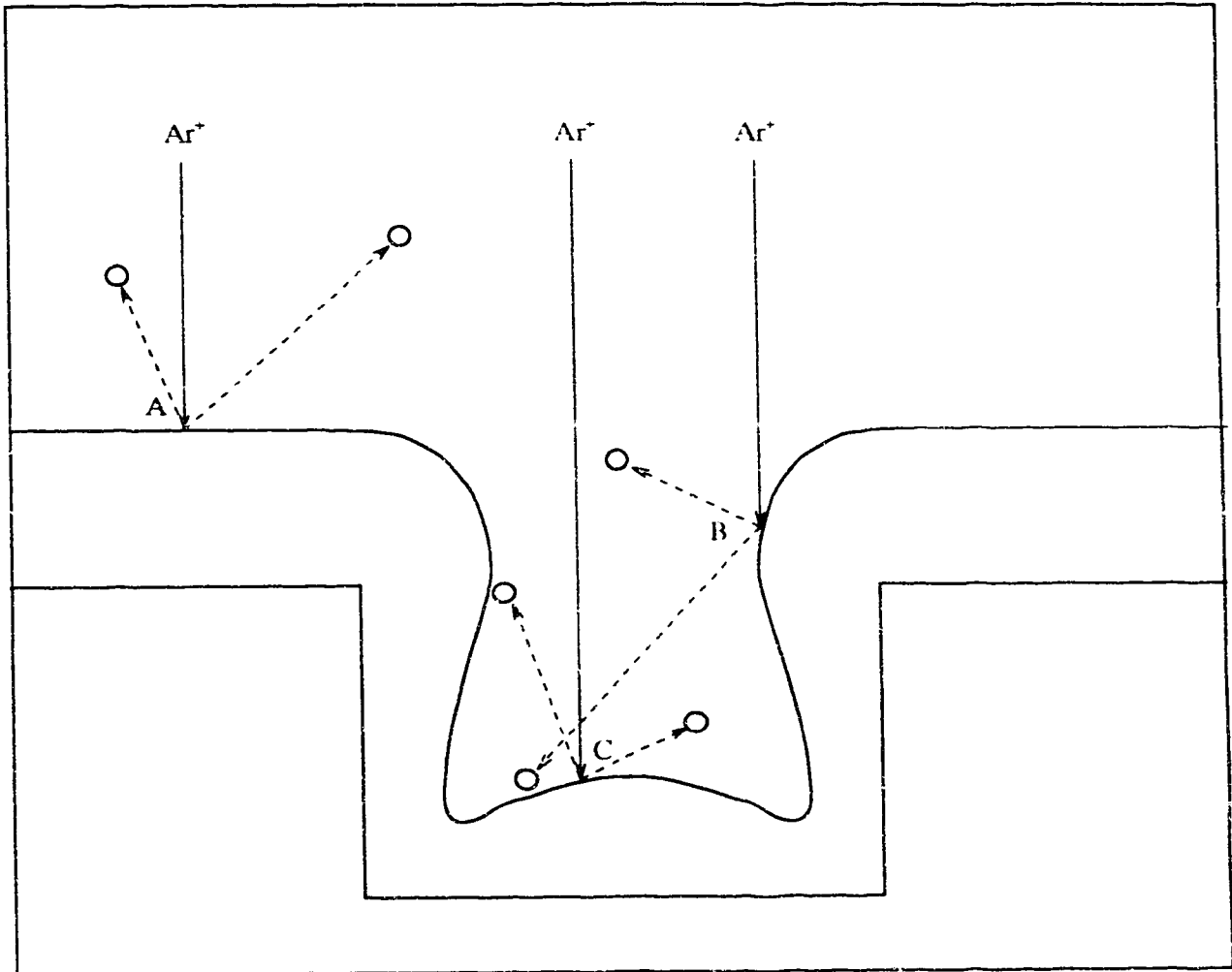


Figure 4.29: Ion bombardment during deposition causes film resputtering which reduces deposition rate. However, resputtered film material from the top surface (A) is usually lost while material from within topography (B and C) often redeposits within the same feature, thereby increasing the net relative deposition rate along the sidewalls. This results in improved step coverage.

step coverage. (See Figure 4.29.)

In bias sputtering, the ion bombardment is generated by applying an rf (radio-frequency) voltage to the substrate holder to create a glow discharge plasma at the substrate. (See Figure 4.30.) Due to the difference in mobilities between ions and electrons in this plasma, the substrate holder develops a negative dc bias voltage to retain charge neutrality. [24] This net voltage causes positively charged argon ions in the plasma to be accelerated toward the substrate and strike the growing film. Typically, the bias voltage is between -100 V and -2 kV. [16,24] (A dc bias could also be applied for a similar effect, but to sustain a dc discharge at the substrate generally requires higher energies which can be detrimental to the film.)

In addition to resputtering, the ion flux striking the film can cause a number of other events to occur. For example, the ions may be reflected off the film surface (particularly if they are incident at glancing angles), or, due to their high energies, they may become implanted into the film and cause argon gas incorporation, or they may transfer that energy to the film atoms and cause surface relaxation and diffusion. All of these effects (with the probable exception of gas incorporation) can affect the film coverage and microstructure.

As with any new metallization process, it is desirable to have a process model in order to better understand its sensitivities and to help optimize its parameters. The best such model so far is that of Bader and Lardon. [108,109] However, this model is based on a string algorithm so it cannot provide microstructure or density information. It also does not consider the effects of ion reflection or surface diffusion which can be very important. In addition, the effects of gas scattering on the incident angular

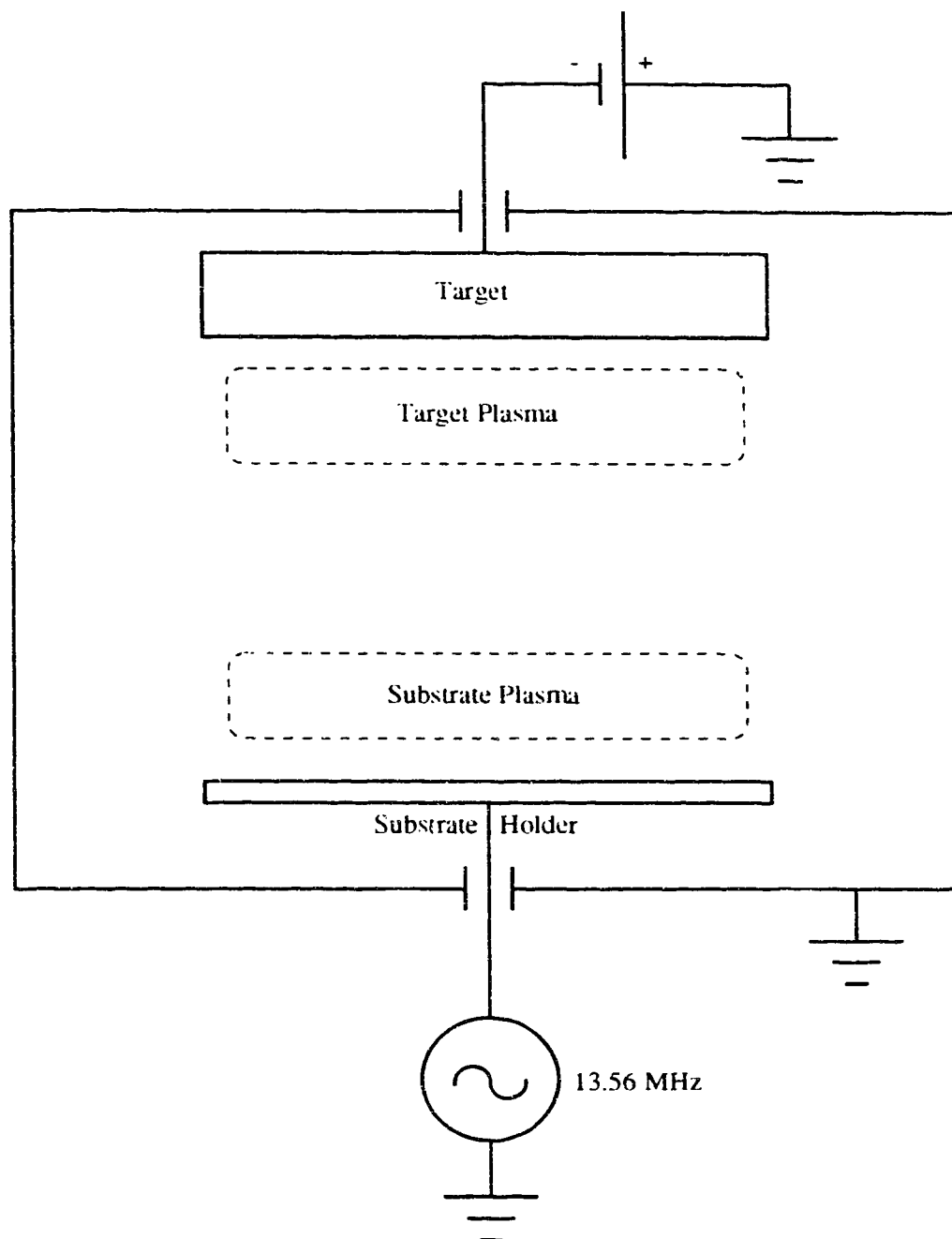


Figure 4.30: Schematic description of bias sputtering. Radio-frequency power applied to the substrate holder creates a discharge and net negative dc bias there. This causes argon ion bombardment of the substrate in a manner similar to that occurring at the target.

distribution of the sputtered flux (which were seen in the previous chapter to strongly affect step coverage) were not incorporated. Because of these shortcomings, it is desirable to extend the SIMBAD model to simulate bias sputtering.

4.2 SIMBAD Bias Sputtering Model

In order to extend the SIMBAD model to simulate bias sputtering, it is necessary to generate ion discs as well as film ones. These ion discs represent averages of many individual ions in the same manner that film discs represent many film atoms. However, unlike the film discs, the ion discs are not incorporated into the film. Instead, they act on the aggregated film discs to redistribute or rearrange them.

Under typical bias sputtering conditions, the ions are not scattered during their acceleration toward the substrate. This means they arrive at angles very close to normal incidence to the wafer and with energies close to the bias voltage. [108,110,111] Therefore, when generated in SIMBAD, the ion discs are assumed to be mono-energetic and uniformly incident at the wafer normal angle.

Like the film discs, the ion discs follow straight line trajectories until they strike the film. Once the point of impact is determined, an ion can reflect off the surface, and/or resputter the struck film disc, and/or cause local film surface relaxation. Which of these fates occurs depends largely on the ion energy and angle of incidence relative to the local film surface normal.

The probability of an ion (and the corresponding ion disc) reflecting off the film depends on its energy, angle of incidence, and mass relative to the atoms in the reflecting

surface. [112, 113] Unfortunately, the details of this dependence have not been well investigated – particularly in the energy regime of interest to bias sputtering. [112] The ion reflection model used by SIMBAD is based on calculations made by Hou *et al.* [113] using the program, MARLOWE. Their results show the ion has a very high probability of reflection above a critical angle (for example, that angle is 77° for 3 keV argon ions striking copper). Below this angle, there is a relatively narrow transition to very low reflection probabilities. Within that transition regime, a linear dependence is used by SIMBAD to approximate the MARLOWE results. (Another model capable of predicting ion reflection probabilities, TRIMSP, [112] has qualitatively similar results.) If the ion does reflect, a specular reflection angle is assumed. (The angle of reflection equals the angle of incidence relative to the local surface normal.) A result of this reflection behaviour is the ion etching of small trenches at the base of steeply angled features during bias sputtering as extra ions are reflected there. (See Figure 4.31)

The probability of the ion causing film resputtering is directly proportional to the ion sputtering yield. Like the reflection probability, the sputter yield depends on the ion energy, the angle of ion incidence, and the material being bombarded. [92, 114] Fortunately, there is somewhat more experimental characterization of this dependence which usually makes it possible to employ empirical sputter yields in SIMBAD. Figure 4.32 shows the typical angular dependence of yield increasing with angle as more of the ion's energy is transferred to the surface atoms since the ion does not penetrate as deeply into the film. The trend reverses at higher angles, however, as the probability of ion reflection increases. [114] This angular dependence is important to bias sputtering since the average angle of incidence and, hence, average sputter

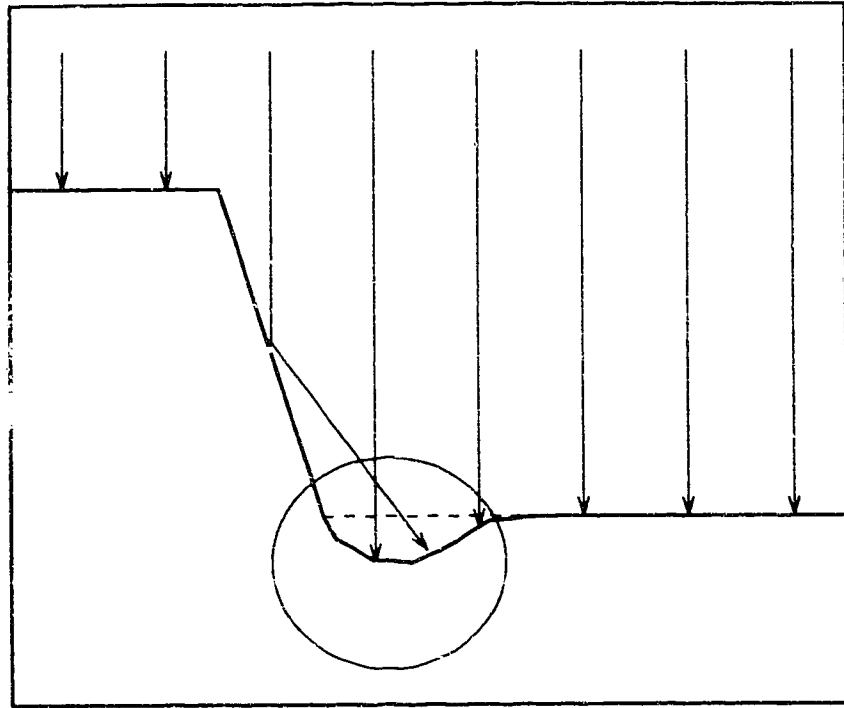


Figure 4.31: Reflection of ions off steeply angled features increases relative ion impingement at the feature base (circled region) and causes trench formation.

probability will vary over topography. In SIMBAD, the ions are assumed to be mono-energetic and an empirical angular-dependent sputter yield should be used which is appropriate for that energy and film material.

If a resputtering event does occur, then the emission angular distribution must be considered. This function also depends on the ion energy and incident angle as well as the material and surface properties. [116] At high energies, the ion penetrates deeply into the material and the emission distribution is close to a cosine. [116,92] However, at typical bias sputtering energies, there is a large component of the emission distribution in the specular direction. [116,92] In bias sputtering, this preferential emission causes material on sidewalls to tend to resputter further into the topography and thereby

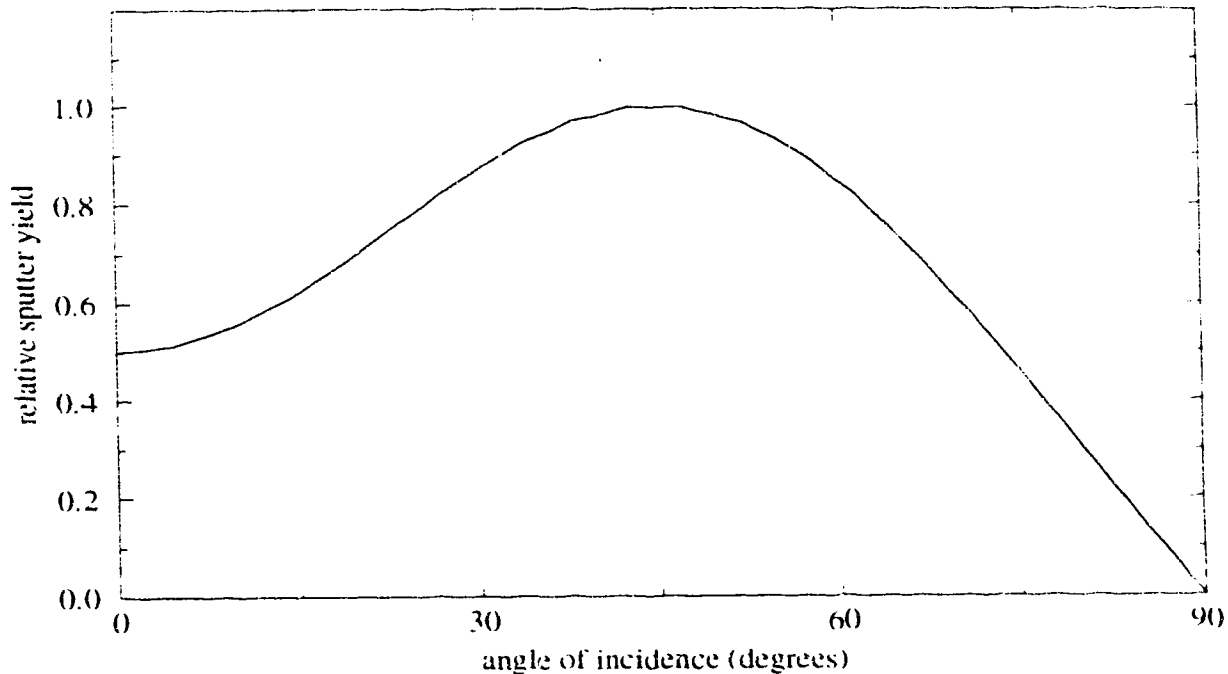


Figure 4.32. Angular dependence of sputter yield for aluminum. [115]

help to fill and planarize it. Unfortunately, there is little empirical data to quantify the angular dependence for the emission distribution. [92] Probably the most useful of this data is from Tsuge *et al.* [91] The emission angular distribution used in SIMBAD is an empirical function which is based on Tsuge's data for aluminum. (See Figure 4.33) An alternate source of information might be the simulation results from the program TRIMSP. [112]

The final ion bombardment effect that must be included in SIMBAD is ion-induced surface diffusion. Each time an ion strikes the film, it transfers some energy to it which can cause diffusion of the surface atoms. This effect is incorporated into the SIMBAD model by locally diffusing the film discs in the immediate vicinity of the one which is struck by the incident ion, after any resputtering has occurred to allow

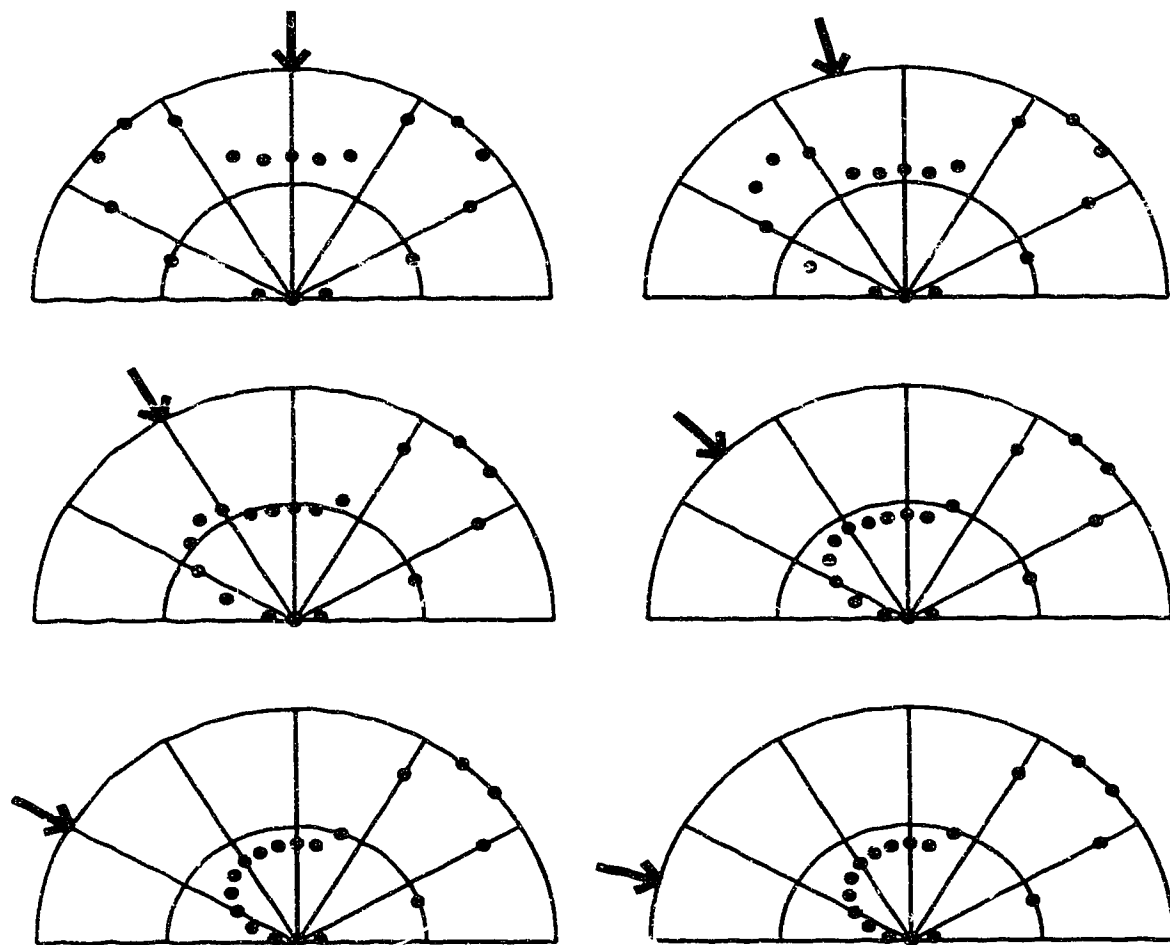


Figure 4.33: Polar plots of the resputter angular distributions used by SIMBAD. The angle of ion incidence is indicated in each plot by the arrow. This empirical dependence is based on data by Tsuge *et al.* [91]

for surface relaxation. (Since SIMBAD does not currently represent individual film grains, the impact of this ion bombardment on grain size is not modeled. However such ion bombardment effects are reported. [117])

One factor not included in SIMBAD is argon incorporation. Argon concentration in the film is known to increase with substrate bias [117] which can affect film properties such as resistivity. The impact of this incorporation on film coverage and columnar microstructure, however, is likely to be minor.

Many of the events that can occur when an ion disc strikes the film depend on the local surface normal. In a discrete simulation such as SIMBAD, this surface is not well defined and must be determined by averaging the surface near the impact point over an appropriate length scale. This length must be large enough that the surface is well defined, but small enough to be relevant to the local conditions at the impact point. An effective compromise length was found to be 10–15 disc diameters. This represents only about 2% of the total surface length for a typical simulation, so the value obtained does reflect a localized surface normal. However, lengths much less than this resulted in an unacceptably broad distribution of surface normals which average out variations in sputter yield over topography. Figure 4.34 describes the SIMBAD surface normal algorithm.

The SIMBAD bias sputtering model executes more slowly than the basic deposition model for a given film thickness as more particles are involved. Under high bias conditions, this could be by a factor of 2 to 3.

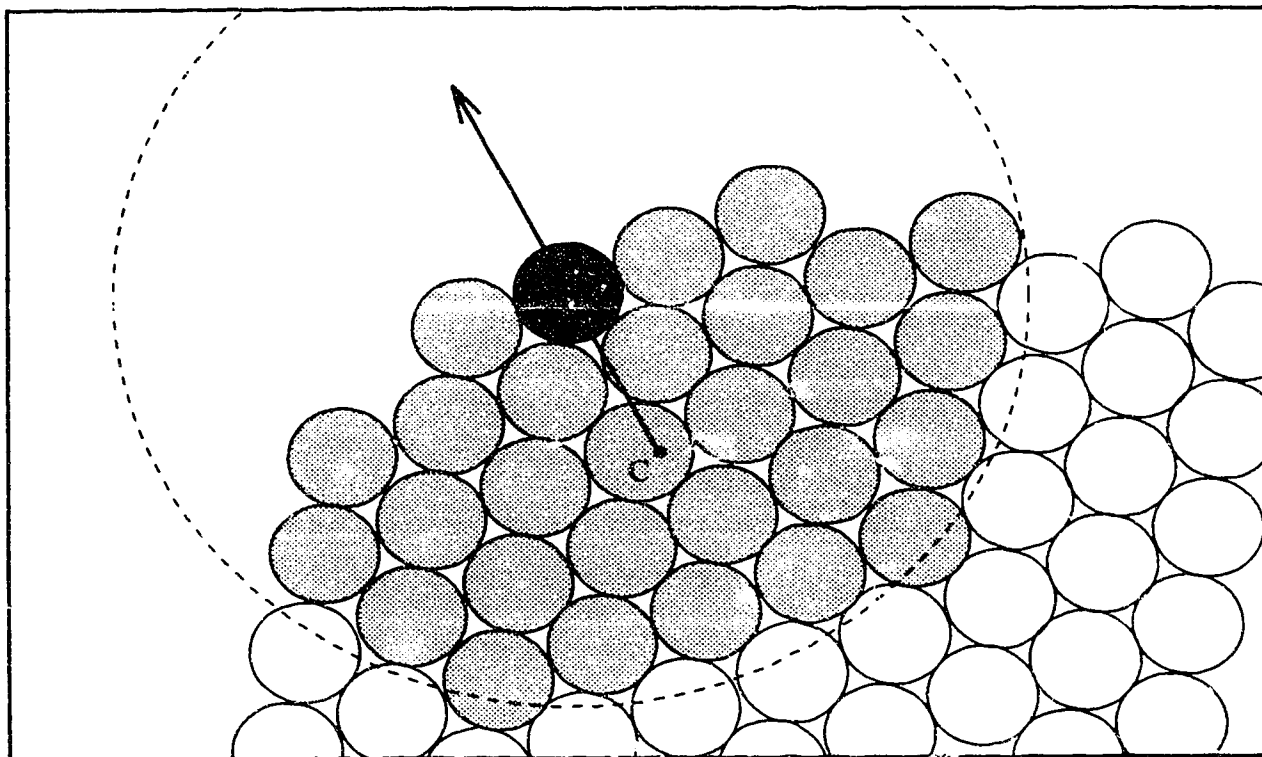


Figure 4.34: The surface normal of a disc (dark grey) whose centre is at P is given by the vector through P from the center of mass (C) of all discs (light grey) whose centres are within a given radius of P . The size of this selection radius determines the amount of surface averaging.

4.3 Experimental Verification

In order to verify the results of the SIMBAD bias sputtering model, a series of tungsten films were deposited with varying levels of substrate bias and compared to the SIMBAD depictions. The sputtering system used for this work was a three target MRC 8620 rf diode system. The rf diode sputter source is similar to the magnetron one described earlier, but it lacks the magnetic confinement to enhance efficiency and uses rf power to develop a dc bias at the target in the same manner as it is employed at the substrate. This arrangement allows a single power supply to be split to apply rf power to both the target and the substrate.

In all depositions, the target power was maintained at close to 200 W, and the power to the substrate was varied from 0 to 50 W. The target and substrate bias voltages were monitored and used to estimate the division of power between the target and the substrate. [118] For all depositions, the rf impedance could be tuned using a matching network so that the reflected power was typically less than 3 W.

The targets used were 12.7 cm in diameter and spaced 5.8 cm away from the 15.5 cm diameter (water-cooled) substrate holder. The argon pressure during deposition was maintained at 8.0 mTorr with a flow rate of 60 sccm of high purity gas. The system base pressure prior to introducing argon was 1×10^{-6} Torr.

Using these conditions, tungsten films 600–800 nm thick were deposited onto patterned silicon dioxide trenches and vias on a silicon wafer. An intermediate titanium layer approximately 20 nm thick was first deposited to promote adhesion of the tungsten onto the oxide. Both the targets and the substrate were sputter cleaned for

2 minutes at 100 W prior to deposition to remove any surface contamination. The nominal tungsten deposition rate was 18.3 nm/min.

After deposition, the samples were cleaved and coated with gold for cross-sectional analysis with a scanning electron microscope (SEM). Unfortunately, adhesion of the tungsten films at low and moderate bias levels was poor, and many of the samples delaminated during this step. However, zero and high bias level samples were successfully examined using the SEM. Film thicknesses were measured by profiling a step in the film (made using a shadow mask) using a Sloan Dektak II profilometer.

Substrate bias	Target bias	Forward power	Target power	Rate (nm/min)
0 V	-1.90 kV	200 W	200 W	18.7±0.9
-102	-1.78	208	197	14.5±1.5
-190	-1.54	215	192	12.3±0.8
-247	-1.47	231	198	10.9±0.5
-338	-1.58	238	196	8.5±0.5

Table 4.3: Deposition conditions for individual tungsten bias sputtering runs. Total film thicknesses were 600–800 nm.

Table 4.3 shows the bias voltages, powers, and deposition rates of the tungsten depositions. Figure 4.35 shows the dependence of the observed net deposition rate on substrate bias. The linear dependence is consistent with the results of others. [104] Since the target power is constant, it is assumed that the rate of sputtering of the target is constant and, hence, the flux of tungsten arriving at the substrate is constant. Therefore, the drop in deposition rate shown in Figure 4.35 must be due to ion etching of the film. The dependence of this ion etch rate (IER) on the substrate bias (V_b) can be described by:

$$IER = (0.0290 \pm 0.002 \frac{\text{nm}}{\text{min-V}}) V_b \quad (4.20)$$

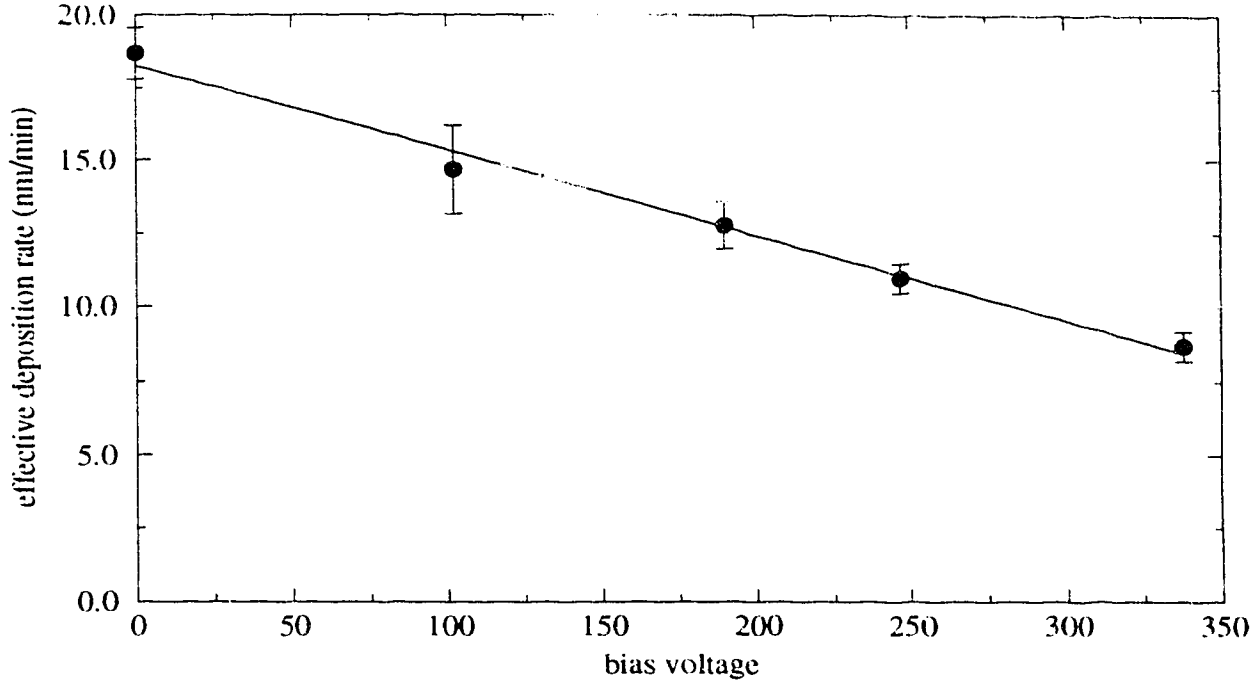


Figure 4.35: Dependence of deposition rate (normalized to 200 W target power) on substrate bias voltage.

Figure 4.36 shows the variation in the simulated relative deposition rate with the ratio of ion disc flux (Γ_i) to film disc flux (Γ_f). This also shows a linear dependence for deposition rate due to increased ion etching. The simulated ion etch rate (SER) can then be given by:

$$SER = (0.402 \pm 0.007)\Gamma_i/\Gamma_f \quad (4.21)$$

In order to match the experimental and simulated results, the experimental ion etch rate can be equated with the simulated one. This gives a calibration of the simulated ion flux to the equivalent substrate bias:

$$\Gamma_i = (0.0039 \pm 0.0002 \text{ volts}^{-1})V_b \quad (4.22)$$

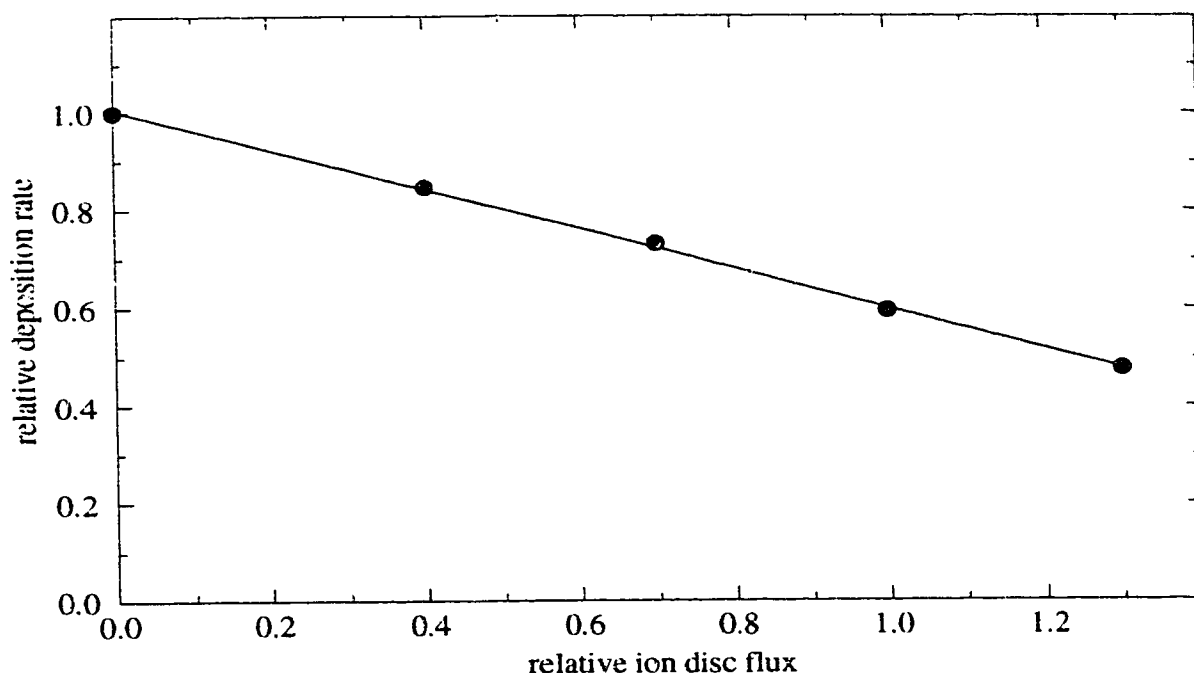


Figure 4.36: Dependence of simulated deposition rate on relative ion disc flux. This can be combined with Figure 4.35 to calibrate ion disc flux against substrate bias voltage.

Using this ion flux calibration, the reflection, resputtering, and re-emission dependencies described above, and an incident angular distribution for film discs obtained using SIMSPUD, the SIMBAD bias sputtering model is completely specified for this experimental system.

Figure 4.37 shows the experimental and SIMBAD depictions of the tungsten film deposited without an applied bias over a 0.55 aspect ratio trench. There is good agreement between the two profiles and the observed variation in column orientation over the feature is well represented in the simulated result. Figure 4.38 shows the corresponding results with an applied bias of -338 V. As can be seen by comparing with the previous figure, the relative sidewall coverage has approximately doubled

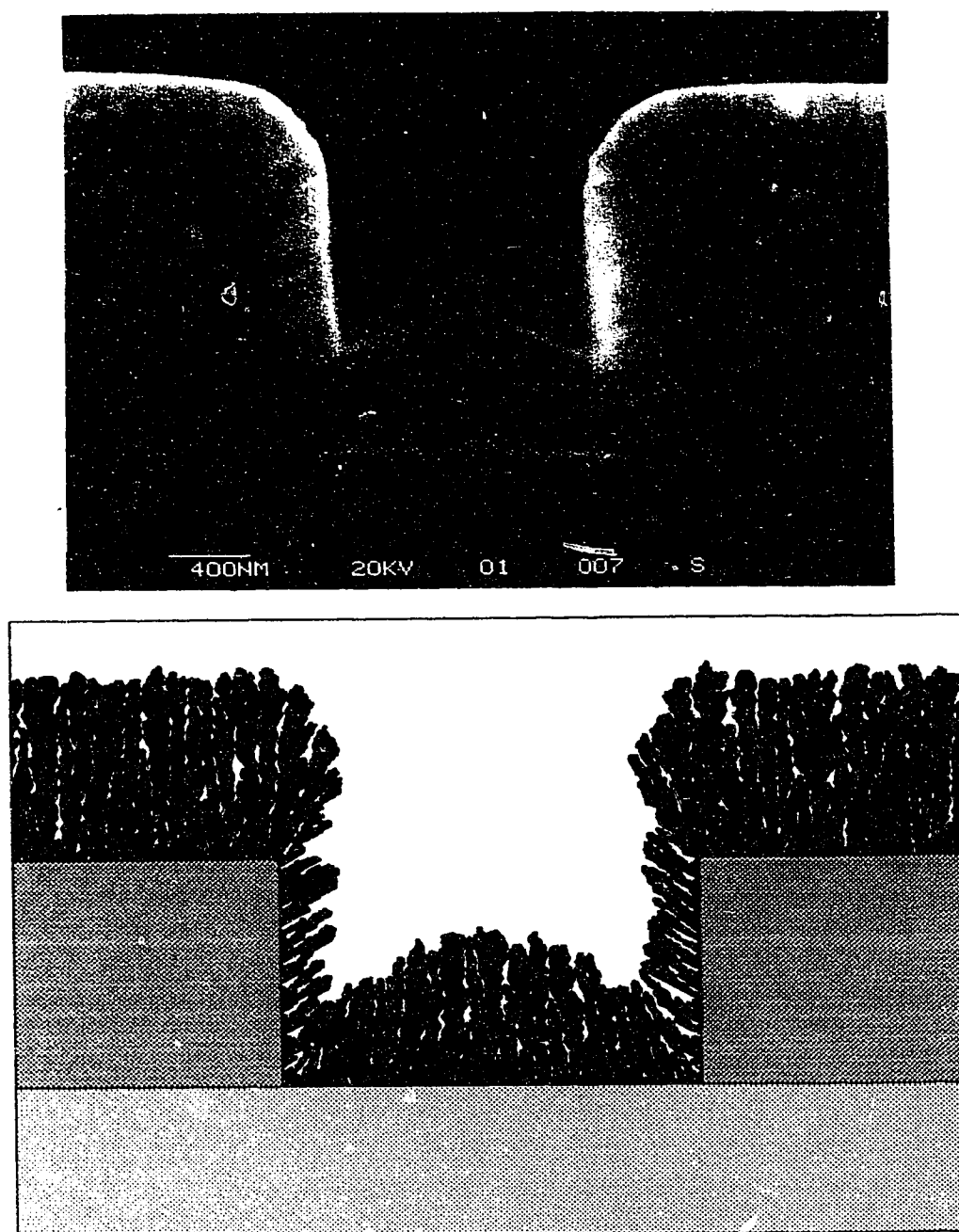


Figure 4.37: Tungsten film deposited without applied rf bias (top) and corresponding SIMBAD depiction (bottom).

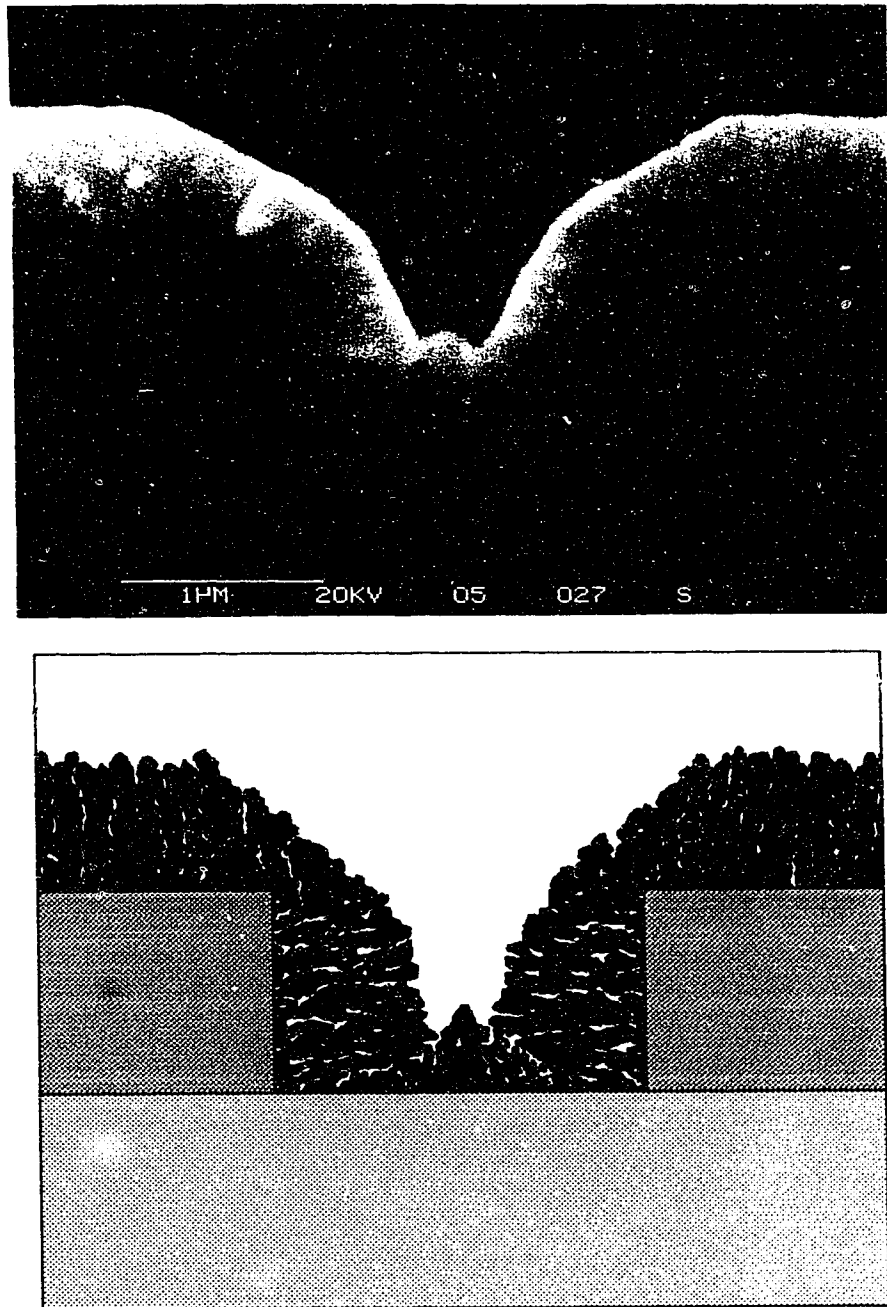


Figure 4.38: Tungsten film deposited with -338 V rf bias (top) and corresponding SIMBAD depiction (bottom).

with the application of rf bias. The surface of the biased film is more planar but with two distinct taper angles. In the bottom centre of the biased film, there is a triangle of vertically oriented columns flanked by almost horizontal ones growing from the sidewalls. All of these structural features are captured in the SIMBAD depictions.

One feature that is not present in the simulated biased film is the pair of small trenches in the silicon on either side of the central triangle. These are likely caused in the early stages of growth by ions reflecting off the central triangle and etching into the silicon. This trenching is not duplicated in the simulations as etching of the substrate is not yet modeled.

Figure 4.39 shows a thicker film deposited with a -330 V rf bias, along with a corresponding SIMBAD density plot. (This film was deposited with a slight tilt which has been included in the SIMBAD plot as a 5° offset in the film distribution.) This film shows excellent filling of the trench and relatively good overall planarity. The density plot shows the sidewall regions are almost as dense as the top ones. (This is in contrast to the film without bias which results in much lower density along the sidewalls.) In addition, it shows a small void in the centre of the trench which is also visible in the experimental film.

Figure 4.40 shows the -338 V film deposited over series of trenches with varying aspect ratios. This shows an increase in the ion etching of the silicon at the bottom of each trench as the aspect ratio increases. This is caused, in part, by the tapered sidewalls reflecting and focussing the ion flux into a progressively smaller area in the trench centre. This trend is also visible in the SIMBAD density plot of a higher aspect trench. Once again, the etching of the substrate is not supported by SIMBAD, but its

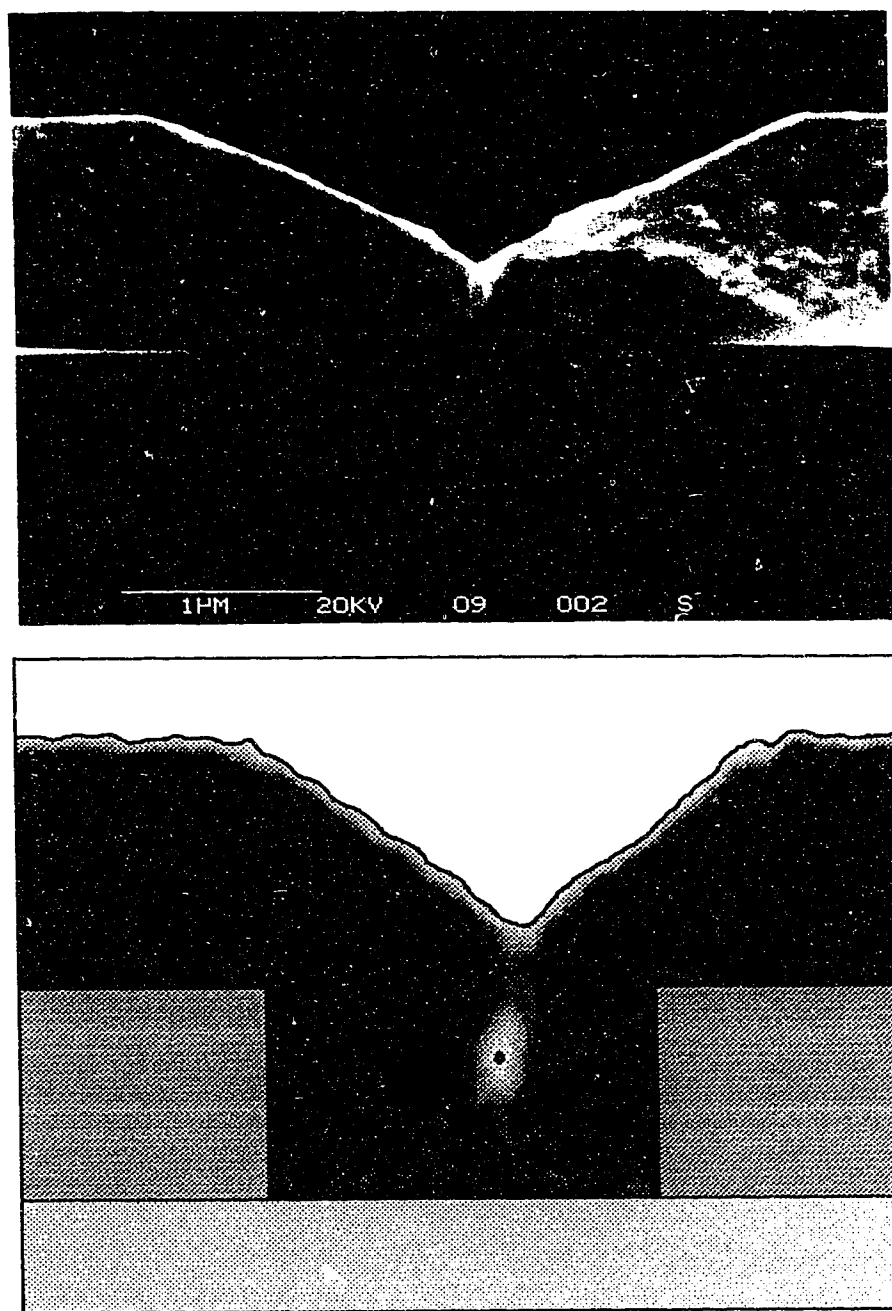


Figure 4.39: Thicker film deposited with -330 V rf bias (top) and corresponding SIMBAD density plot (bottom) averaged over 6 films.

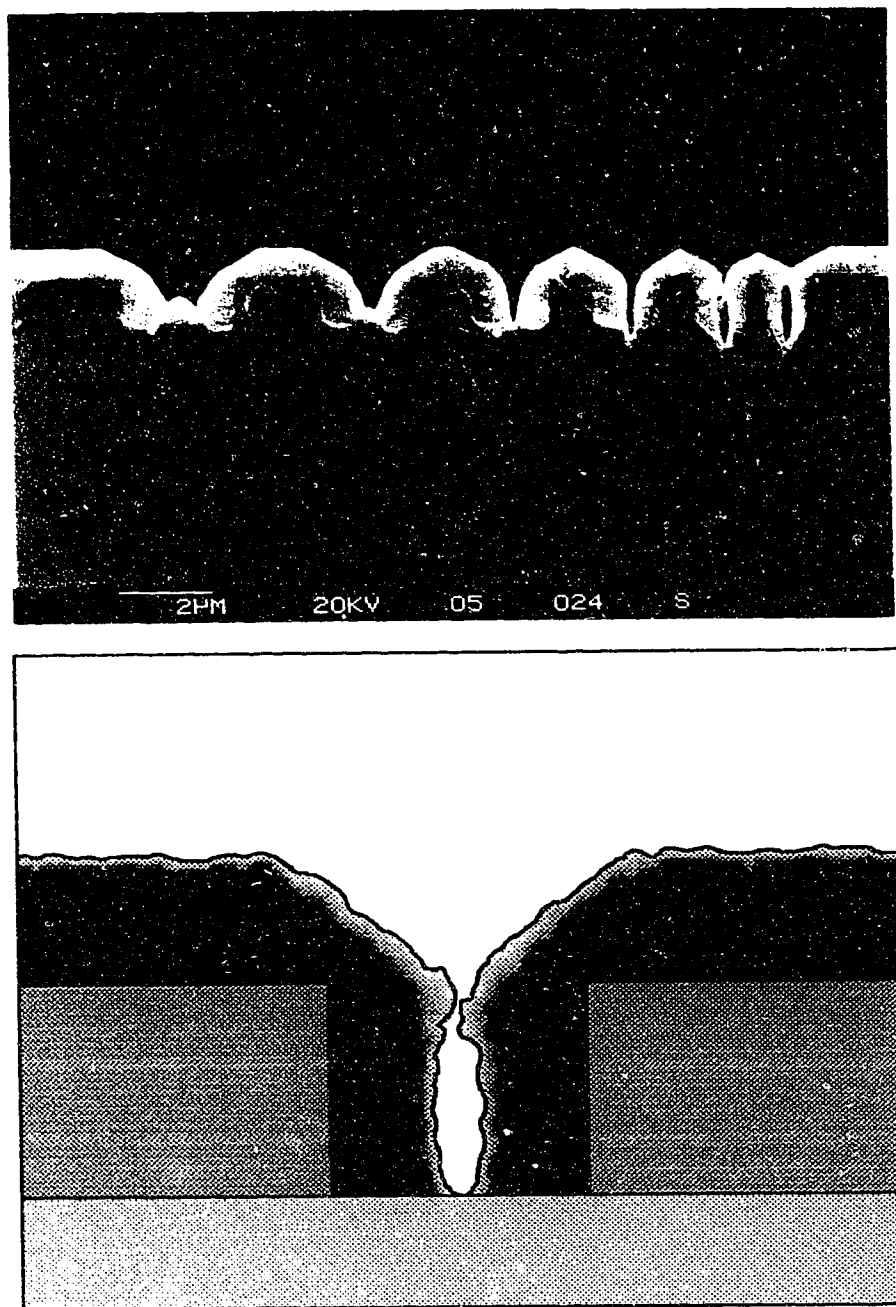


Figure 4.40: Series of trenches with varying aspect ratio (top) and a SIMBAD density plot of a narrower trench (bottom) averaged over 5 films.

likelihood is indicated by the presence of exposed substrate segments. Furthermore, the number of SIMBAD ion discs striking the bottom surface of the trench provides a measure of the amount of etching damage.

4.4 Applications of SIMBAD Bias Sputtering Model

Having verified that the SIMBAD bias sputtering model produces results consistent with experiment, it is possible to apply the model to investigate the effects of several parameters. Specifically, the effects of bias voltage, target-substrate separation, and protective layer thickness on sidewall coverage and substrate damage will be examined.

4.4.1 Effects of Bias Voltage

As indicated by Equation 4.20, a higher bias causes increased ion bombardment and, hence, an increase in film redistribution within topography. Figure 4.41 shows the predicted variation in sidewall midpoint coverage with bias voltage. (The midpoint coverage is used instead of minimum coverage because the film taper on the biased films is such that the minimum occurs at the film top corner rather than inside the feature. Since the corner coverage can be easily increased by further deposition with or without bias, it is not as critical a measurement as the sidewall coverage.) As expected, the sidewall coverage significantly improves with increasing bias, with close to a linear dependence. However, also shown in Figure 4.41 is the variation in ion damage due to increased ion flux onto the silicon at the bottom of the trench. Since this damage will impair the function of the underlying doped regions, it is desirable

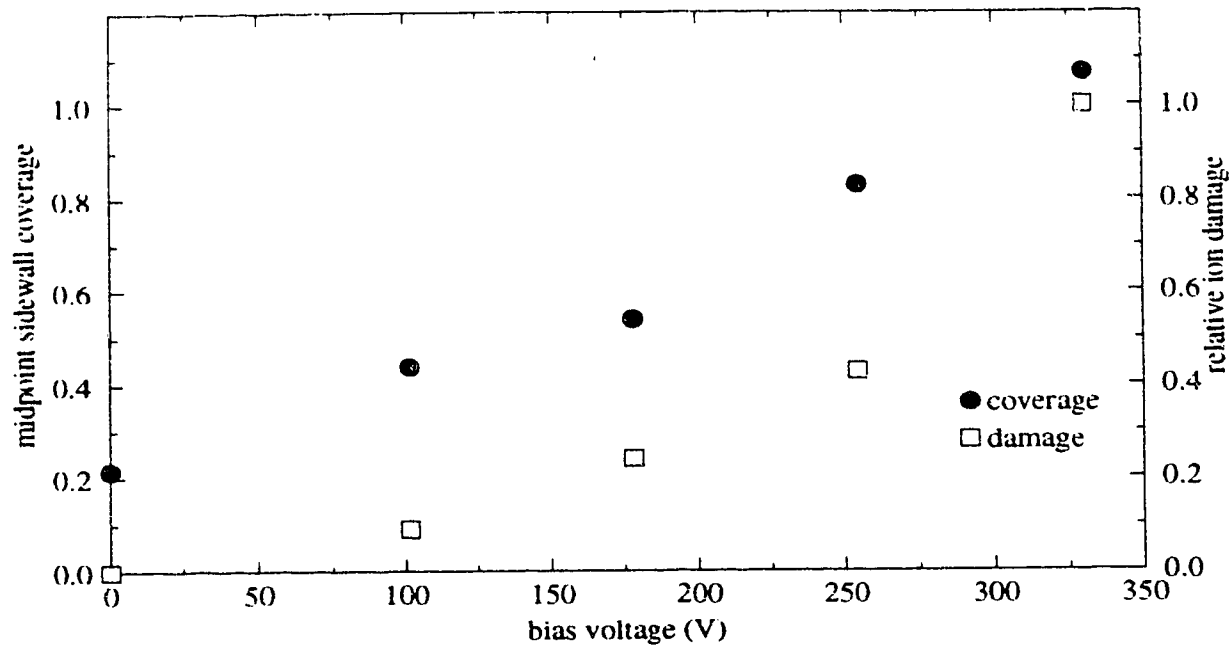


Figure 4.41: The dependence of the simulated film coverage at the sidewall midpoint on substrate bias voltage is shown for a 1.55 aspect trench (left axis). Also, the relative variation of the ion flux striking the bottom of the trench is given (right axis).

to minimize it. Clearly, under the conditions employed for these simulations, there must be a trade-off between improved coverage and increased ion damage.

4.4.2 Effects of Target-Substrate Separation

The previous chapter demonstrated the importance of the incident film flux angular distribution to determining step coverage. Since bias sputtering also changes step coverage, it is worthwhile testing the combination of bias sputtering with factors which affect angular distribution, such as target-substrate separation. Figure 4.42 shows the results of just such a study using the same topography and other conditions

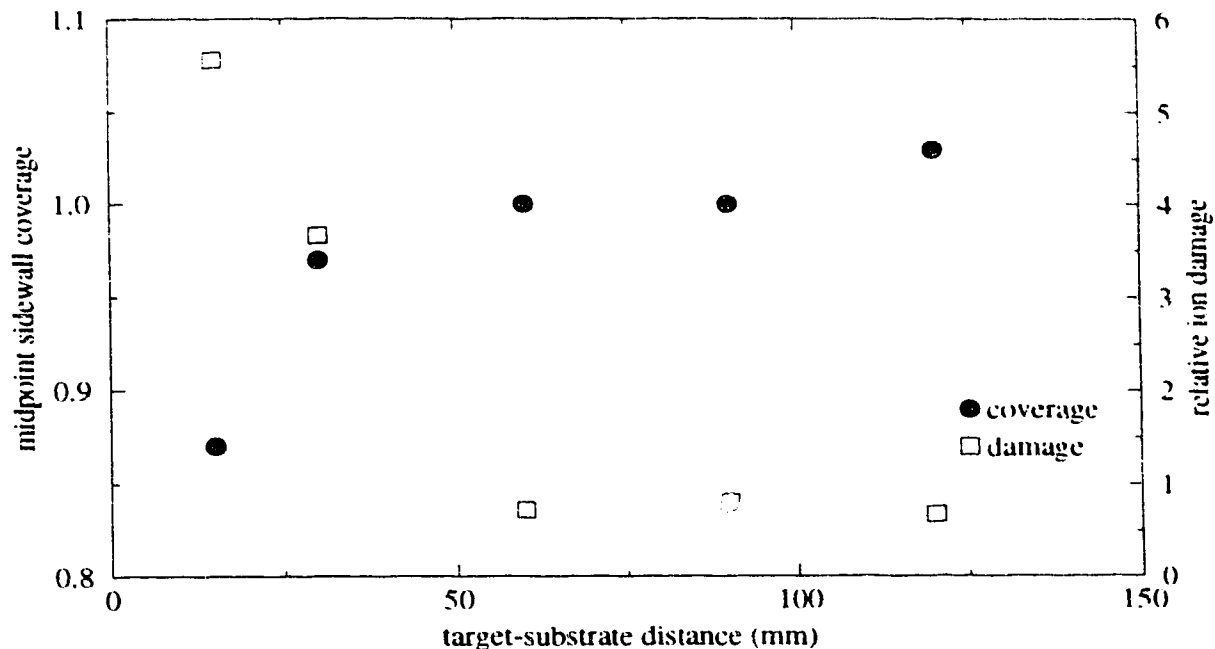


Figure 4.42: The simulated dependence of film coverage on the target-substrate separation is shown for -338 V bias conditions (left axis). Also, the variation of the ion flux striking the bottom of the trench is given (right axis). Normalization of the ion flux is the same as for Figure 4.41.

described above.

Clearly, the target-substrate spacing does have some impact on the resulting step coverage, but the ion bombardment effects appear to be dominant at this level of bias. Some improvement can be obtained at larger separations as the distribution becomes narrower and more material enters the trench — even if it does not initially deposit on the sidewall. The logical conclusion of this trend is to evaporate or sputter using a collimator [119] so that the material travels straight down into the feature with a very narrow distribution. Such an approach has been successfully employed by Bader and Lardon using alternation between evaporation and ion etching. [120]

A more serious effect of changing the target-substrate separation, however, is on the level of ion damage to the underlying silicon. At small separations, relatively few atoms reach the bottom of the trench to form a protective layer. This allows very high bombardment and resulting damage. At larger separations, this protective layer forms more readily and ion damage is significantly reduced.

4.4.3 Initial Protective Layer Use

Despite the tremendous improvement in coverage shown by Figure 4.41, bias sputtering will not be a candidate for advanced metallization situations unless it can be used for higher aspect ratio features without substantial etching damage. The results of the previous section highlight the importance of maintaining a protective film layer on the bottom surface. One possible way to accomplish this is to initially deposit a thin layer without rf power applied to the substrate in order to establish a protective coating. Then, the rf is applied for the remainder of the deposition to enhance coverage. According to SIMBAD predictions, a protective layer just 15% of the total film thickness is sufficient to completely eliminate the ion damage for the 0.55 aspect trench at -338 V bias. The penalty for this two-step process is a slight reduction of coverage from 1.07 to 0.98. (It should be remembered, however, that this reduced value is still much higher than the value of 0.22 obtained for the simulation without bias sputtering.)

Applying this approach to a higher aspect ratio (1.0) trench gives the simulation results shown in Figure 4.43. (Due to the advantages suggested by Figure 4.42, the angular distribution for these results corresponds to the 120 mm target-substrate

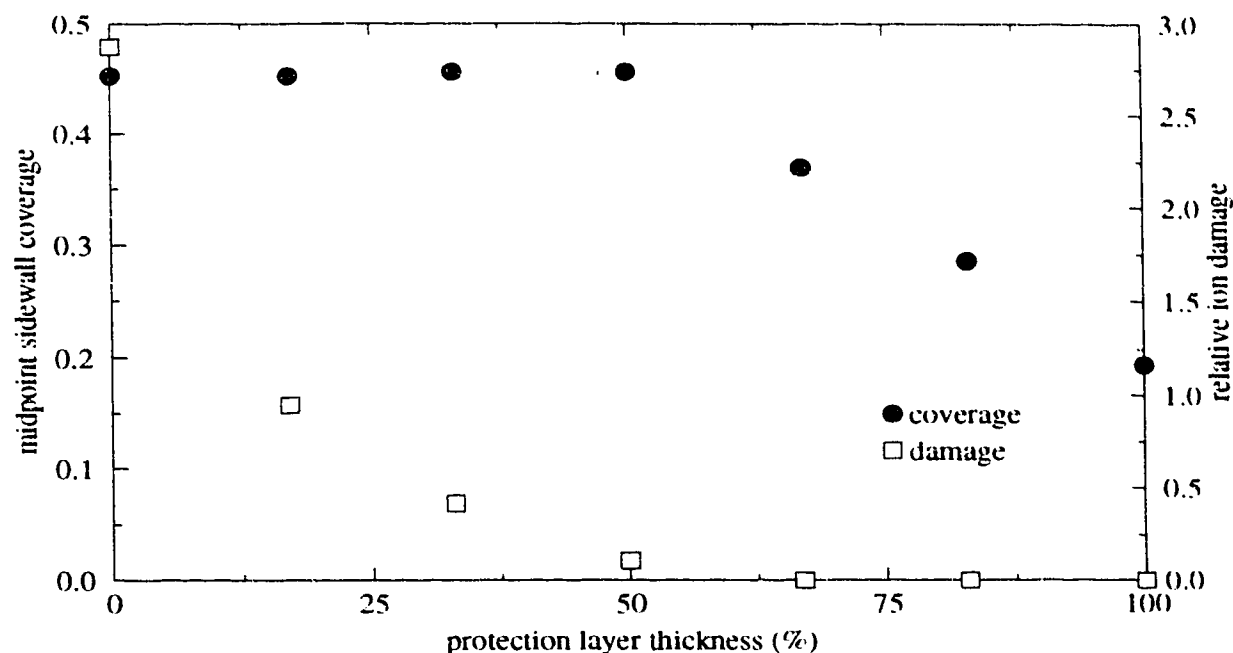


Figure 4.43: The dependence of film coverage (left axis) and ion damage (right axis) on the thickness of an initial (unbiased) protection layer for a high aspect (1.0) trench under -338 V bias conditions. Normalization of the ion flux is the same as for Figure 4.41.

separation conditions.) These data show that the ion bombardment of the trench bottom drops off very sharply with a relatively thin initial unbiased layer, but does not reach zero until the protective layer exceeds 50% of the total film thickness. However, the step coverage is virtually constant below 50% so there is no benefit to using a thinner protective layer than this anyway. The maximum step coverage that can be obtained using this two-step approach for the 1.0 aspect ratio is not as good as was seen for the 0.55 aspect feature, but it is substantially better than could be obtained without any bias sputtering at all (which corresponds to the 100% protection layer thickness case).

4.5 Summary

A SIMBAD bias sputtering model has been developed and experimentally verified using tungsten films deposited over topography. Both the model and experimental results show improvements in film coverage and planarity with this technique and adequate coverage can be obtained for aspect ratios near 1. However, a drawback of this approach is ion damage to the substrate. Although this damage can be minimized with the appropriate process design, it becomes increasingly severe as the aspect ratio increases. This may ultimately limit bias sputtering as an advanced metallization process.

Chapter 5

High Temperature Deposition¹

5.1 Introduction

Another approach to advanced metallization which has been receiving a great deal of interest recently is high temperature aluminum sputtering. [121–128] In this process, aluminum alloys are deposited under very clean conditions at temperatures close to their melting points. The resulting films appear to flow into concave topography (such as a via or trench) and partially or completely fill it. This almost completely eliminates problems with step coverage and irregular surface topography. An additional advantage of the high temperature is that it tends to produce larger aluminum grains which reduce electromigration. Clearly, this conceptually very simple process has significant potential to reduce important metallization problems.

Despite its apparent simplicity, however, high temperature aluminum has not been previously exploited because it is very sensitive to residual gas contamination [122, 123] and, therefore, requires ultra-high vacuum (UHV) sputter systems which have much lower ultimate pressures than do conventional systems. Also, there is a serious problem with the reactive nature of aluminum at these temperatures, so extra process steps are required to deposit (and pattern) barrier layers such as TiN or Ti-W alloys

¹The material in this chapter has been published as references [74, 75].

between the aluminum and most of the other materials in the integrated circuit. [123,128]

Because of these difficulties, the application of high temperature aluminum metalization is still in its infancy and could benefit from a microstructure-level model, such as SIMBAD, to help identify key process parameters and limitations and to help optimize this technique.

5.2 SIMBAD High Temperature Model

The primary benefit of depositing at high temperatures is a dramatic increase in surface diffusion. This occurs because the diffusivity (D) is thermally activated so that: [125]

$$D = D_0 e^{-Q_s/kT} \quad (5.23)$$

where D_0 is the intrinsic diffusivity and Q_s is the activation energy for surface diffusion. From empirical studies of metals at temperatures below their melting points (T_m), this energy can be approximately described by [129] (although there is considerable experimental scatter)

$$Q_s \approx 5kT_m \quad (5.24)$$

The average surface diffusion length (L) is related to the diffusivity by [125,32]

$$L = \sqrt{D\tau} \quad (5.25)$$

where τ is the mean lifetime for mobile surface atoms. This lifetime is limited by the deposition rate [127] (which determines the time it takes to form a monolayer over the atom and effectively bury it) and by the presence of reactive gas species or

defects which can bind with the atom and fix its position [125] (which is why very clean vacuum systems are required). Combining these relations gives

$$L = \sqrt{D_0 \tau} e^{-2.5T_m/T} \quad (5.26)$$

Unfortunately, since τ is dependent on system and process parameters, the prefactor, $\sqrt{D_0 \tau}$, must be calibrated for each system before this relation can be used in SIMBAD to compute high temperature diffusion lengths.

As noted in Chapter 2, the basic SIMBAD diffusion model cannot handle long diffusion lengths. However, in order to fill topography by surface diffusion, it follows that the diffusion lengths must be of the same order as the size of the topography. This is beyond the range of the existing algorithm; therefore, a new longer-range SIMBAD diffusion model is required. This is discussed next.

5.2.1 Capillarity

While the high temperature process does occur at temperatures approaching the melting point of aluminum, the film does not actually flow in the sense of a liquid. However, as with liquid flow, it is a surface tension effect that drives the film surface atoms to diffuse into areas with high (concave) curvature and, hence, fill topography. These capillarity forces arise because surface curvature (κ) modifies the surface chemical potential (μ) according to [130]

$$\mu = \mu_0 + \gamma V \kappa \quad (5.27)$$

where μ_0 is the potential of a flat film, γ is the surface tension (surface energy) of aluminum, and V is the atomic volume. The sign of κ is chosen such that diffusion from convex to concave regions lowers the overall energy.

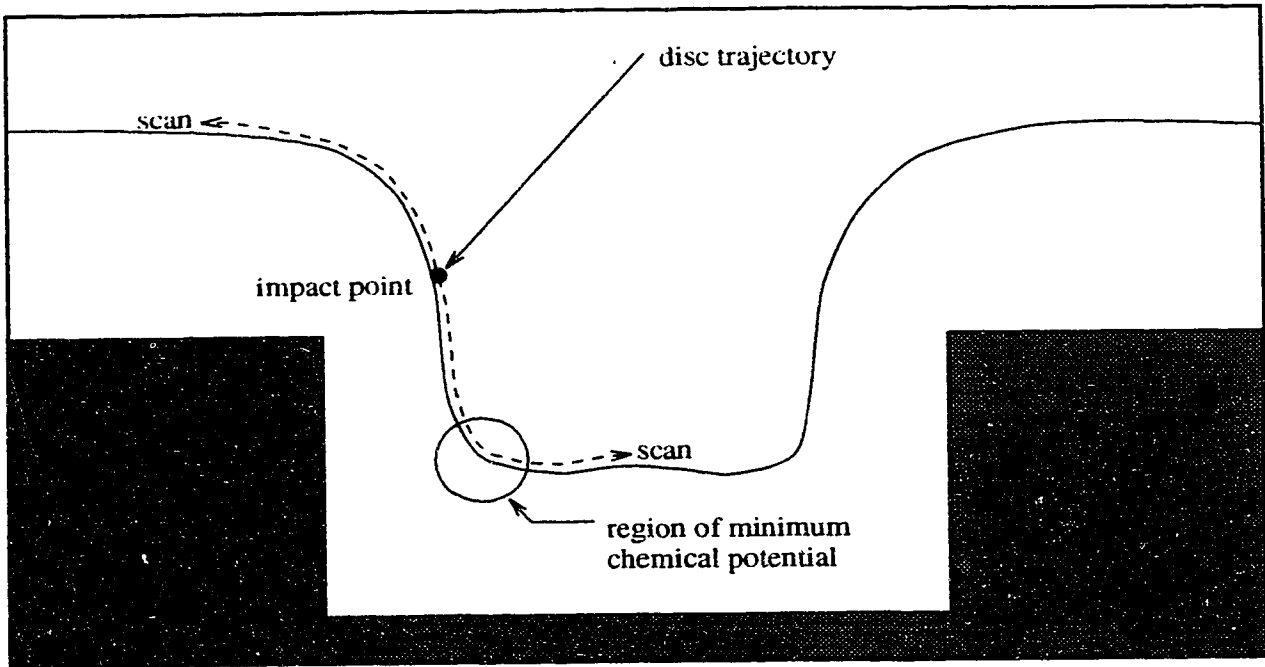


Figure 5.44: The first stage of the modified SIMBAD diffusion algorithm searches either side of the impact point for regions of low chemical potential. The second stage does a local basic SIMBAD relaxation within that region.

With the long diffusion lengths which occur at high temperatures, there can be a considerable variation in surface curvature which must be accounted for. In SIMBAD, the chemical potential can be approximated for every surface disc using the definition of curvature: [131]

$$\kappa \equiv \frac{d\psi}{d\ell} \approx \frac{\Delta\psi}{\Delta\ell} \quad (5.28)$$

where ψ is the local surface normal and ℓ is the surface path length. $\Delta\psi$ is the difference in surface normals on either side of the disc in question and can be readily computed using the surface normal calculation described in Chapter 4. $\Delta\ell$ is then equal to the twice the disc diameter. In the modified SIMBAD diffusion algorithm, the surface on either side of the impact point can be scanned up to the maximum

diffusion length to search for the region of lowest chemical potential. (See Figure 5.44.) Unfortunately, since the calculation of the surface normal used to find $\Delta\mu$ involves averaging the surface over a certain region (see page 71), the exact site with the lowest chemical potential cannot be adequately localized within this averaged region. Therefore, the final selection of the site at which to add the new disc within this region of optimal chemical potential is performed using the basic SIMBAD diffusion algorithm described in Chapter 2.

Unfortunately, Equation 5.27 is complicated by the presence of interfaces such as grain or column boundaries or the substrate. Discontinuities in the chemical potential at these points lead to effects such as grain boundary grooving and substrate wetting, respectively. In order to qualitatively account for these features, grain boundary or interface energy terms can be added to the chemical potential of discs which occur along grain boundaries or substrate interfaces. A more sophisticated SIMBAD model that more carefully accounts for these interfacial effects is currently under development in collaboration with Dr. T. Smy.

5.2.2 Assumptions

A number of assumptions are implicit in this new diffusion model. For example, the effects of bulk diffusion are assumed to be negligible. This is reasonable since the activation energy for bulk diffusion of aluminum (1.48 eV) [132] is much higher than that for surface diffusion (0.4 eV). [129] As well, grain boundary diffusion is not yet included. This is less justifiable since it involves an intermediate activation energy, [78] but, to a first approximation, the primary result of grain boundary diffusion

would be slight grain boundary grooving. [134] Also, anisotropic effects have been ignored in Equation 5.27. This omission prevents the modelling of crystal faceting, for example. [78,133] Modification of the film through re-evaporation of the film has not been included, either. [134] However, even at high deposition temperatures, the vapour pressure of aluminum is so low that the re-evaporation rate is usually several orders of magnitude less than the typical deposition rate. [135]

An important assumption of the current algorithm has been the simplification of nucleation and wetting effects. The degree to which aluminum will wet the substrate depends on the corresponding interfacial energies (tensions). [33] If the aluminum does not wet the underlying material very well, large discontinuous islands will form which are not desirable for metallization. [123,128] If there is good wetting, a continuous aluminum film can form even over severe topography. [128] To simplify nucleation behaviour, SIMBAD assumes that the underlayer is a thin film of aluminum deposited at low temperature so that the substrate surface tension is the same as that for the high temperature aluminum film. Fortunately, this assumption is consistent with common experimental practice. [123]

Because of the overhead involved in computing surface potentials for every disc, the high temperature SIMBAD model takes longer to execute than the basic model. Depending on temperature, execution times may be up to 2 hours.

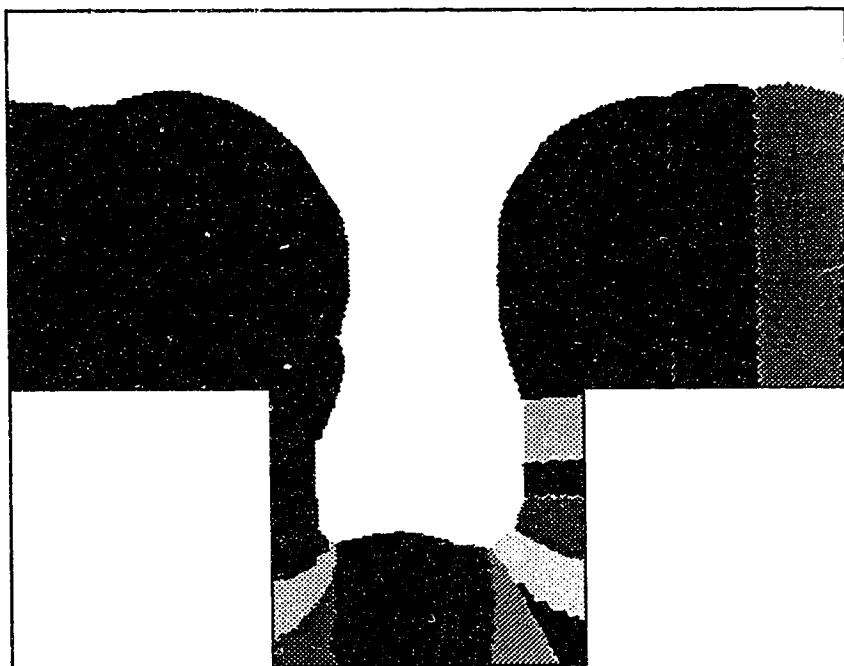
5.3 Model Verification

Figure 5.45 shows the qualitative trend of increasing diffusion lengths as substrate temperature is increased. Figure 5.45a shows the low temperature Zone 1 structure

(a) $L=27\text{ nm}$
 $T=85^\circ\text{C}$



(b) $L=200\text{ nm}$
 $T=245^\circ\text{C}$



(figure continued ...)

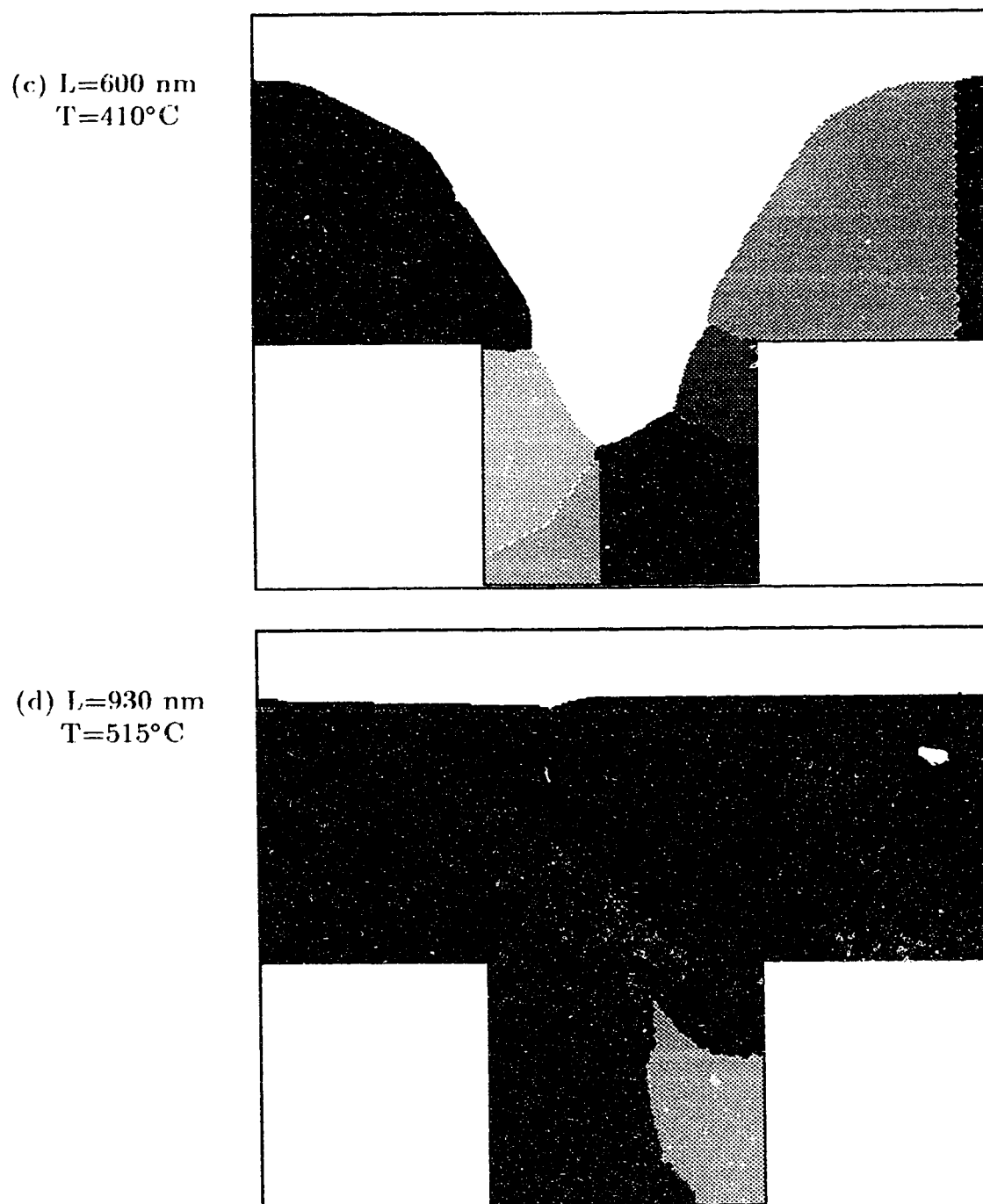


Figure 5.45: The effect of temperature on SIMBAD film structure and coverage in a $1\text{ }\mu\text{m} \times 1\text{ }\mu\text{m}$ feature. Shading is intended to highlight the column/grain structure.

that results from aluminum deposition onto cooled substrates. Figure 5.45b shows the transition to a Zone 2 structure with a keyhole-shaped profile and re-entrant sidewalls. This profile is typical of metallization films deposited without temperature control. (The estimated deposition temperature under such conditions is about 250°C.) At higher temperatures, the profile progresses to a “V”-shaped trough (Figure 5.45c) and finally becomes almost completely planar (Figure 5.45d). This sequence of profile and structure development is in very good qualitative agreement with observed experimental trends. [125,121,127]

In order to translate the diffusion lengths of Figure 5.45 into temperatures, the prefactor, $\sqrt{D_0\tau}$, must first be calibrated. The correspondence between the profile of Figure 5.45b and the films deposited by Inoue *et al.* [121] at 245°C suggests that this temperature is appropriate for this simulation. Scaling this assumption to the other three simulations gives temperatures of 85°C, 410°C, and 515°C.

A more quantitative verification of the SIMBAD model can be made by comparing the temperature dependence of the fill factor. (This is the ratio of the thickness of the film at the bottom of the feature to the sum of the feature depth and the film thickness. This ratio provides a measure of film planarity as a completely planar film would have a fill factor of 1.0.) Figure 5.46 shows this dependence for SIMBAD and for experimental results of Aronson *et al.* [125] and demonstrates good agreement given the uncertainties in the experimental conditions such as deposition rate, reactive gas pressure, and incident flux angular distribution. The discrepancy at lower temperatures, particularly, can be attributed to this last factor. Also, the uncertainty in the value of the activation energy must be considered when comparing these results.

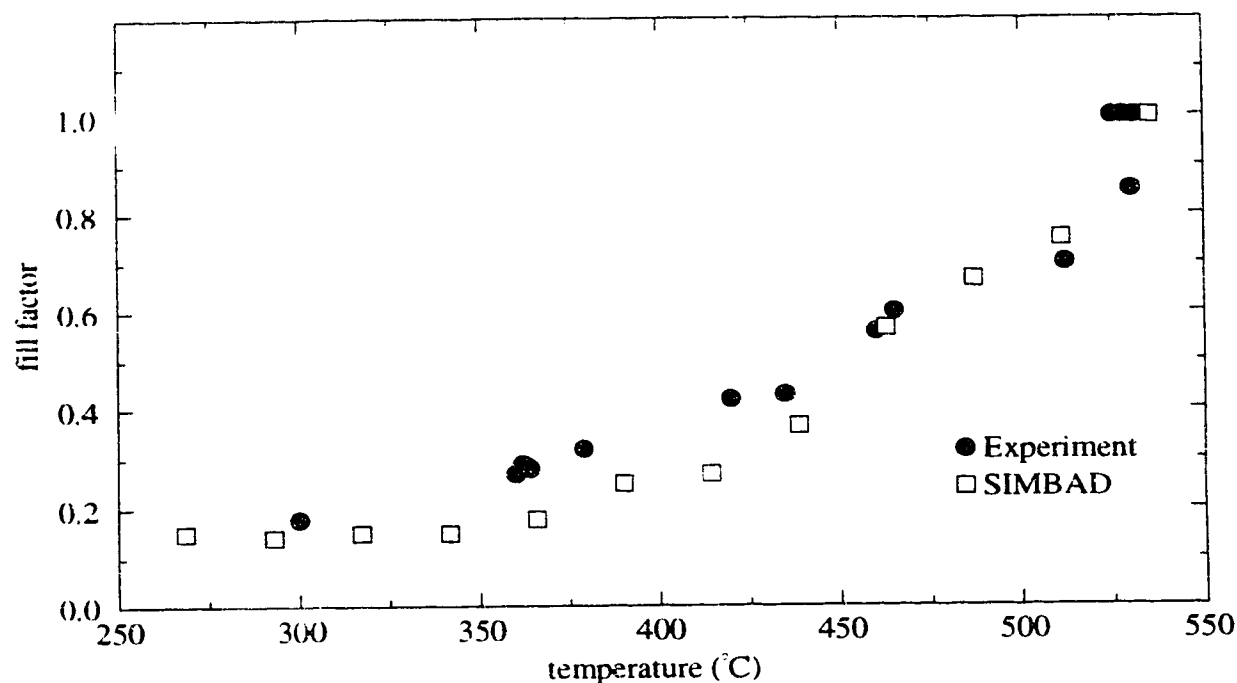


Figure 5.46: The effect of substrate temperature on fill factor for 1:1 aspect ratio features 1 μm deep. Both SIMBAD and experimental results [125] are shown.

5.4 Applications of SIMBAD High Temperature Model

Some of the obvious applications of this model have been presented in the previous section. Once calibrated, it can be used to examine the effects of temperature on film profile and microstructure. Other obvious applications are to investigate the impact of temperature on step coverage or the effects of topography aspect ratio. In addition, an intriguing prospect is to incorporate the SIMBAD high temperature model with the bias sputtering model and examine the effects of combining these two techniques.

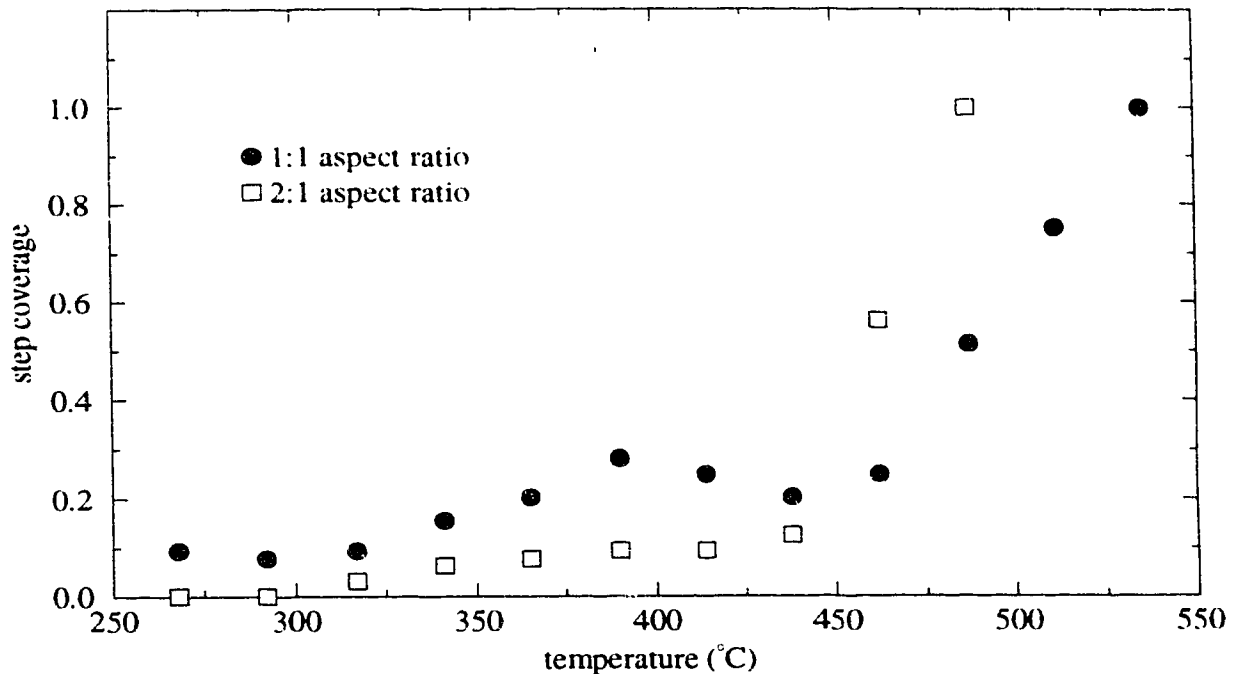


Figure 5.47: The effect of substrate temperature on step coverage for 1:1 and 2:1 aspect ratio features.

5.4.1 Temperature and Step Coverage

Figure 5.47 shows the predicted variation in step coverage with temperature for two different aspect ratios in a $1\text{ }\mu\text{m}$ deep trench. For the 1:1 aspect ratio, the coverage initially increases up to almost 400°C as material migrates into the bottom corners where curvature is high and the film is thinnest. Just below 400°C , however, the coverage starts to decrease as the profile changes from the keyhole shape to a “V” shape. The position of the minimum thickness which defines the step coverage shifts from near the bottom of the sidewall to the top corner. This corner is a region of convex curvature so the increased diffusion with higher temperature tends to remove material from this critical area and reduce coverage. This trend continues until almost

150°C when the diffusion length becomes long enough that material from the top surface can fill the concave bottom of the trough and start to planarize the film.

The trend in step coverage for the 2:1 aspect ratio trench is similar, but the magnitude of the improvement below 425°C is small as very little material enters the feature directly from the vapour and surface diffusion lengths are too short for material from the top surface to reach the critical area near the bottom. Above 425°C, however, diffusion lengths become sufficiently long, and the higher average curvature inside the 2:1 aspect ratio feature drives the film to full planarity at a lower temperature than would have occurred for the 1:1 aspect ratio.

5.4.2 Effect of Aspect Ratio

Figure 5.48 investigates the effect of aspect ratio more closely at low (245°C) and high (440°C) temperatures. (Only density plot surface contours are shown due to the small size of the plots.) As discussed earlier, the step coverage (and fill factor) at low temperature is drastically reduced with increasing aspect ratio, and the coating is discontinuous by a 2:1 aspect ratio. (However, as seen in Chapter 3, step coverage at this temperature is highly sensitive to the incident flux angular distribution.)

At higher temperature, coverage (and fill factor) are improved for all aspect ratios, but not uniformly. The low temperature 1:2 aspect film has high curvature in the critical areas near the bottom corners. Because of this curvature, these areas are rapidly filled at higher temperatures which dramatically improves coverage. The 1:1 aspect film is less markedly improved at 440°C as the convex regions which supply material are too far from the concave ones for significant diffusion between them to

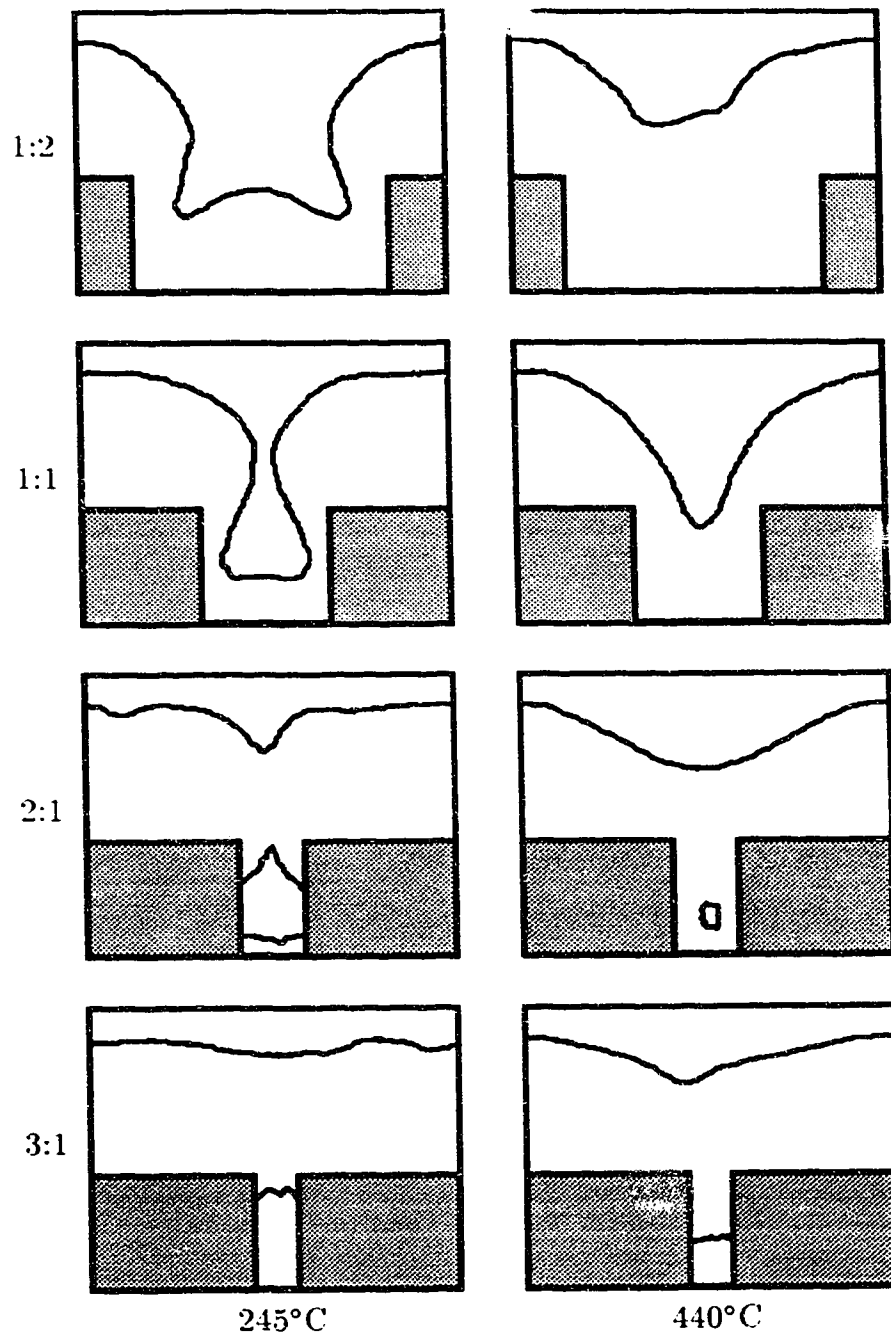


Figure 5.48: A sequence of surface contours showing the effects of substrate aspect ratio at 245°C (left) and 440°C (right).

occur. Possibly because very little additional material is needed, the 2:1 feature is substantially improved at 440°C, although a small void remains. Filling of the 3:1 film is improved at 440°C, but as also observed experimentally, [127] the film still does not make contact with the bottom. (For that to occur, even longer diffusion lengths (higher temperatures) would be required.) These trends in film profile as a function of aspect ratio agree well with experimental findings. [121,127]

5.4.3 High Temperature Bias Sputtering

One variation on the high temperature process is to combine it with bias sputtering. [125] As seen in the previous chapter, the ion bombardment modifies the surface both through resputtering and ion-induced diffusion. Since these effects are not temperature sensitive, they can complement the effects of high temperature diffusion and possibly reduce the temperatures required for improved coverage.

The simulated effect of this combination can be seen in Figure 5.49, which presents a matrix of surface plots with temperatures ranging from 245°C to 535°C and relative ion fluxes varying from 0 to 1. As desired, the primary effect of the rf bias is to lower the temperature at which planarization occurs. (Alternatively, at any given temperature, the ion bombardment improves the step coverage.) This is attractive since lower temperatures reduce problems with chemical interaction between the aluminum and other materials. These results are consistent with what has been observed experimentally. [125]

One problem that can be seen in the simulated biased films, however, is the tendency to create a central void which would increase resistivity and electromigration. As

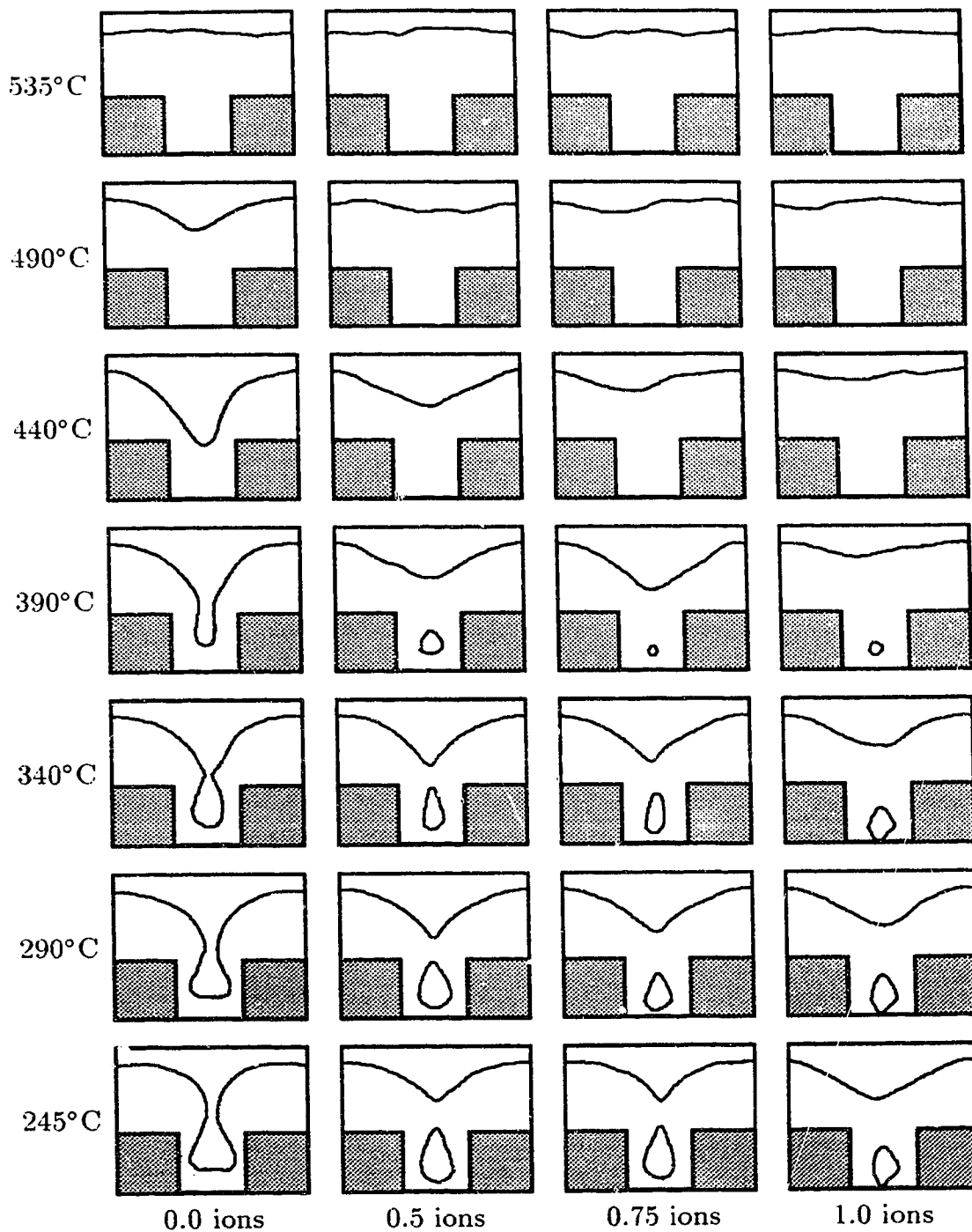


Figure 5.49: A matrix of surface contours showing the effects of both substrate temperature and substrate bias. Temperature increases vertically, and ion bombardment increases to the right.

seen earlier, another problem is that ion bombardment of the substrate can cause damage to the underlying material. This is particularly important since ion etching of the barrier layer could cause its failure and lead to significant chemical interaction. However, the techniques suggested in Chapter 4 to prevent this could also be employed here.

5.5 Summary

A preliminary high temperature SIMBAD model has been developed which has good qualitative agreement with reported experimental results. Application of the model indicates that very good coverage and filling can be obtained for high aspect ratio (above 1) features provided the substrate temperature is sufficiently high. The required temperature can be reduced with the inclusion of bias sputtering, although higher ion fluxes may introduce voids and cause ion damage to the underlying material.

Chapter 6

Refractory Chemical Vapour Deposition¹

6.1 Introduction

There has recently been a great deal of interest in using chemical vapour deposition to form metallization layers. [26, 23, 136] The primary reason for this is the possibility of obtaining almost conformal coverage (unity step coverage) even over extreme topography. [23] Much of the interest so far has been in the refractory materials such as tungsten, [136–139] molybdenum, [23] WSi_x , [136, 137] and TiN [140, 141] which have desirable properties such as high process temperature tolerance, excellent electromigration resistance, and good diffusion barrier properties. [23, 142, 143] Most importantly, they have been relatively easy to deposit and can usually achieve good conformality. This has already led integrated circuit manufacturers to employ CVD tungsten in commercial products. [144] However, these refractory materials also have very pronounced columnar microstructures which can be of concern to film performance. [145, 28, 146]

Refractory metal CVD is usually performed in a single wafer reactor vessel. [136] (See Figure 6.50 for a schematic diagram.) Reactant gases (such as WF_6 and H_2 or SiH_4 for tungsten deposition) are introduced into the reactor containing heated

¹The material in this chapter has been published as references [76, 77].

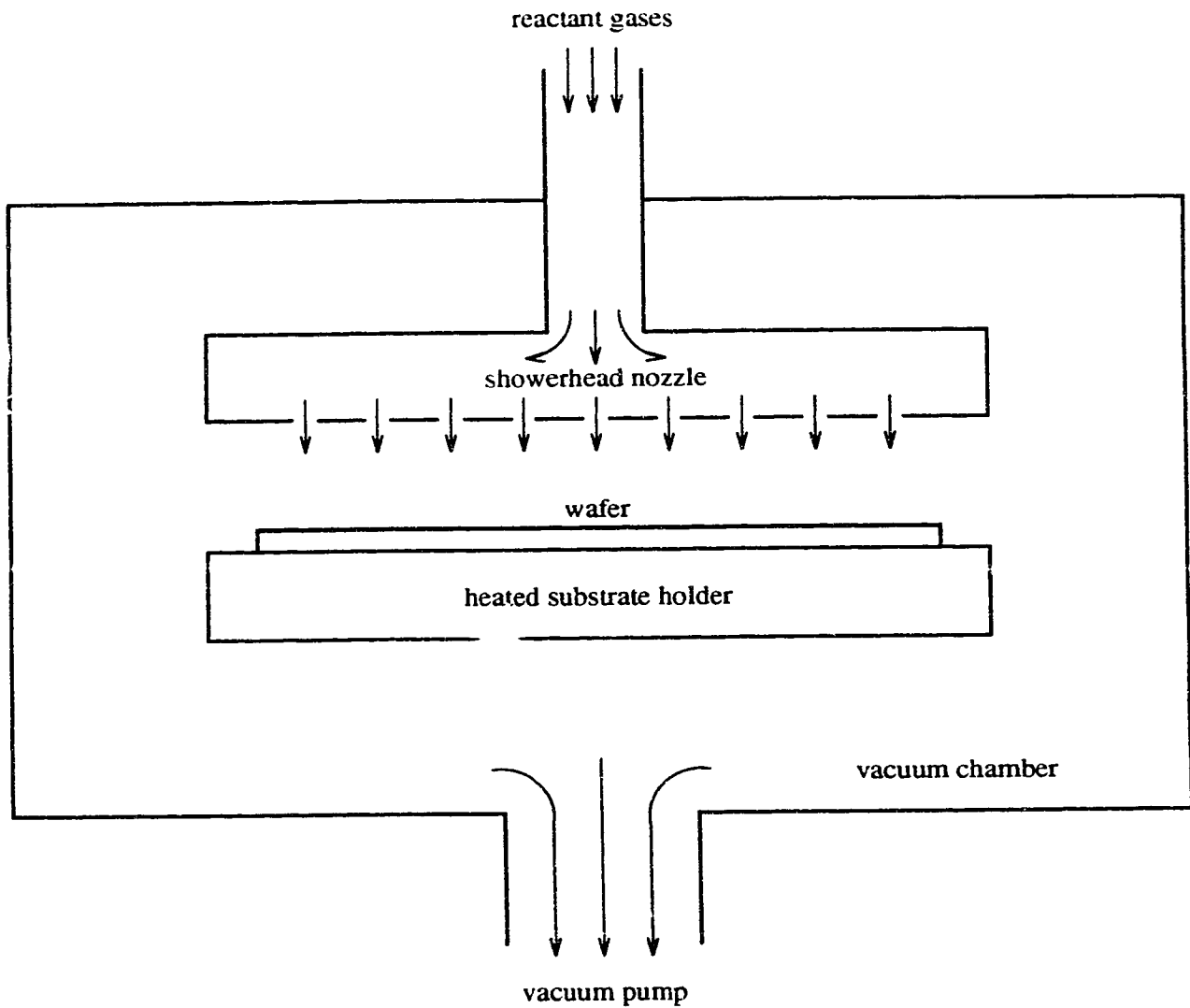


Figure 6.50: Typical single wafer CVD reactor. Reactant gases are sprayed onto the hot substrate which catalyzes the CVD reaction. Exhaust gases are pumped out to maintain low chamber pressure.

substrates (300–450° C for tungsten [136]). The high temperature activates a surface reaction which produces the metal film. (Gaseous byproducts are desorbed from the surface and pumped away.) This is usually performed at low pressures to enhance uniformity and reduce gas phase reactions which produce unwanted particles. [26] Plasma activation is also possible to reduce process temperatures, but has produced inferior metal films so far. [26]

Unfortunately, most of the refractory CVD films require extra process steps to deposit initial nucleation, adhesion, or barrier layers, in order to promote film growth and prevent chemical attack by the process gases of the underlying material. [136] (Usually a sputtered Ti-W or TiN layer is used to perform all three functions.) In addition, refractory materials such as tungsten have higher resistivities than aluminum so the refractory material is commonly used only to fill difficult vertical topography such as vias, and then aluminum alloys are used to form the longer horizontal runners. However, before the aluminum deposition, the excess tungsten must first be etched back to form via plugs. [136] (See Figure 6.51)

Because of the complexities involved in such CVD processes, it is useful to have a simulation capability to facilitate better understanding and optimization. A number of general CVD simulations have been developed, [148–155] but these have usually been string algorithm-based and cannot provide information about the film microstructure. Since the refractory materials have such a prominent columnar structure, a SIMBAD CVD model seems more attractive. For maximum generality, such a model should be simple and flexible and not optimized for a specific CVD chemistry.

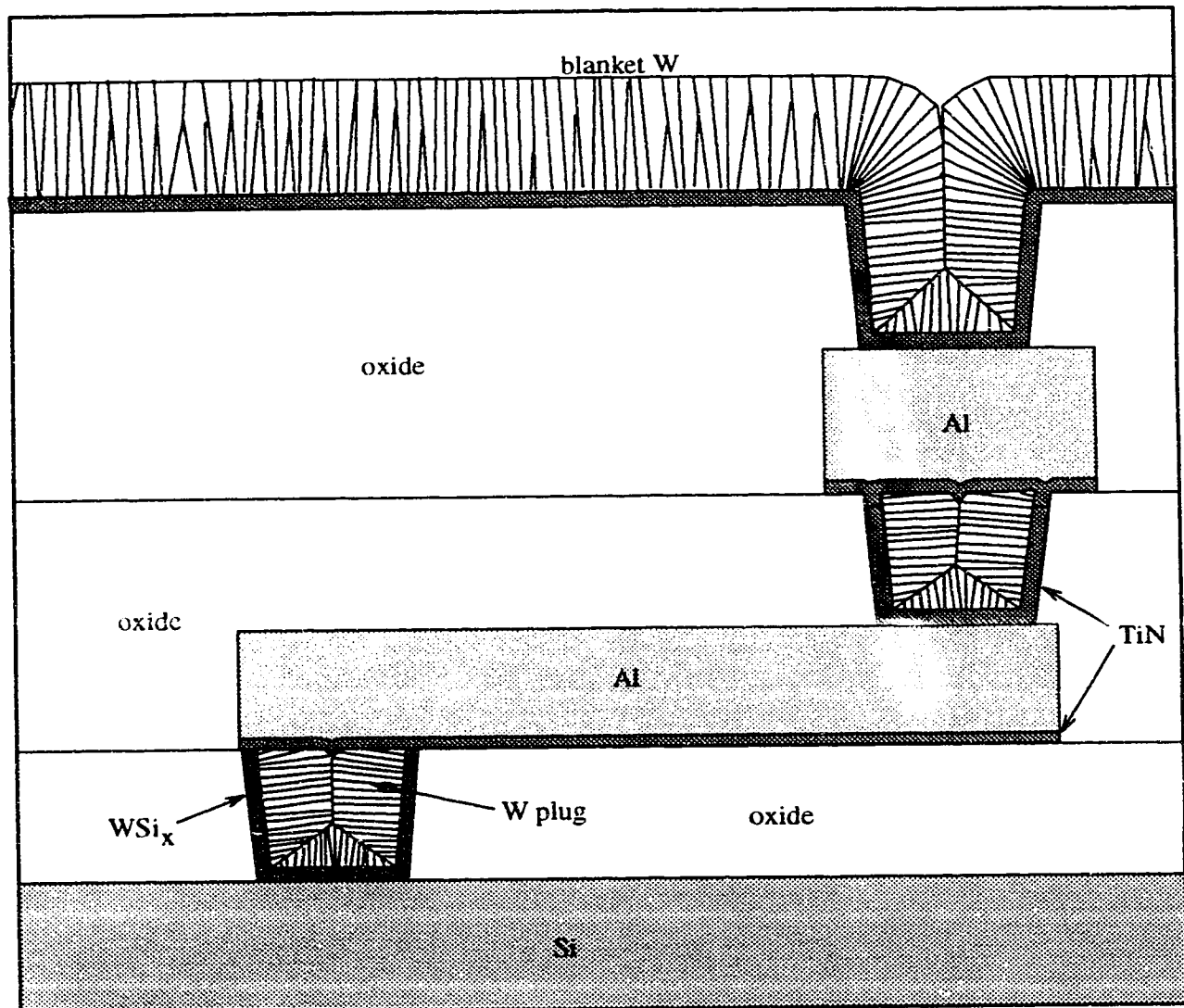


Figure 6.51: Illustration of tungsten plug technology. Blanket CVD tungsten layers are deposited over topography and then etched back to leave only the vias filled. Horizontal interconnection is then achieved with low resistivity (sputtered) aluminum. TiN barrier layers are employed in this example, and contact to the silicon is made by WSi_x. In this diagram, the top tungsten layer has not yet been etched back.

6.2 CVD Microstructure

Since CVD is a fundamentally different deposition technique than sputtering or evaporation, it is useful to re-evaluate the origin of CVD microstructure before developing a SIMBAD model. In general, CVD film growth involves the following sequence of events: [147]

1. diffusion of the reactant gases to the surface
2. adsorption onto the surface
3. surface diffusion of reactants
4. surface reaction to form film material
5. desorption of the byproduct gases
6. diffusion of the byproducts away from the surface
7. surface diffusion of the solid products

The impact of each of these events on the development of the film coverage and microstructure should be considered.

The first item, involving reactant gas diffusion, is important since it determines the incident angular distribution (discussed below) and shadowing which we have already seen are important to microstructure development. In contrast, the diffusion of byproduct gases away from the surface (Item 6) likely has little impact on film microstructure.

Items 2, 4, and 5 are all surface events which affect the reaction probability. While the CVD reaction generally involves more than one species, under typical conditions, the reaction rate is limited by the availability of just one. The others are assumed to be present on the surface in sufficient quantity for the reaction to proceed. However, the availability of this one critical precursor (reactant) is not simply limited by its impingement rate as the molecules may fail to be adsorbed (and bounce off) or may be adsorbed but subsequently desorb (evaporate) before a reaction can occur. This leads to the concept of a sticking coefficient, s , which is the probability that the critical precursor will be adsorbed long enough for the reaction to occur.

In CVD, the sticking coefficient is often considerably less than 1 because the precursors are being adsorbed onto a surface whose temperature is well above their boiling points. (This is unlike physical vapour deposition, such as sputtering, where the substrate is generally much cooler than even the melting point.) If the precursors do not stick, the desorbing molecules are re-emitted from the surface and are free to adsorb and react elsewhere on the film. However, as seen in Chapter 4, material that is re-emitted from inside vias and trenches is more likely to be trapped on another surface inside that same feature. Therefore, one expected effect of a non-unity sticking coefficient is improved step coverage.

Surface diffusion, of course, also affects microstructure development, and that by the precursors (Item 3) must be considered since they are loosely bound (as discussed above) and consequently have a low activation energy for diffusion. However, the range of this diffusion is limited by the high desorption rate and the reaction rate. The role of surface diffusion of the product species (Item 7) depends on the material being deposited. Refractory materials, such as tungsten, are deposited at low temperatures

compared with their melting points and consequently experience very little diffusion after formation. (In contrast, CVD aluminum is deposited at a substantial fraction of its melting temperature, [26] and may consequently experience considerable post-formation diffusion.)

The essential factors, therefore, that must be considered in a CVD microstructure model for refractory materials are shadowing and surface diffusion of the precursors as well as a non-unity sticking coefficient. These features can be readily implemented by a ballistic deposition model such as SIMBAD.

6.3 SIMBAD CVD Model

The SIMBAD representation is sufficiently general that its extension to CVD can be made with relatively moderate modification. In the case of SIMBAD CVD, a distinction must be made between the ballistic (moving) discs and the ones which are already aggregated into the film. The ballistic discs represent averages of the precursor species while the film discs represent the (solid) reaction product species. The transformation of the former to the latter occurs through the surface reaction.

In order to model flux shadowing, precursor discs are randomly launched from an appropriate angular distribution from just above the film surface (well within the mean free path for collisions between gas molecules). As before, these discs follow straight line trajectories until they strike an already deposited film disc or the substrate (initialized to the device topography by a series of line segments). The linear trajectories used by SIMBAD are valid provided the distances travelled are much less than the mean free path for collisions in the process gas. For films deposited within micron

and submicron features, this is a safe assumption for typical LPCVD pressures of less than 100 mTorr. However, there is increasing interest in depositing CVD tungsten at pressures up to 80 Torr [148] due to the higher deposition rates possible. [136] To accommodate these pressures, a two dimensional isotropic scattering model with a fixed mean free path has been incorporated into the SIMBAD ballistic phase.

Once the discs strike the film, they either desorb or react – with the probability dependent on the sticking coefficient. If they desorb, the discs are re-emitted from the surface according to a thermal (cosine) random angular distribution. [135] Re-emitted discs may strike the film at another point in an iterative process until either a reaction does occur or the disc returns to the source gas.

If the precursor disc reacts, it is first allowed to diffuse a limited distance over the surface using the basic SIMBAD diffusion model. (The high temperature model described in Chapter 5 is not appropriate since capillarity forces do not generally apply to adsorbed precursors. [79] They would apply for product disc diffusion, but such diffusion is virtually insignificant for refractory materials and is ignored in the SIMBAD CVD model.)

6.3.1 Sticking Coefficient

The sticking coefficient is clearly a central parameter to this model. In general, its value depends on the precursor desorption rate (R_d), the surface reaction rate (R_r), and the impingement rate (R_i) according to [60]

$$s = (1 + \frac{R_d + R_i}{R_r})^{-1} \quad (6.29)$$

Unfortunately, these rates are inter-related and may vary across the film. However, it is often appropriate to use a single averaged value. This is the approach employed by most of the CVD string algorithm profile simulations, [149-153] and is also used in SIMBAD.

The assumptions and limitations inherent in the constant sticking coefficient approximation have been explored. [60, 149, 155] Implicit to this type of model is the assumption that the reaction is limited by the supply of a single precursor species and that the reaction proceeds at a rate proportional to the supply of that precursor. (This is not always a good assumption if a non-linear reaction mechanism is involved. [155]) Of course, the value of the sticking coefficient varies with the process being modeled and is strongly dependent on the conditions being used. Allowing for multiple sticking coefficients (corresponding to several possible precursors [151]) or sticking coefficients which vary with underlying material (selective deposition) are straightforward modifications to SIMBAD.

The sticking coefficient strongly affects SIMBAD execution time. In general, there is an inverse dependence. As a result, low sticking coefficient (0.01) simulations may take several hours to execute.

6.3.2 Incident Angular Distribution

The angular distribution used by SIMBAD CVD simulations is that due to an ideal gas at thermal equilibrium impinging on a flat plane. (Since feature sizes are usually small compared with the mean free path, deviations in the angular distributions due to non-planar topography should be minor.) Intuitively, since thermal gas scattering

is isotropic, the incident CVD distribution should also be isotropic (as assumed by some groups [150, 154] using string algorithms). However, this neglects the increased probability of scattering for gas molecules impinging at angles nearly tangential to the surface (since they must travel further to reach the substrate). As well, the effects of gas depletion near the substrate due to the finite sticking coefficient must be considered. Of course, the distribution must also be projected onto two dimensions for use in a model such as SIMBAD.

The flux density striking the substrate at spherical coordinate angles (θ, γ) due to scattering events in a thin slab at a height h above the substrate can be given by

$$\begin{aligned}
 \mathcal{F}(\theta, \gamma, h) d\Omega dh &= (\text{probability of scattering to } (\theta, \gamma) \text{ within } d\Omega) \\
 &\times (\text{probability of scattering at } h \pm \frac{1}{2}dh) \\
 &\times (\text{probability of reaching substrate from } h \text{ without rescattering}) \\
 &= \left(\frac{d\Omega}{4\pi}\right) G(h)dh (e^{-\lambda/\lambda_m})
 \end{aligned} \tag{6.30}$$

where λ is the distance that must be travelled from h at angle (θ, γ) to reach the substrate ($\lambda = h/\cos \theta$), and λ_m is the mean free path for scattering (which is assumed to be approximately constant). The first term simply describes the isotropic scattering of a thermalized gas. The second term contains the scattering density, $G(h)$, which varies with h due to the removal of the precursor gas by the CVD reaction. If it is assumed the change in partial pressure of the precursor within a few λ_m of the surface is small compared with the total pressure, then the scattering density can be approximated by

$$G(h)dh = A p(h)dh \tag{6.31}$$

where $p(h)$ is the precursor partial pressure at height h , and A is a proportionality

constant. From Fick's Law [156], the flux diffusing to the substrate is given by

$$J = -D \frac{dn}{dh} = -\frac{D}{kT} \frac{dp}{dh} \quad (6.32)$$

where the gas diffusivity is given by $\frac{1}{3}\lambda_m(8kT/\pi m)^{1/2}$ from the kinetic theory of gases, [156] and $p = nkT$ for an ideal gas. By continuity, it is reasonable to assume J is constant (at least for several λ_m near the substrate). This flux equals the reaction rate at the surface.

$$\begin{aligned} J &= (\text{sticking coefficient}) \times (\text{impingement rate on the substrate}) \\ &= s (2\pi mkT)^{-1/2} p(0) \end{aligned} \quad (6.33)$$

where the impingement rate is also given by kinetic theory. [156] Equating (6.32) and (6.33) and solving the differential equation gives

$$p(h) = p(0) \left(1 + \frac{3sh}{4\lambda_m}\right) \quad (6.34)$$

where $p(0)$ is the pressure at the surface. Combining (6.30), (6.31), and (6.34) gives

$$\mathcal{F}(\theta, \gamma, h) d\Omega dh = \frac{Ap(0)}{4\pi} \left(1 + \frac{3sh}{4\lambda_m}\right) (e^{-h/\lambda_m \cos \theta}) d\Omega dh \quad (6.35)$$

Integrating (6.35) over h/λ_m from 0 to ∞ gives

$$\mathcal{F}(\theta, \gamma) d\Omega = C d\Omega \left(\cos \theta + \frac{3s}{4} \cos^2 \theta\right) \quad (6.36)$$

for some normalization constant, C . In order to collapse this distribution into two dimensions, the coordinates are changed to (θ_{2D}, η) where θ_{2D} is the angle from the z-axis to the projection onto the x-z plane and η is the angle perpendicular to this projection. (See Figure 6.52) In this coordinate frame,

$$d\Omega = \cos \eta d\eta d\theta_{2D} \text{ and } \cos \theta = \cos \theta_{2D} \cos \eta$$

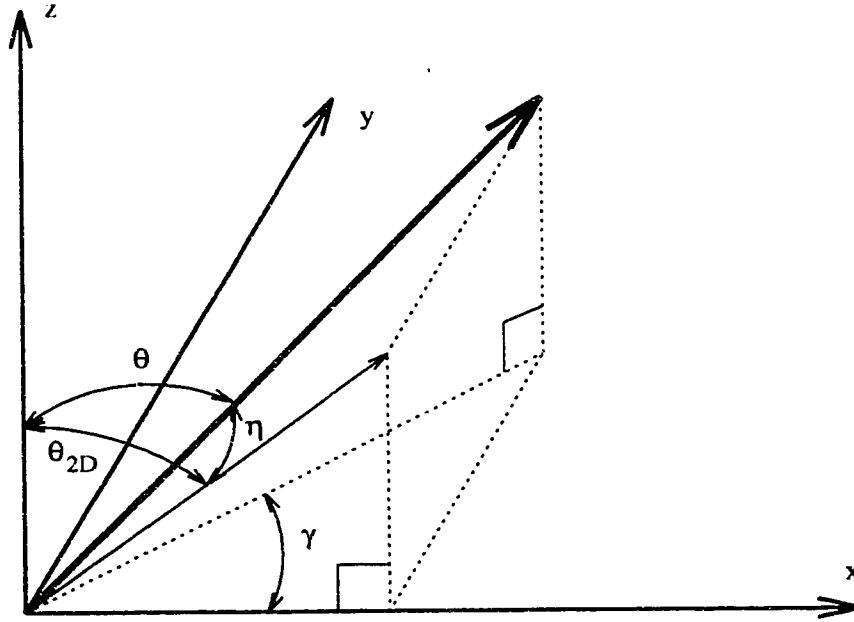


Figure 6.52: Coordinate system for projecting CVD angular distributions into two dimensions.

Therefore, (6.36) becomes

$$\mathcal{F}(\theta_{2D}, \eta) \cos \eta \, d\eta d\theta_{2D} =: C \cos \eta \, d\eta d\theta_{2D} (\cos \theta_{2D} \cos \eta + \frac{3s}{4} \cos^2 \theta_{2D} \cos^2 \eta) \quad (6.37)$$

Integrating both sides of (6.37) over η from $-\pi/2$ to $\pi/2$ gives the final distribution used by SIMBAD.

$$f_{\Theta}(\theta_{2D}) \, d\theta_{2D} = C \left(\frac{\pi}{2} \cos \theta_{2D} + s \cos^2 \theta_{2D} \right) d\theta_{2D} \quad (6.38)$$

6.4 Model Verification

Figure 6.53a shows a CVD tungsten film deposited by Hasper *et al.* [157, 136] over a trench $3 \, \mu\text{m}$ wide and $13 \, \mu\text{m}$ deep with the deposition conditions given in Table 6.4. It

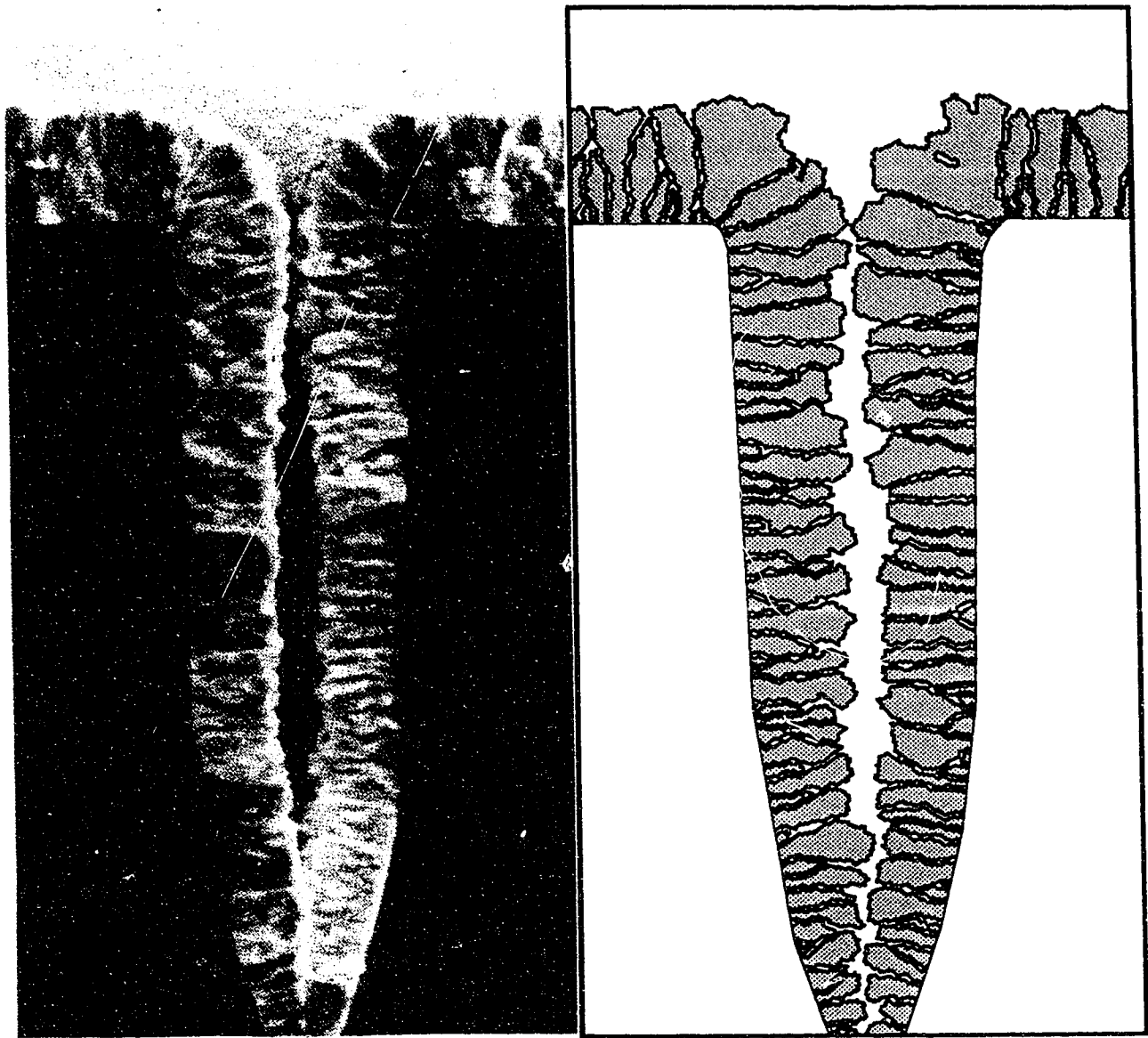


Figure 6.53: Comparison between CVD tungsten film (left) deposited by Hasper *et al.* [157, 136] and the corresponding SIMBAD depiction (right). The trench is approximately $3\text{ }\mu\text{m}$ wide and $13\text{ }\mu\text{m}$ deep. The sticking coefficient used in the simulation was 0.0089. (Photo courtesy J.E. Schmitz. [136])

clearly shows the nearly conformal coverage and characteristic columnar microstructure of CVD refractory metal films. In order to match this film with a SIMBAD depiction, it is first necessary to determine the appropriate sticking coefficient.

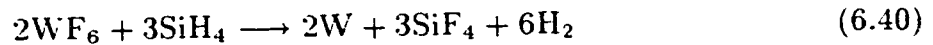
SiH ₄ partial pressure at the wafer	1.5 Pa	11.3 mTorr
WF ₆ partial pressure at the wafer	10 Pa	75 mTorr
total pressure (including argon carrier gas)	133 Pa	1 Torr
wafer temperature	673 K	400 °C
deposition rate	150 nm/min	2.5 nm/s

Table 6.4: Deposition conditions used by Hasper *et al.* [157] to deposit tungsten. Their reported partial pressures have been corrected for diffusion and depletion effects.

Hasper *et al.* determined that the rate-limiting precursor was silane (SiH₄) under these conditions. This means that the appropriate sticking coefficient is that for silane. This can be computed by comparing the film growth rate (dh/dt) with the silane impingement rate (R_i).

$$\frac{dh}{dt} = s \frac{2}{3} V R_i \quad (6.39)$$

where V is the atomic volume of tungsten ($1.58 \times 10^{-29} \text{ m}^3$ [47]). The $2/3$ factor stems from the consumption of three molecules of silane to produce two tungsten atoms according to the reaction equation [157, 26]



The impingement rate can be computed from kinetic theory: [156]

$$R_i = p_{\text{SiH}_4} (2\pi m k T)^{-1/2} \quad (6.41)$$

where $m = 32.4 \text{ AMU}$ for silane.

Using the data from Table 6.4, Equation 6.39 becomes

$$2.5 \text{ nm/s} = s(282 \text{ nm/s}) \quad (6.42)$$

which gives $s = 0.0089$. Using this value of sticking coefficient gives the corresponding SIMBAD depiction shown in Figure 6.53b.

As can be seen in this figure, there is very good agreement between the experimental and simulation results in terms of step coverage and film microstructure. The observed coverage of 0.70 is comparable to the simulated value of 0.72 and the column shape and orientation is also successfully depicted. Two SIMBAD deficiencies should be noted, however. First, the SIMBAD films do not close as tightly together in the centre. This is due to a decrease in ballistic transport efficiency as the gap approaches the size of a SIMBAD disc. At these dimensions, the disc is more likely to strike the film sides than a much smaller atom would. Consequently, an insufficient number of discs penetrate narrowing regions to close these gaps.

The second SIMBAD artifact is the formation of large wedge-shaped columns at the feature mouth. The experimental films show a fan shaped array of columns at these locations because of the highly convex nature of the topography there. This results in decreased competition between columns for the incident flux and allows columns that were initially smaller than a SIMBAD disc to grow to substantial size. However, since SIMBAD cannot represent film structure at sub-disc dimensions, its depictions show only a few large columns rather than several smaller ones. These problems can be reduced by decreasing the size of the SIMBAD disc at the cost of longer execution time and larger memory requirements.

Despite these minor shortcomings, however, the good agreement between the experimental and SIMBAD results indicates the potential usefulness of the model.

6.5 Applications of SIMBAD CVD

There are a number of possible applications for a SIMBAD model of refractory metal CVD. An obvious example is to examine the effect of the sticking coefficient on film coverage and structure. Also, the interest in higher pressure tungsten deposition suggests examining the effects of gas scattering inside topography using the model. Another possible application is to examine the implications of selective deposition where the film only grows on certain materials (such as silicon or metal) and not on others (such as oxides). Each of these example applications are discussed below.

6.5.1 Effects of Sticking Coefficient

Figure 6.54 illustrates the effect of sticking coefficient on CVD film coverage and microstructure. Three SIMBAD films are shown deposited over high aspect ratio topography at high, intermediate, and low sticking coefficients. These films demonstrate the importance of low sticking in attaining conformal coverage. The high sticking film is more characteristic of physical vapor deposition methods (for example, sputtering) than CVD and is discontinuous at the bottom of the sidewalls. The columns inside the feature for this film tend to be small and angled toward the mouth of the feature. On the other hand, the intermediate and low sticking coefficient films are more characteristic of refractory metal CVD films and have larger columns, which are oriented perpendicular to the underlying substrate and possess an overall higher density along

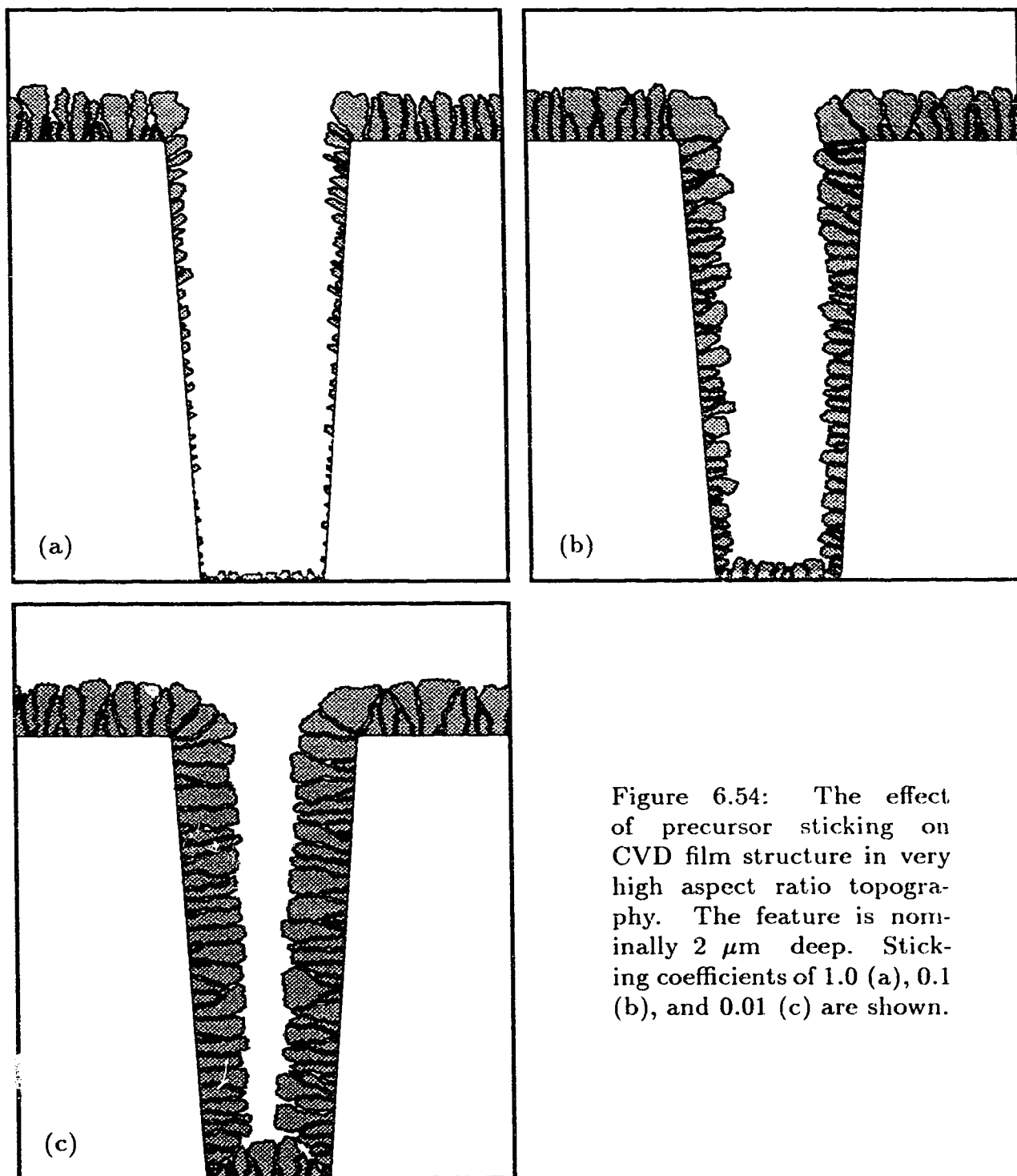


Figure 6.54: The effect of precursor sticking on CVD film structure in very high aspect ratio topography. The feature is nominally $2\ \mu\text{m}$ deep. Sticking coefficients of 1.0 (a), 0.1 (b), and 0.01 (c) are shown.

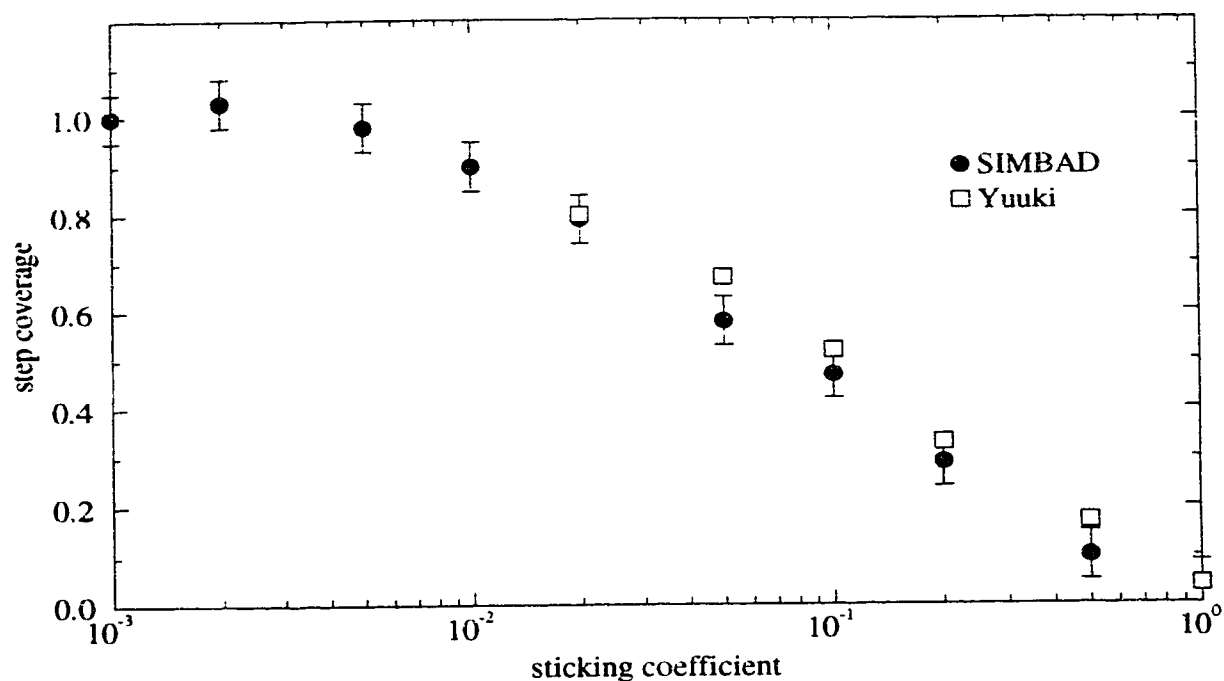


Figure 6.55: The effect of sticking coefficient on step coverage for a 2:1 trench with vertical sidewalls. Results from SIMBAD and Yuuki *et al.* [151] are shown.

the sidewalls.

Even though the low sticking coefficient film has good sidewall coverage near the bottom, cracks can be seen extending into the corners, where the vertical columns growing up from the bottom collide with the horizontal ones extending from the sidewalls. These cracks are also visible in experimental films deposited over trenches and vias, [137] and may be a concern for reliability — especially of diffusion barriers, since the cracks provide a diffusion path right through the film. [146]

Figure 6.55 shows the variation in step coverage with sticking coefficient over a 2:1 aspect trench with vertical sidewalls. As can be seen, there is approximately an exponential relation above a sticking coefficient of about 0.01 and virtually conformal

coverage below this value. Also shown in this graph are corresponding data measured from a string algorithm study by Yuuki *et al.* [151] The trend in their results is in overall agreement with those from SIMBAD although some discrepancies are to be expected due to differences in the respective angular distributions and representations.

6.5.2 Effects of Pressure

Since refractory metal CVD is usually performed one wafer at a time, it is desirable to keep deposition times low in order to maintain acceptable throughput. One way to increase deposition rates to achieve this goal is by increasing pressure. [136] However, there is concern about the effects higher pressures will have on step coverage. As the mean free path between collisions becomes less than the feature size, gas scattering will reduce the amount of material that reaches the bottom of vias and trenches and thereby reduce film growth and coverage there. [136]

Figure 6.56 shows the effect of increasing pressure on CVD film coverage using SIMBAD with two different sticking coefficients. In order to convert pressures into mean free paths for use in SIMBAD, Equation 3.14 was used with an assumed gas temperature of 400°C. Also, a collision cross-section of 180 Å² was approximated based on data for moderate-sized molecules in O'Hanlon. [90] This figure shows that step coverage does fall off with pressure at constant sticking coefficient due to scattering in the feature. (Of course, the sticking coefficient may also vary with pressure due to changes in impingement and reaction rates.) The magnitude of this effect varies with s as the relative coverage decreases less with pressure at lower sticking coefficients.

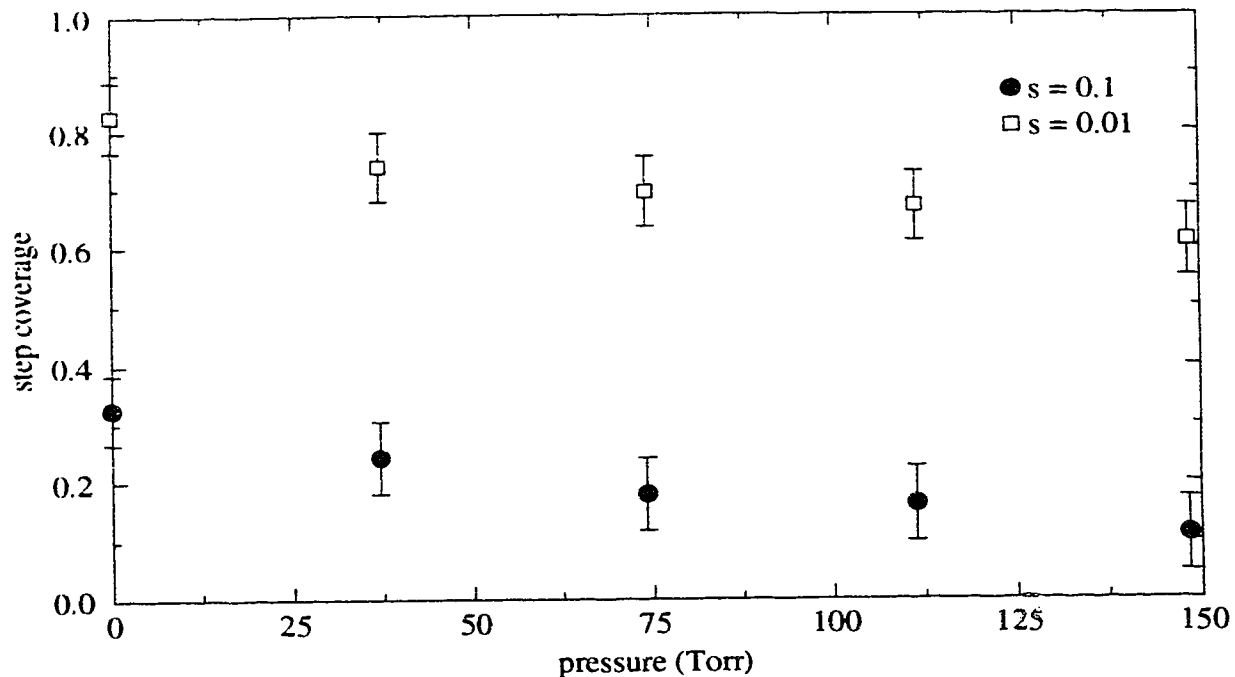


Figure 6.56: The effect of pressure on step coverage for a simulated $0.6 \mu\text{m}$ by $2 \mu\text{m}$ trench. Results for two different sticking coefficients are shown.

This effect may ultimately limit the maximum pressure that can be used without coverage degradation unless compensations in sticking coefficient are made.

6.5.3 Selective Deposition

One potentially useful variation of metal CVD is selective deposition on specific surfaces. This is possible because materials such as silicon or metals catalyze the CVD reaction much more readily than do oxides. With careful control of the deposition conditions, the reaction can be made to proceed only on these catalyzing materials. [26,136]

This is advantageous since it allows via plugs (of any diameter) to be produced without

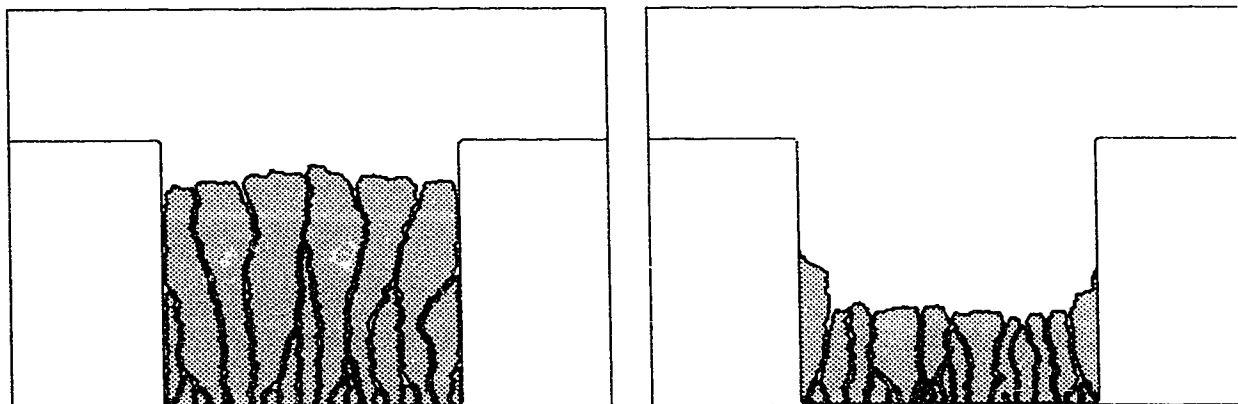


Figure 6.57: Selective deposition (left) and selectivity loss resulting in sidewall creep (right).

an additional etchback step and also drastically reduces the amount of the reactant gases required. [136] A drawback of this approach is that it requires all the vias to be of nearly the same depth or additional steps will be needed to planarize after deposition. [136] Commercial applications of selective CVD still await further development which could profit from a SIMBAD model of this process.

The primary addition to SIMBAD CVD to incorporate selective deposition is to allow the sticking coefficient to vary over the substrate. Any surface with non-zero sticking becomes selected. Selective deposition of refractory materials such as tungsten results in films with a unique microstructure comprised of long sinuous columns growing out of the selected surface. [139] Figure 6.57a shows that the SIMBAD model reproduces this characteristic selective column structure. Microstructure such as this is potentially important because, for plug applications, the current flow is in the same direction as the column orientation — in contrast to blanket CVD plugs. Also, these plugs have no central seam (where the sides grew together) or corner cracks and may serve as better diffusion barriers as a result.

One problem currently observed with selective deposition of tungsten is selectivity loss. This occurs when reaction byproducts diffuse onto unselected surfaces and chemically attack them. [26,136] This creates defects which can nucleate film growth which is then self-catalyzing. Most commonly, this causes the film to “creep up” the sidewalls. [26,136] The SIMBAD model can be extended to depict this problem (See Figure 6.57b) by increasing the likelihood of the reaction products diffusing onto the sidewalls to create a site for further nucleation.

6.6 Summary

A general SIMBAD refractory metal CVD model has been developed and verified through direct comparison with reported experimental results. The model shows that virtually conformal films, even over very high aspect ratio features, can be obtained provided that a low precursor sticking coefficient is used. The characteristic refractory CVD microstructure (including that of selective deposition) has been reproduced by the SIMBAD model. However, due to the high resistivity of the refractory materials, it is likely that this process will be used mainly to form via plugs and barrier layers, and deposition techniques from one of the previous chapters will be used to complete the metallization.

Chapter 7

Conclusions and Recommendations

7.1 Conclusions

This thesis has presented the extension of the SIMBAD simulation and the development of the SIMSPUD model as tools for designing and analyzing advanced metallization techniques. These are intended for use by a process designer or metallization engineer to assess, develop, or optimize a specific metallization process with minimal costly and time-consuming experimental analysis. Toward this end, a preliminary version of SIMBAD is being released commercially by the Alberta Microelectronic Centre. In addition, a more powerful version is planned for the near future which will contain many of the extensions discussed in this work. A brief summary of the extensions presented in this thesis and their original contributions is given below.

7.1.1 Sputter Distributions

The SIMSPUD simulation, described in Chapter 3, can be used to predict the angular, energy, and spatial distributions of sputtered material arriving at the target. This information can be utilized by SIMBAD to predict the effects on uniformity, step coverage, film microstructure, and stoichiometry of parameters such as magnetron

design; sputter gas pressure, temperature, and species; target species and voltage; target-substrate separation; substrate position; and substrate topography. While other models have been developed to provide some of the distribution information generated by SIMSPUD, none have previously been integrated with a film deposition model, such as SIMBAD and, therefore, lack the ability to translate most of their results into predictions of film properties. Also, previous models have either been limited in applicability, detail, or have been too computationally intensive to be of practical use.

Other original contributions of this chapter include the first detailed simulation of swept-magnetron sputtering systems and the first prediction of stoichiometric variations of alloys sputtered over topography. Results of the SIMSPUD/SIMBAD model suggest that even optimized distributions cannot yield adequate step coverage for vertical features with aspect ratios approaching 1.

7.1.2 Bias Sputtering

The addition of ion bombardment effects discussed in Chapter 4 allows SIMBAD to simulate the simultaneous deposition and ion etching involved in bias sputtering. This allows such a process to be optimized with respect to enhancing coverage and planarity while minimizing ion damage. While the earlier work of Bader and Lardon [108, 109] presented a similar model, it omitted the important effects of surface diffusion and ion reflection. In addition, their work involved a string algorithm representation and could not provide any microstructural information. The SIMBAD model rectifies these deficiencies and also provides the first detailed model which allows analysis

of ion damage to the substrate in the context of bias sputtering over high aspect ratio topography. Predictions of the model indicate that bias sputtering can provide adequate step coverage for aspect ratios near 1, but not without special measures to reduce substrate damage.

7.1.3 High Temperature Deposition

Efforts to extend the range of surface diffusion and incorporate the effects of capillarity have been discussed in Chapter 5 and the results allow SIMBAD to successfully depict high temperature aluminum deposition over topography. This preliminary model is the first which successfully demonstrates the observed filling of high aspect topography at elevated temperatures. Predictions indicate that high aspect ratios (above 1) can be completely filled but only by using very high temperatures during deposition. These temperatures can be reduced by simultaneous bias sputtering. A more sophisticated SIMBAD high temperature model is under development in collaboration with Dr. T. Smy. The purpose of this advanced model will be to examine the role of substrate wetting and nucleation on high temperature film deposition. (The contribution of Dr. Smy in co-developing the theory and simulation for the preliminary high temperature model is re-emphasized here.)

7.1.4 Refractory Metal CVD

The final extension in this work is the development in Chapter 6 of a general SIMBAD model for refractory metal CVD. The resulting simulations successfully capture the characteristic columnar microstructure and conformal coverage of these films.

Previous CVD models have employed string algorithms and have been unable to depict this microstructure. Extensions of the SIMBAD model to higher pressure and selective deposition models have also been made. Model results indicate that even extremely high aspect ratio features can be adequately covered provided that the sticking coefficient is suitably low.

7.2 Recommendations for Further Work

There are four general areas for further work to enhance the usefulness and power of these models. First, it would be desirable to establish a database of model parameter values (such as gas scattering cross-sections, surface diffusion lengths, or sticking coefficients) for a wide variety of materials and conditions. This would enable the casual user of the simulation to get useful information more quickly and with very little preparatory effort. Second, various parts of the existing model could be refined to give more accurate depictions. For example, the effects of anisotropic interfacial energies could be incorporated into the high temperature model or a variable sticking coefficient could be included in the CVD model. The third area of future work could be in extending the SIMBAD model to different processes. For example, SIMBAD models for wet [67] and plasma [70] etching have been developed in conjunction with Dr. R.N. Tait *et al.* The fourth area for future development would be to exploit the microstructure information provided by SIMBAD to predict film performance and properties. For example, Dr. T. Smy *et al.* have developed a model for predicting resistivity, current density, and heating in films over topography using SIMBAD results. [158] In addition, they are developing an electromigration model which also

utilizes this microstructure information. [159] Other models could conceivably predict the effect of microstructure on permeability of diffusion barriers or on film stress and stress-induced migration.

Bibliography

- [1] W.R. Runyan, K.E. Bean, *Semiconductor Integrated Circuit Processing Technology*, Addison-Wesley, Reading, Mass., 1990.
- [2] "IBM First with 16Mb DRAM", *Semiconductor International*, April, 1992, p. 15.
- [3] S.M. Sze, *VLSI Technology*, Second Edition, edited by S.M. Sze, McGraw-Hill, New York, 1988, p. 1.
- [4] S.K. Tewksbury, *Wafer-Level Integrated Systems*, Kluwer Academic Publishers, Boston, 1989.
- [5] D.K. Ferry, L.A. Akers, E.W. Greeneich, *Ultra Large Scale Integrated Microelectronics*, Prentice Hall, New Jersey, 1988.
- [6] M. Domenici, "Modern Aspects of Silicon Technology for Microelectronics", *Wafer Scale Integration III*, edited by M. Sami, F. Distanto, North Holland, Amsterdam, 1990, p. 163.
- [7] P. Van Zant, *Microchip Fabrication*, Semiconductor Services, San Jose, 1985.
- [8] J.E. Kelly (III), D.J. Fleming, "Interconnection Technology and Manufacturability Issues", *Proceedings of the Advanced Metallization for ULSI Applications Conference*, Materials Research Society, Pittsburgh, 1992, p. 13.

- [9] R.K. Watts, "Lithography", in *VLSI Technology*, Second Edition, edited by S.M. Sze, McGraw-Hill, New York, 1988, p. 141.
- [10] P.T. Panousis, D.P. Favreau, S.M. Merchant, E.A. Dein, "Technology Directions in VLSI", keynote address at the Advanced Metallization for ULSI Applications Conference, October 8-10, 1991, Murray Hill, N.J.
- [11] T. Smy, R.N. Tait, M.J. Brett, "Ballistic Deposition Simulation of Vial Metallization Using a Quasi-Three-Dimensional Model", *IEEE Transactions on Computer-Aided Design*, Vol. 10, No. 1, 1992, p. 130.
- [12] A.G. Sabnis, "Multilevel Metallization Schemes", *VLSI Electronics 15 - VLSI Metallization*, edited by N.G. Einspruch, Academic Press, Orlando, 1987, p. 293.
- [13] A.G. Sabnis, "Gate Metallization", *VLSI Electronics 15 - VLSI Metallization*, edited by N.G. Einspruch, Academic Press, Orlando, 1987, p. 221.
- [14] C.R.M. Grovenor, *Microelectronic Materials*, Adam Hilger, Bristol, 1989.
- [15] J.M. Pimbley, M. Ghezzi, H.G. Parks, D.M. Brown, *Advanced CMOS Process Technology*, Academic Press, Orlando, 1989.
- [16] J.L. Vossen, J.J. Cuomo, "Glow Discharge and Sputter Deposition", in *Thin Film Processes*, edited by J.L. Vossen, W. Kern, Academic Press, New York, 1978, p. 11.
- [17] R.F. Bunshah, *Deposition Technologies for Films and Coatings*, Noyes Publications, New Jersey, 1982.
- [18] S.P. Murarka, "Metallization", in *VLSI Technology*, Second Edition, edited by S.M. Sze, McGraw-Hill, New York, 1988, p. 375.

- [19] S. Luce, S. Pennington, "Technology for 16-Mbit DRAM and 0.5- μm CMOS Logic", *1992 IEEE VLSI Multilevel Interconnection Conference Proceedings*, 1992, p. 55.
- [20] M.E. Gross, V.M. Donnelly, "Copper Metallization for ULSI: A Brief Review and Recent Results on MOCVD Film Growth and Nucleation Mechanisms on TiN", *Proceedings of the Advanced Metallization for ULSI Applications Conference*, Materials Research Society, Pittsburgh, 1992, p. 355.
- [21] A.E. Kaloyeros, A.N. Saxena, K. Brooks, S. Ghosh, E. Einsenbraun, "Blanket and Selective Copper CVD From $\text{Cu}(\text{FOD})_2$ for Multilevel Metallization", in *Advanced Metallizations in Microelectronics*, edited by A. Katz, S.P. Murarka, A. Appelbaum, Materials Research Society, Pittsburgh, 1990, p. 79.
- [22] W.S. Ruska, *Microelectronic Processing*, McGraw-Hill, New York, 1987.
- [23] D.W. Skelly, T.M. Lu, and D.W. Woodruff, "Metallization Techniques", *VLSI Electronics 15 - VLSI Metallization*, edited by N.G. Einspruch, Academic Press, Orlando, 1987, p. 101.
- [24] R.K. Waits, "Planar Magnetron Sputtering", in *Thin Film Processes*, edited by J.L. Vossen, W. Kern, Academic Press, New York, 1978, p. 131.
- [25] F.F. Chen, *Introduction to Plasma Physics and Controlled Fusion*, Plenum Press, New York, Second Edition, 1984.
- [26] A. Sherman, *Chemical Vapor Deposition for Microelectronics*, Noyes Publications, Park Ridge, New Jersey, 1987.

- [27] J.A. Schwarz, "Electromigration in Interconnects and Contacts", *VLSI Electronics 15 - VLSI Metallization*, edited by N.G. Einspruch, Academic Press, Orlando, 1987, p. 345.
- [28] R.N. Singh, "Metallurgical Properties of Thin Conducting Films", *VLSI Electronics 15 - VLSI Metallization*, edited by N.G. Einspruch, Academic Press, Orlando, 1987, p. 41.
- [29] D.C. Thomas, S.S. Wong, "A Planar Interconnection Technology Utilizing the Selective Deposition of Tungsten-Multilevel Implementation", *IEEE Transactions on Electron Devices*, Vol. ED-39, No. 4, 1992, p. 901.
- [30] B.J. Bartholomeusz, K.H. Muller, M.R. Jacobson, "Computer Simulation of the Nucleation and Growth of Optical Coatings", *Modeling of Optical Thin Films*, SPIE No. 821, 1987, p. 2.
- [31] C.A. Neugebauer, "Condensation, Nucleation, and Growth of Thin Films", in *Handbook of Thin Film Technology*, edited by L.I. Maissel, R. Cleug, McGraw-Hill, New York, 1983, p. 8-3.
- [32] B. Lewis, J.C. Anderson, *Nucleation and Growth of Thin Films*, Academic Press, New York, 1978.
- [33] M. Ohring, *The Materials Science of Thin Films*, Academic Press, Boston, 1992.
- [34] B.A. Movchan, A.V. Demchishin, "Study of the Structure and Properties of Thick Vacuum Condensates of Nickel, Titanium, Tungsten, Aluminum Oxide, and Zirconium Dioxide", *Fiz. Metal. Metalloved.*, Vol. 28, No. 4, 1969, p. 653.

- [35] R.N. Tait, *Thin Film Microstructure Effects in VLSI Metallization*, Ph.D. thesis, Department of Electrical Engineering, University of Alberta, Edmonton, 1992.
- [36] J.A. Thornton, "Influence of Apparatus Geometry and Deposition Conditions on the Structure and Topography of Thick Sputtered Coatings". *Journal of Vacuum Science and Technology*, Vol. 11, No. 4, 1974, p. 666.
- [37] J.A. Thornton, "High Rate Thick Film Growth", *Annual Review of Material Science*, Vol. 7, 1977, p. 239.
- [38] J.A. Thornton, "The Microstructure of Sputter-Deposited Coatings", *Journal of Vacuum Science and Technology A*, Vol. 4, No. 6, 1986, p. 3059.
- [39] H. Joswig, A. Kohlhase, P. Kücher, "Advanced Metallization of Very-Large-Scale Integration Devices". *Thin Solid Films*, Vol. 175, 1989, p. 17.
- [40] K.W. Harper, R.E. Jones, Jr., "A Comparison of Three-Dimensional and Two-Dimensional Simulations of Contact Step Coverage", *Journal of Vacuum Science and Technology A*, Vol. 5, No. 3, 1987, p. 333.
- [41] E.W. Scheckler, *Algorithms for Three-Dimensional Simulation of Etching and Deposition Processes in Integrated Circuit Fabrication*, Ph.D Dissertation, Electronics Research Laboratory, University of California, Berkeley, Memorandum No. UCB/ERL M91/99, 1991.
- [42] B.W. Dodson, "Molecular Dynamics Modeling of Vapor-Phase and Very-Low-Energy Ion-Beam Crystal Growth Processes", *CRC Critical Reviews in Solid State and Materials Sciences*, Vol. 16(2), 1990, p.115.

- [43] H.J. Leamy, G.H. Gilmer, A.G. Dirks, "The Microstructure of Vapor Deposited Thin Films", in *Current Topics in Materials Science, Volume 6*, edited by E. Kaldis, North-Holland, Amsterdam, 1980, p. 311.
- [44] K.-H. Müller, "Stress and Microstructure of Sputter-Deposited Thin Films: Molecular Dynamics Investigations", *Journal of Applied Physics*, Vol. 62, No. 5, 1987, p. 1796.
- [45] M. Schneider, A. Rahman, I. K. Schuller, "Vapor-Phase Growth of Amorphous Materials: A Molecular-Dynamics Study", *Physical Review B*, Vol. 34, No. 3, 1986, p. 1802.
- [46] P.K. Swaminathan, C.S. Murthy, M.J. Redmon, "Computer Simulations of Epitaxial Growth", *Physical Review B*, Vol. 39, No. 7, 1989, p. 4541.
- [47] *Handbook of Chemistry and Physics, 1st Student Edition*, edited by R.C. Weast, CRC Press, Boca Raton, 1988.
- [48] K.-H. Müller, "Monte Carlo Calculation for Structural Modifications in Ion-Assisted Thin Film Deposition Due to Thermal Spikes", *Journal of Vacuum Science and Technology A*, Vol. 4, No. 2, 1986, p. 184.
- [49] C.H. Ting, A.R. Neureuther, "Application of Profile Simulation for Thin Film Deposition and Etching Processes", *Solid State Technology*, February, 1982, p. 115.
- [50] J. McVittie, J. Rey, L.-Y. Cheng, A. Bariya, S. Ravi, K. Saraswat, "SPEEDIE: A Profile Simulator for Etching and Deposition", *TECHCON '90, Extended Abstract Volume*, Semiconductor Research Corporation, San Jose, 1990, p. 16.

- [51] *DEPICK-2*, Technology Modeling Associates, 300 Hamilton Avenue, third floor, Palo Alto, California.
- [52] Silvaco International, 4701 Patrick Henry Drive, Building 3, Santa Clara, California.
- [53] G.S. Bales, A. Zangwill, "Macroscopic Model for Columnar Growth of Amorphous Films by Sputter Deposition", *Journal of Vacuum Science and Technology A*, Vol. 9, No. 1, 1991, p. 145.
- [54] D. J. Srolovitz, A. Mazor, B.G. Bukiet, P.S. Hagan, "Theory and Simulations of Zone II Microstructures in Thin Films", *Journal of Vacuum Science and Technology A*, Vol. 9, No. 1, 1991, p. 145.
- [55] S. Lichter, J. Chen, "Model for Columnar Microstructure of Thin Solid Films", *Physical Review Letters*, Vol. 56, No. 13, 1986, p. 1396.
- [56] R.P.U. Karunasiri, R. Bruinsma, J. Rudnick, "Thin-Film Growth and the Shadow Instability", *Physical Review Letters*, Vol 62., No. 7, 1989, p. 788.
- [57] B.J. Palmer, R.G. Gordon, "Kinetic Model of Morphological Instabilities in Chemical Vapor Deposition", *Thin Solid Films*, Vol. 177, p. 141.
- [58] D. Henderson, M.H. Brodsky, P. Chauhari, "Simulation of Structural Anisotropy and Void Formation in Amorphous Thin Films", *Applied Physics Letters*, Vol. 25, No. 11, 1974, p. 641.
- [59] P. Meakin, P. Ramanlal, L.M. Sander, R.C. Ball, "Ballistic Deposition on Surfaces", *Physical Review A*, Vol. 34, No. 6, 1986, p. 5091.

- [60] M.J. Cooke, G. Harris, "Monte Carlo Simulation of Thin-Film Deposition in a Rectangular Groove", *Journal of Vacuum Science and Technology A*, Vol. 7, No. 6, 1989, p. 3217.
- [61] M.J. Brett, "Structural Transitions in Ballistic Aggregation Simulation of Thin-Film Growth", *Journal of Vacuum Science and Technology A*, Vol. 6, No. 3, 1988, p. 1749.
- [62] M.J. Brett, "Simulation of Structural Transitions in Thin Films", *Journal of Material Science*, Vol. 24, 1989, p. 623.
- [63] M.J. Brett, "Thin Film Deposition Profiles using a Ballistic Aggregation Model", *Journal of Material Science Letters*, Vol. 8, 1989, p. 415.
- [64] M.J. Brett, K.L. Westra, T. Smy, "Simulation of Thin Film Step Coverage and Microstructure", *Canadian Journal of Physics*, Vol. 67, No. 4, 1989, p. 347.
- [65] K.L. Westra, T. Smy, M.J. Brett, "Simulation by Ballistic Deposition of Local Density Variation and Step Coverage for Via Metallization", *IEEE Electron Device Letters*, Vol. 10, No. 5, 1989, p. 198.
- [66] T. Smy, K.L. Westra, M.J. Brett, "Simulation of Density Variations and Step Coverage for a Variety of Via/Contact Geometries Using SIMBAD", *IEEE Transactions on Electron Devices*, Vol. 37, 1990, p. 591.
- [67] R.N. Tait, S.K. Dew, T. Smy, M.J. Brett, "Density Variations of Tungsten Films Sputtered over Topography", *Journal of Applied Physics*, Vol. 70, No. 8, 1991, p. 4295.

- [68] R.N. Tait, S.K. Dew, T. Smy, M.J. Brett, "Ballistic Simulation of Optical Coatings Deposited over Topography", *SPIE Proceedings 1324*, 1990, p. 112.
- [69] E.P. Lozowski, M. Brett, N. Tait, T. Smy, "Simulating Giant Hailstone Structure with a Ballistic Aggregation Model", *Quarterly Journal of the Royal Meteorological Society*, Vol. 117, 1991, p. 427.
- [70] R.N. Tait, S.K. Dew, T. Smy, M.J. Brett, "Etching of Thin Metal Films Using a Ballistic Model", to be published in *Journal of Vacuum Science and Technology A*, July/August, 1992.
- [71] M.J. Brett, R.N. Tait, S.K. Dew, S. Kamasz, A.H. Labun, T. Smy, "Nodular Defect Growth in Thin Films", *Journal of Materials Science: Materials in Electronics*, Vol. 3, 1992, p. 64.
- [72] S.K. Dew, T. Smy, R.N. Tait, M.J. Brett, "Modeling Bias Sputter Planarization of Metal Films Using a Ballistic Deposition Simulation", *Journal of Vacuum Science and Technology A*, Vol. 9, No. 3, 1991, p. 519.
- [73] S.K. Dew, T. Smy, M.J. Brett, "Thin Film Microstructure Simulation of RF Bias Planarized Metal Interconnects Using a Ballistic Deposition Model", *1991 IEEE VLSI Multilevel Interconnection Conference Proceedings*, 1991, p. 353.
- [74] S.K. Dew, T. Smy, M.J. Brett, "Simulation of Elevated Temperature Aluminum Metallization Using SIMBAD", *IEEE Transactions on Electron Devices*, Vol. 39, No. 7, 1992, p. 1599.

- [75] T. Smy, S.K. Dew, M.J. Brett, "Simulation of High Temperature Via Filling Using SIMBAD", *1992 IEEE VLSI Multilevel Interconnection Conference Proceedings*, 1992, p. 465.
- [76] S.K. Dew, T. Smy, M.J. Brett, "Simulation of the Microstructure of Chemical Vapor Deposited Refractory Thin Films", *Journal of Vacuum Science and Technology B*, Vol. 10, No. 2, 1992, p. 618.
- [77] S.K. Dew, T. Smy, M.J. Brett, "Microstructure Simulation of CVD Refractory Films", in *Advanced Metallization for ULSI Applications*, edited by V.V.S. Rana, R.V. Joshi, I. Ohdomari, Materials Research Society, Pittsburgh, 1992, p. 85.
- [78] D. Gupta, P.S. Ho, *Diffusion Phenomena in Thin Films and Microelectronic Materials*, Noyes Publications, Park Ridge, New Jersey, 1988.
- [79] H.P. Bonzel, "Transport of Matter at Surfaces", in *Surface Physics of Materials, Volume II*, edited by J.M. Blakely, Academic Press, New York, 1975, p. 280.
- [80] R.E. Somekh, "The Thermalization of Energetic Atoms During the Sputtering Process", *Journal of Vacuum Science and Technology A*, Vol. 2, No. 3, 1984, p. 1285.
- [81] K. Meyer, I.K. Schuller, C.M. Falco, "Thermalization of Sputtered Atoms", *Journal of Applied Physics*, Vol. 52, No. 9, 1981, p. 5803.
- [82] M.A. Vidal, R. Asomoza, "Monte Carlo Simulation of the Transport Process in the Growth of α -Si:H Prepared by Cathodic Reactive Sputtering", *Journal of Applied Physics*, Vol. 67, No. 1, 1990, p. 477.

- [83] S.M. Rossnagel, "Sputtered Atom Transport Processes", IEEE Transactions on Plasma Science", Vol. 18, No. 6, 1990, p. 878.
- [84] T. Motohiro, "Applications of Monte Carlo Simulation in the Analysis of a Sputter-Deposition Process", Journal of Vacuum Science and Technology A, Vol. 4, No. 2, 1986, p. 189.
- [85] G.M. Turner, I.S. Falconer, B.W. James, D.R. McKenzie, "Monte Carlo Calculation of the Thermalization of Atoms Sputtered from the Cathode of a Sputtering Discharge", Journal of Applied Physics, Vol. 65, No. 9, 1989, p. 3671.
- [86] G.L. Hansen, R.G. Ahonen, "The Effect of Gas Scattering on the Deposition Profile of Optical Thin Films", Journal of Vacuum Science and Technology A, Vol. 5, No. 5, 1987, p. 2898.
- [87] T. Heberlein, G. Krautheim, W. Wuttke, "The Sputter Deposition Process: A Monte Carlo Study", Vacuum, Vol. 42, Nos. 1/2, 1991, p. 47.
- [88] A.M. Myers, J.R. Doyle, J.R. Abelson, "Monte Carlo Simulations of Magnetron Sputtering Particle Transport", Journal of Vacuum Science and Technology A, Vol. 9, No. 3, 1991, p. 614.
- [89] J.M. Nieuwenhuizen, H.B. Haanstra, "Microfractography of Thin Films", Philips Technical Review, Vol. 27, No. 3, 1966, p. 87.
- [90] J.F. O'Hanlon, *A User's Guide to Vacuum Technology*, Second Edition, Wiley, New York, 1989.
- [91] H. Tsuge, S. Esho, "Angular Distribution of Sputtered Atoms from Polycrystalline Metal Targets", Journal of Applied Physics, Vol. 52, No. 7, 1981, p. 4391.

- [92] H. Oechsner, "Sputtering - A Review of Some Recent Experimental and Theoretical Aspects", *Applied Physics*, Vol. 8, 1975, p. 185.
- [93] W.D. Davis, T.A. Vanderslice, "Ion Energies at the Cathode of a Glow Discharge", *Physical Review*, Vol. 131, No. 1, 1963, p. 219.
- [94] M.J. Goeckner, J.A. Goree, T.E. Sheridan, Jr., "Monte Carlo Simulation of Ions in a Magnetron Plasma", *IEEE Transactions on Plasma Science*, Vol. 19, No. 2, 1991, p. 301.
- [95] J. Rickards, "Energies of Particles at the Cathode of a Glow Discharge", *Vacuum*, Vol. 34, No. 5, 1990, p. 559.
- [96] L.D. Landau, E.M. Lifshitz, *Mechanics*, Third Edition, Pergammon, London, 1960.
- [97] R. Razdan, *Magnetic Stabilization of Laser Gas Discharges*, Ph.D. thesis, Department of Electrical Engineering, University of Alberta, Edmonton, 1987.
- [98] R.S. Robinson, "Energetic Binary Collisions in Rare Gas Plasmas", *Journal of Vacuum Science and Technology*, Vol. 16, No. 2, 1979, p. 185.
- [99] W.D. Westwood, "Calculation of Deposition Rates in Diode Sputtering Systems", *Journal of Vacuum Science and Technology*, Vol. 15, No. 1, 1978, p. 1.
- [100] W.H. Press, B.P. Flannery, S.A. Teukolsky, W.T. Vetterling, *Numerical Recipes in C*, Cambridge University Press, Cambridge, 1988.
- [101] J.L. Devore, *Probability and Statistics for Engineering and the Sciences*, Brooks, Monterey, 1982.

- [102] C. Kittel, *Introduction to Solid State Physics*, Sixth Edition, Wiley, New York, 1986.
- [103] "The Quantum SputteringTM Source", Varian Semiconductor Equipment Newsletter, edited by N. Gross, 3045 Hanover Street, Palo Alto, California, 1992.
- [104] T. Mogami, H. Okabayashi, E. Nagasawa, M. Morimoto, "Planarized Molybdenum Interconnections Using Via-Hole Filling by Bias Sputtering", *1985 IEEE VLSI Multilevel Interconnection Conference Proceedings*, 1985, p. 17.
- [105] Y. Homma, S. Tsunekawa, "Planar Deposition of Aluminum by RF/DC Sputtering with RF Bias", *Journal of the Electrochemical Society*, Vol. 132, No. 6, 1985, p. 1467.
- [106] D.W. Skelly, L. V. Gruenke, "Significant Improvement in Step Coverage Using Bias Sputtered Aluminum", *Journal of Vacuum Science and Technology A*, Vol. 4, No. 3, 1986, p. 457.
- [107] J.F. Smith, "Influence of DC Bias Sputtering During Aluminum", *Solid State Technology*, January, 1984, p. 135.
- [108] H.P. Bader, M.A. Lardon, "Planarization by Radio-Frequency Bias Sputtering of Aluminum as Studied Experimentally and by Computer Simulation", *Journal of Vacuum Science and Technology A*, Vol. 3, No. 6, 1985, p. 2167.
- [109] H.P. Bader, M.A. Lardon, "Topographical Limitations to the Metallization of Very Large Scale Integrated Structures by Bias Sputtering: Experiments and Computer Simulations", *Journal of Vacuum Science and Technology B*, Vol. 4, No. 5, 1986, p. 1192.

- [110] A. Wucher, W. Reuter, "Angular Distribution of Particles Sputtered from Metals and Alloys", *Journal of Vacuum Science and Technology A*, Vol. 6, No. 4, 1988, p. 2316.
- [111] S.G. Ingram, "The Influence of Substrate Topography on Ion Bombardment in Plasma Etching", *Journal of Applied Physics*, Vol. 68, No. 2, 1990, p. 500.
- [112] W. Eckstein, J.P. Biersack, "Self-Sputtering and Reflection", *Zeitschrift für Physik B*, Vol. 63, 1986, p. 109.
- [113] M. Hou, M.T. Robinson, "The Conditions for Total Reflection of Low-Energy Atoms from Crystal Surfaces", *Applied Physics*, Vol. 17, 1978, p. 371.
- [114] M.T. Robinson, "Theoretical Aspects of Monocrystal Sputtering" in *Sputtering by Particle Bombardment, I*, edited by R. Behrisch, Springer-Verlag, Berlin, 1981, p. 73.
- [115] *SAMPLE User Guide, V.1.7a*, University of California at Berkeley, 1989, p. 99.
- [116] W.O. Hofer, "Angular, Energy, and Mass Distribution of Sputtered Particles" in *Sputtering by Particle Bombardment, III*, edited by R. Behrisch, K. Wittmaack, Springer-Verlag, Berlin, 1991, p. 15.
- [117] I. Petrov, L. Hultman, J.E. Sundgren, J.E. Greene, "Polycrystalline TiN Films Deposited by Reactive Bias Magnetron Sputtering: Effects of Ion Bombardment on Resputtering Rates, Film Composition, and Microstructure", *Journal of Vacuum Science and Technology A*, Vol. 10, No. 2, 1992, p. 265.
- [118] *SEM-8620 Operating and Maintenance Manual*, Materials Research Corporation, p. IV-3.

- [119] S.M. Rossnagel, D. Mikalsen, H. Kinoshita, J.J. Cuomo, "Collimated Magnetron Sputter Deposition", *Journal of Vacuum Science and Technology A*, Vol. 9, No. 2, 1991, p. 261.
- [120] H.P. Bader, M.A. Lardon, "A New Metallization Technique for Very Large Scale Integrated Structures: Experiments and Computer Simulation", *Journal of Vacuum Science and Technology B*, Vol. 4, No. 4, 1986, p. 833.
- [121] M. Inoue, K. Hashizume, H. Tsuchikawa, "The Properties of Aluminum Thin Films Sputter Deposited at Elevated Temperatures", *Journal of Vacuum Science and Technology A*, Vol. 6, No. 3, 1988, p. 1636.
- [122] R. Burggraaf, "Sputtering's Task: Metalizing Holes", *Semiconductor International*, December, 1990, p. 28.
- [123] D. Pramanik, A.N. Saxena, "Aluminum Metallization for ULSI ", *Solid State Technology*, March, 1990, p. 73.
- [124] F.S. Chen, Y.S. Lin, G.A. Dixit, R. Sundaresan, C. C. Wei, F.T. Liou, "Planarized Aluminum Metallization for Sub-0.5 μm CMOS Technology", *Transactions of the 1990 IEEE Electron Devices Meeting*, 1990, p. 51.
- [125] A. Al-Jon, I. Wagner, "Advanced Aluminum Metallization: Part II - Planarization", in *Advances in Magnetron Sputtering and Etching*, Materials Research Corp., 1988.
- [126] H. Ono, Y. Ushiku, T. Yoda, "Development of a Planarized Al-Si Contact Filling Technology", *1991 IEEE VLSI Multilevel Interconnection Conference Proceedings*, 1991, p. 76.

- [127] K. Kikuta, T. Kikkawa, M. Aoki, "Al-Ge Reflow Sputtering for Submicron-Contact-Hole Filling", *1991 IEEE VLSI Multilevel Interconnection Conference Proceedings*, 1991, p. 163.
- [128] M. Taguchi, K. Koyama, Y. Sugano, "Quarter Micron Hole Filling with SiN Sidewalls by Aluminum High Temperature Sputtering", *1992 IEEE VLSI Multilevel Interconnection Conference Proceedings*, 1992, p. 219.
- [129] G. Neumann, W. Hirschwald, "The Mechanisms of Surface Self Diffusion", *Z. Physik. Chem. Neue Folge*, Vol. 81, 1972, p. 176.
- [130] G. Carter, "The Influence of Surface Diffusion on Topography Development of an Amorphous Solid During Sputtering", *Journal of Material Science*, Vol. 11, 1976, p. 1091.
- [131] M.R. Spiegel, *Mathematical Handbook*, McGraw-Hill, New York, 1968.
- [132] J. Bass, "The Formation and Motion of Vacancies in Aluminum", *Phil. Mag.*, Vol. 15, 1967, p. 717.
- [133] A. Zangwill, *Physics at Surfaces*, Cambridge University Press, Cambridge, 1988.
- [134] W.W. Mullins, "Theory of Thermal Grooving", *Journal of Applied Physics*, Vol. 28, No. 3, 1957, p. 333.
- [135] R. Glang, "Vacuum Evaporation", in *Handbook of Thin Film Technology*, edited by L.I. Maissel, R. Glang, McGraw-Hill, New York, 1983, p. 1-3.
- [136] J.E. Schmitz, *Chemical Vapor Deposition of Tungsten and Tungsten Silicides*, Noyes Publications, Park Ridge, New Jersey, 1992.

- [137] K. Ishihara, T. Yamada, S. Onishi, K. Matsuda, K. Sakiyama, "Ti/CVD- WSi_x /Blanket-W Structure for Fine Contact Filling Application", *1991 IEEE VLSI Multilevel Interconnection Conference Proceedings*, 1991, p. 185.
- [138] R.S. Rosler, J. Mendona, M. J. Rice, Jr., "Tungsten Chemical Vapor Deposition Characteristics using SiH_4 in a Single Wafer System", *Journal of Vacuum Science and Technology B*, Vol. 6, No. 6, 1988, p. 1721.
- [139] R.S. Blewer, "Progress in LPCVD Tungsten for Advanced Microelectronics Applications", *Solid State Technology*, Vol. 29, No. 11, 1986, p. 117.
- [140] M.J. Buiting and A.H. Reader, in *Chemical Vapor Deposition of Refractory Metals and Ceramics*, edited by T.M. Besmann and B.M. Gallois, Material Research Society Proceedings, Vol. 168, Pittsburgh, 1990, p. 199.
- [141] I.J. Raaijmakers, A. Sherman, "Contact Hole Fill with Low Temperature LPCVD TiN", *1990 IEEE VLSI Multilevel Interconnection Conference Proceedings*, 1990, p. 219.
- [142] S. Sachdev, R. Castellano, "CVD Tungsten and Tungsten Silicide for VLSI Applications", *Semiconductor International*, May, 1985.
- [143] C. Bernard, R. Madar, Y. Pauleau, "Chemical Vapor Deposition of Refractory Metal Silicides for VLSI Metallization", *Solid State Technology*, February, 1989, p. 79.
- [144] R. Comerford, "How DEC Developed Alpha", *IEEE Spectrum*, July, 1992, p. 26.

- [145] S.S. Cohen, "Electrical Properties of Thin Conducting Films", *VLSI Electronics 15 - VLSI Metallization*, edited by N.G. Einspruch, Academic Press, Orlando, 1987, p. 1.
- [146] D. Pramanik, V. Jain, "Barrier Metals for ULSI: Processing and Reliability", *Solid State Technology*, Vol. 34, No. 5, 1991, p. 97.
- [147] W. Kern, V.S. Ban, "Chemical Vapor Deposition of Inorganic Thin Films", in *Thin Film Processes*, edited by J.L. Vossen, W. Kern, Academic Press, New York, 1978, p. 258.
- [148] T.E. Clark, P.E. Riley, M. Chang, S.G. Ghanayem, C. Leung, A. Mak, "Integrated Deposition and Etchback of Tungsten in a Multi-Chamber, Single-Wafer System", *1990 IEEE VLSI Multilevel Interconnection Conference Proceedings*, 1990, p. 478.
- [149] L.-Y. Cheng, J.C. Rey, J.P. McVittie, K.C. Saraswat, "Sticking Coefficient as a Single Parameter to Characterize STep Coverage of SiO₂ Processes", *1990 IEEE VLSI Multilevel Interconnection Conference Proceedings*, 1990, p. 404.
- [150] J.C. Rey, L.-Y. Cheng, J.P. McVittie, K.C. Saraswat, "Numerical Simulation of CVD Trench Filling Using a Surface Reaction Coefficient Model", *1990 IEEE VLSI Multilevel Interconnection Conference Proceedings*, 1990, p. 425.
- [151] A. Yuuki, Y. Matsui, K. Tachibana, "A Study on Radical Fluxes in Silane Plasma CVD from Trench Coverage Analysis", *Japanese Journal of Applied Physics*, Vol. 28, No. 2, 1989, p. 212.

- [152] M. Ikegawa, J. Kobayashi, "Deposition Profile Simulation Using the Direct Simulation Monte Carlo Method", *Journal of the Electrochemical Society*, Vol. 136, No. 10, 1989, p. 2982.
- [153] J.G. Shaw, C.C. Tsai, "Monte Carlo Simulations of Plasma-Deposited Amorphous Silicon", *Journal of Applied Physics*, Vol. 64, No. 2, 1988, p. 699.
- [154] P.-Y. Lesaicherre, A. Gerodolle, P. Brouget, N. Rossiter, "Characterization and Simulation of PECVD and APCVD Oxide Step Coverage", *1990 IEEE VLSI Multilevel Interconnection Conference Proceedings*, 1990, p. 159.
- [155] T.S. Cale, G.B. Raupp, "A Unified Line-of-Sight Model of Deposition in Rectangular Trenches", *Journal of Vacuum Science and Technology B*, Vol. 8, No. 6, 1990, p. 1242.
- [156] C. Kittel, H. Kroemer, *Thermal Physics*, Second Edition, Wiley, New York, 1980.
- [157] A. Hasper, J. Holleman, J. Middelhoek, C.R. Kleijn, J. Hoogendoorn, "Modeling and Optimization of the Step Coverage of Tungsten LPCVD in Trenches and Contact Holes", *Journal of the Electrochemical Society*, Vol. 138, No. 6, 1991, p. 1728.
- [158] T. Smy, D.J. Reny, M.J. Brett, "Simulation of the Effect of Thin Film Microstructure on Current and Temperature Distribution in VLSI Metalization Structures", accepted for publication in *Journal of Vacuum Science and Technology B*, October, 1992.

- [159] T. Smy, S.S. Winterton, M.J. Brett, "Simulation of Metal Line Failure by Electromigration Using a Monte Carlo Method", *1992 IEEE VLSI Multilevel Interconnection Conference Proceedings*, 1992, p. 441.

Appendix A

Quasi-3D SIMBAD

For a typical via, the topography is often cylindrically symmetric about the via axis. (This means that any vertical slice through the via centre will have the same cross-section.) If there is also similar symmetry in the incident angular distribution (a reasonable approximation unless the topography is far from the axis of deposition), it is possible to project the three-dimensional shadowing problem into a two-dimensional one which, with minor variation, is suitable for solution by SIMBAD. Unfortunately, such a SIMBAD model is not fully equivalent to three dimensions as surface diffusion must proceed in a two dimensional approximation. However, for small diffusion lengths, this is still a reasonable approximation.

In this quasi-3D model, positions and trajectories in the ballistic phase of SIMBAD are followed in all three dimensions, but the path is broken into small steps and at each step it is projected into two dimensions to allow SIMBAD to check for collisions with existing discs (quasi-spheres) or the substrate. (This projection is equivalent to rotating the 2D SIMBAD film about the central axis.) For example, if the trajectory of a disc takes it from A (See Figure A.58) towards B then the position at any point can be represented in cylindrical coordinates by $(\rho, \phi, h)_{3D}$. This can be projected

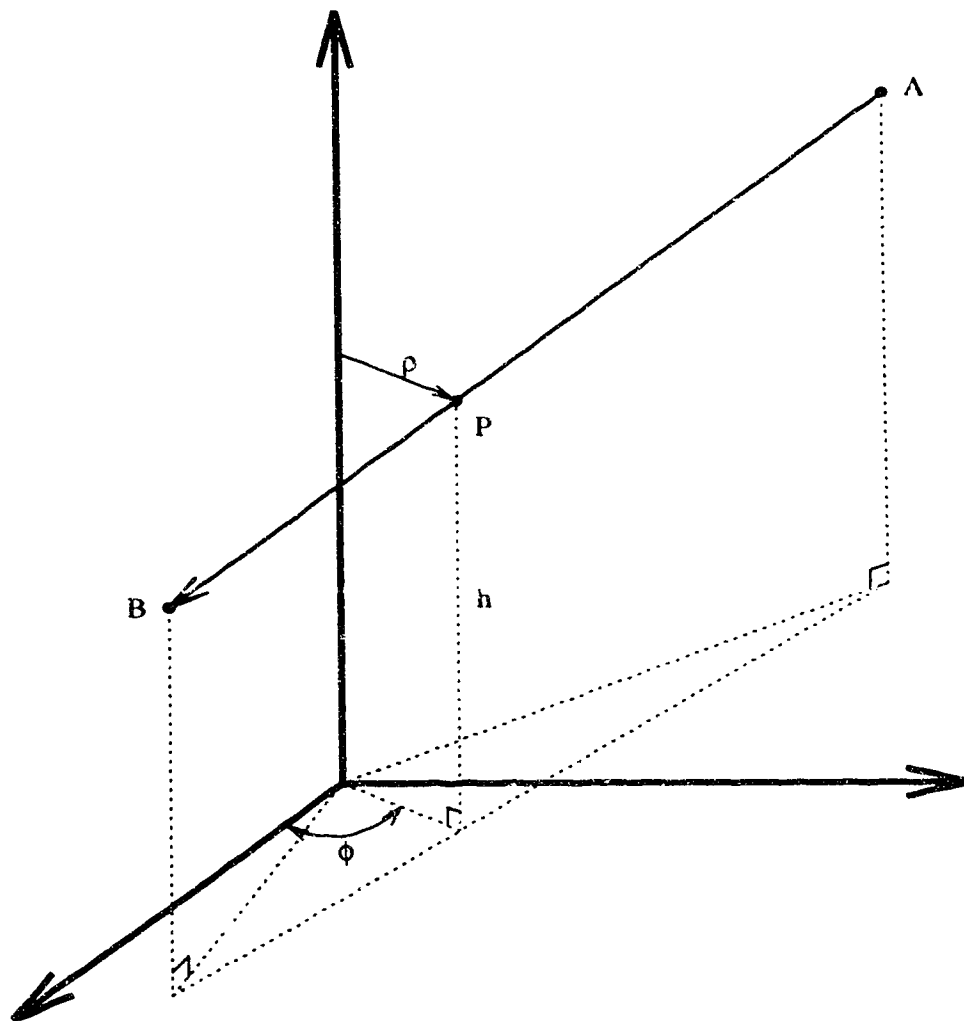


Figure A.58: Geometry used for quasi-3d SIMBAD model. The position P of a particle travelling from A to B is given in cylindrical coordinates by (ρ, ϕ, h)

into SIMBAD space as the position $(x, y)_{2D}$ by the mapping

$$x_{2D} = \rho \quad (\text{A.43})$$

$$y_{2D} = h \quad (\text{A.44})$$

(Due to the assumed rotational symmetry, there is no ϕ dependence in this projection.) Strictly speaking, x_{2D} should range from 0 to ρ_{max} . However, to minimize modifications to SIMBAD, x_{2D} ranges from $-\rho_{max}$ to ρ_{max} with the sign taken such that paths in SIMBAD are continuous and do not cross $x_{2D} = 0$. This means that the film is duplicated with the left half equivalent (but not identical due to random variations) to the right. This theoretically doubles the number of discs required for the simulation but maintains compatibility with existing routines and simplifies the boundary conditions at $x_{2D} = 0$ by eliminating the boundary. The boundary conditions at $\pm\rho_{max}$ are assumed to be periodic, as before. This assumption is not strictly valid for a cylindrical coordinate frame, but is a reasonable approximation for $\rho_{max} \gg \delta\rho$ (where $\delta\rho$ is the average change in radial position from particle generation to impact).

In addition to the 2D position at each step, SIMBAD requires the local trajectory in order to predict impact points. In two dimensions, this local trajectory varies even though in three dimensions the particle is travelling in a straight line. The 2D slope is given by

$$m_{2D} = \frac{dy_{2D}}{dx_{2D}} = \frac{d\rho}{dh} \quad (\text{A.45})$$

An analytic expression can be derived for $d\rho/dh$, but because the trajectory is generally skewed to the axis of symmetry, the relation is complex and computationally expensive to evaluate. Instead, since the particle's position in 2D is tracked in small

steps, it is convenient to approximate the local slope by

$$m_{2D} = \frac{\Delta y_{2D}}{\Delta x_{2D}} \quad (\text{A.46})$$

Finally, the weighting of particles must be considered. In cylindrical coordinates, more particles are generated and impact on the film at higher radii; however, their contributions are divided amongst a correspondingly larger area. This is because the area between ρ and $\rho + d\rho$ is given by $2\pi\rho d\rho$ and consequently increases linearly with ρ . Therefore, particles must be weighted by $1/\rho$ when adding to the film. However, since SIMBAD is a discrete simulation, this can be accomplished by throwing away many of the discs and only keeping a given disc with a probability proportional to $1/\rho$. Unfortunately, this weighting factor is singular at $\rho = 0$. Therefore, a truncation radius, w , must be specified below which the probability of keeping the disc is 1 and above which it is given by w/ρ . This creates a central notch of width $2w$ in the film, but a judicious choice of w can minimize this simulation artifact without unacceptably reducing the simulation efficiency.

The success of this quasi-3D model can be verified by comparing the resulting via profile with the corresponding experimental one. (See Figure A.59.) The bottom and sidewall coverage of the via is correctly predicted to be lower than that for a trench as can be seen in the corresponding Figure A.60.

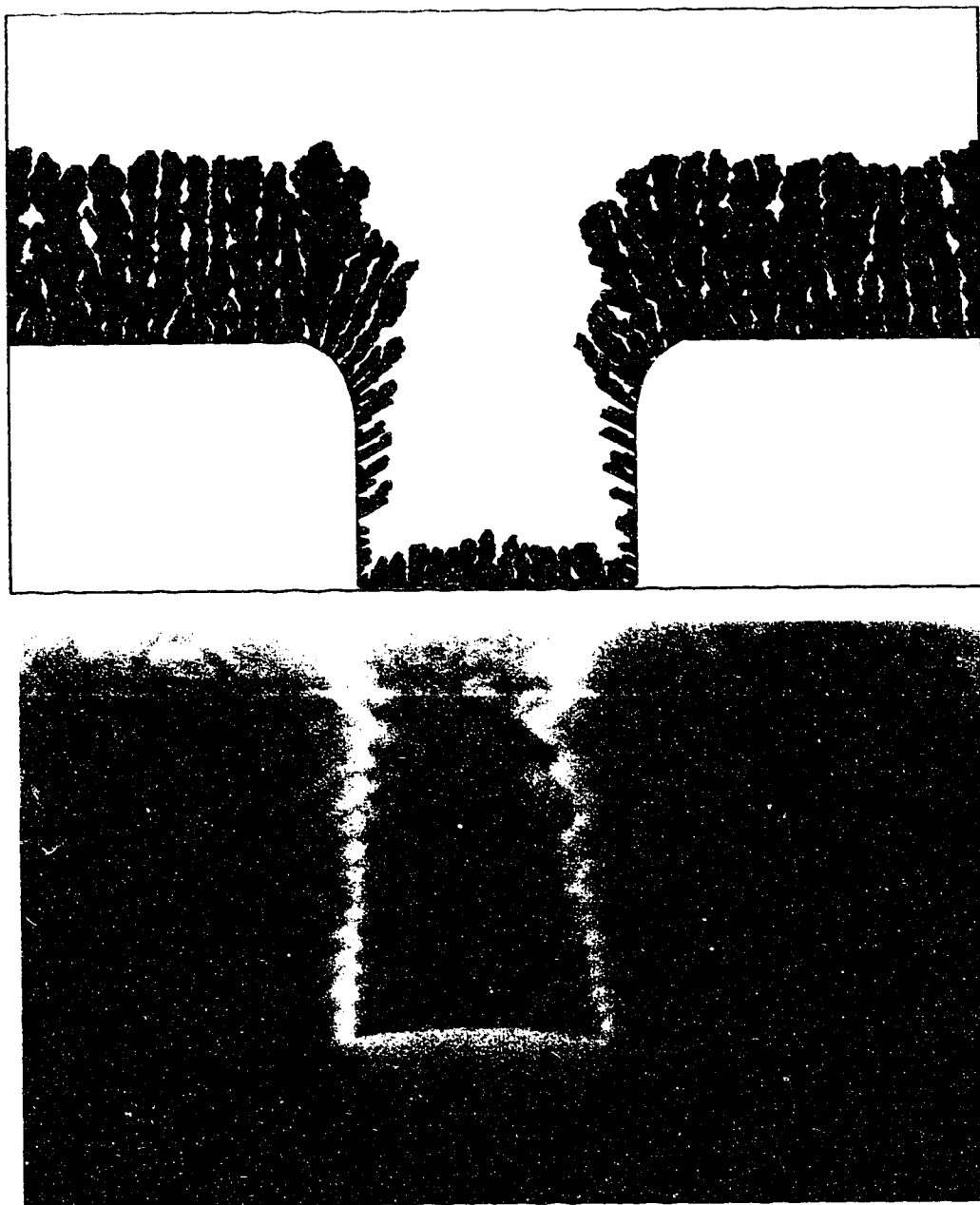


Figure A.59: Quasi-3d SIMBAD depiction of a film over a $1.1\ \mu\text{m}$ deep by $1.2\ \mu\text{m}$ wide via (top) and the corresponding experimental tungsten result (bottom).

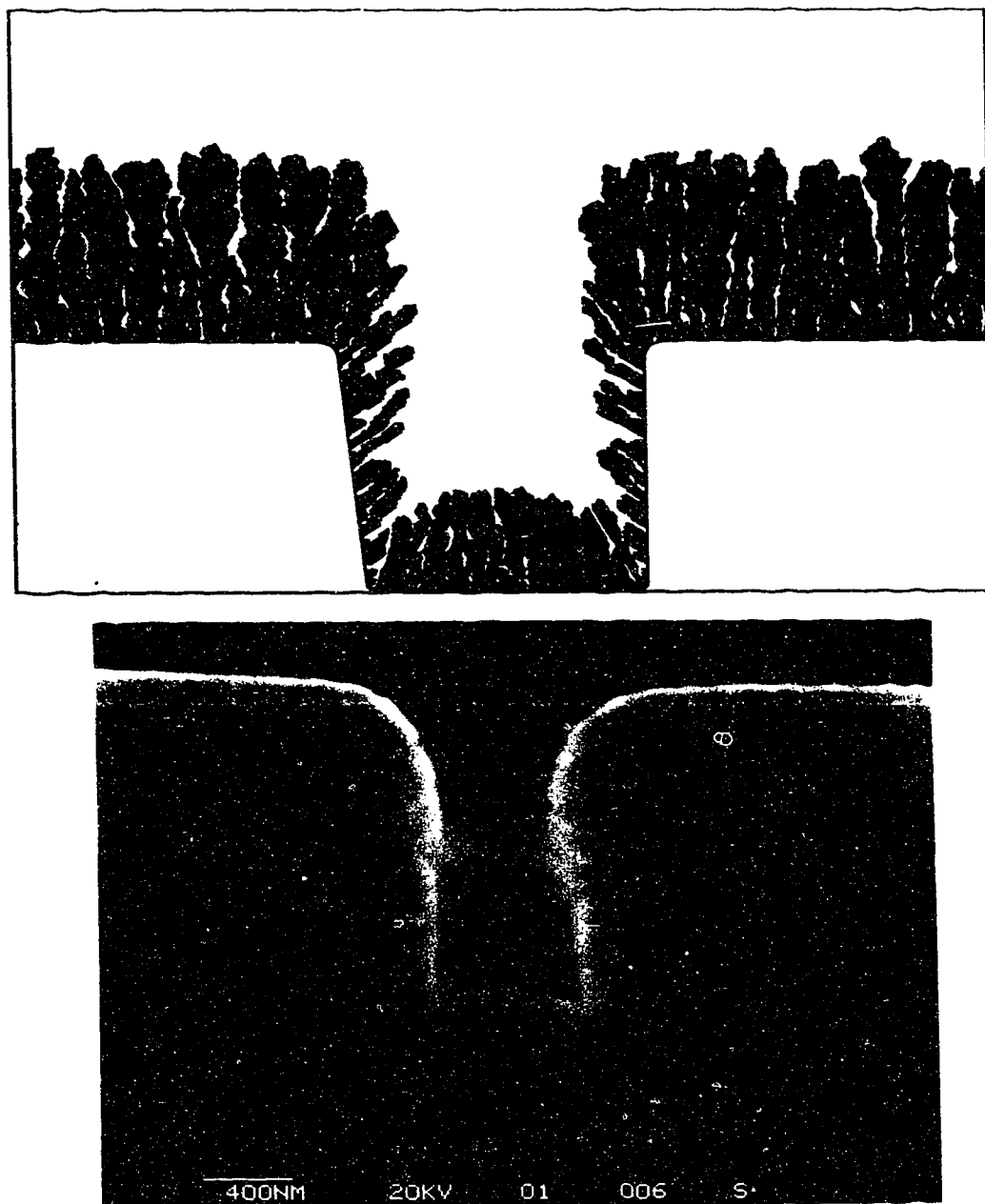


Figure A.60: SIMBAD depiction of a film over a $1.1\ \mu\text{m}$ deep by $1.2\ \mu\text{m}$ wide trench (top) and the corresponding experimental tungsten result (bottom).

Appendix B

SIMSPUD Program Organization

SIMSPUD consists of about 1000 lines of C code in four modules: one for the main program control and simulation routines, and one each for input/output, uniform random number generation, and user-specified distribution generation. Except for the uniform random generator (based on routines by Press *et al.* [100]), SIMSPUD was written by S.K. Dew.

The program is invoked by the command

simspud *fname*

where *fname* is the root name for the run parameter input file (*fname.spud*), and the angular, energy, and thickness output distribution files (*fname.ang*, *fname.E*, and *fname.thick*), as well as the summary output file (*fname.log*). The input file specifies the simulation parameter values in addition to the filenames describing the target erosion profile and the emission angular distribution functions.

The sequence of program execution is described in Figure B.61. The main loop is repeated until a specified number of particles have been generated or collected. The resulting output is a series of (x,y,dy) values in each of the output distribution files which is suitable for viewing with common graphics packages (or input into SIMBAD as in the case of *fname.ang*).

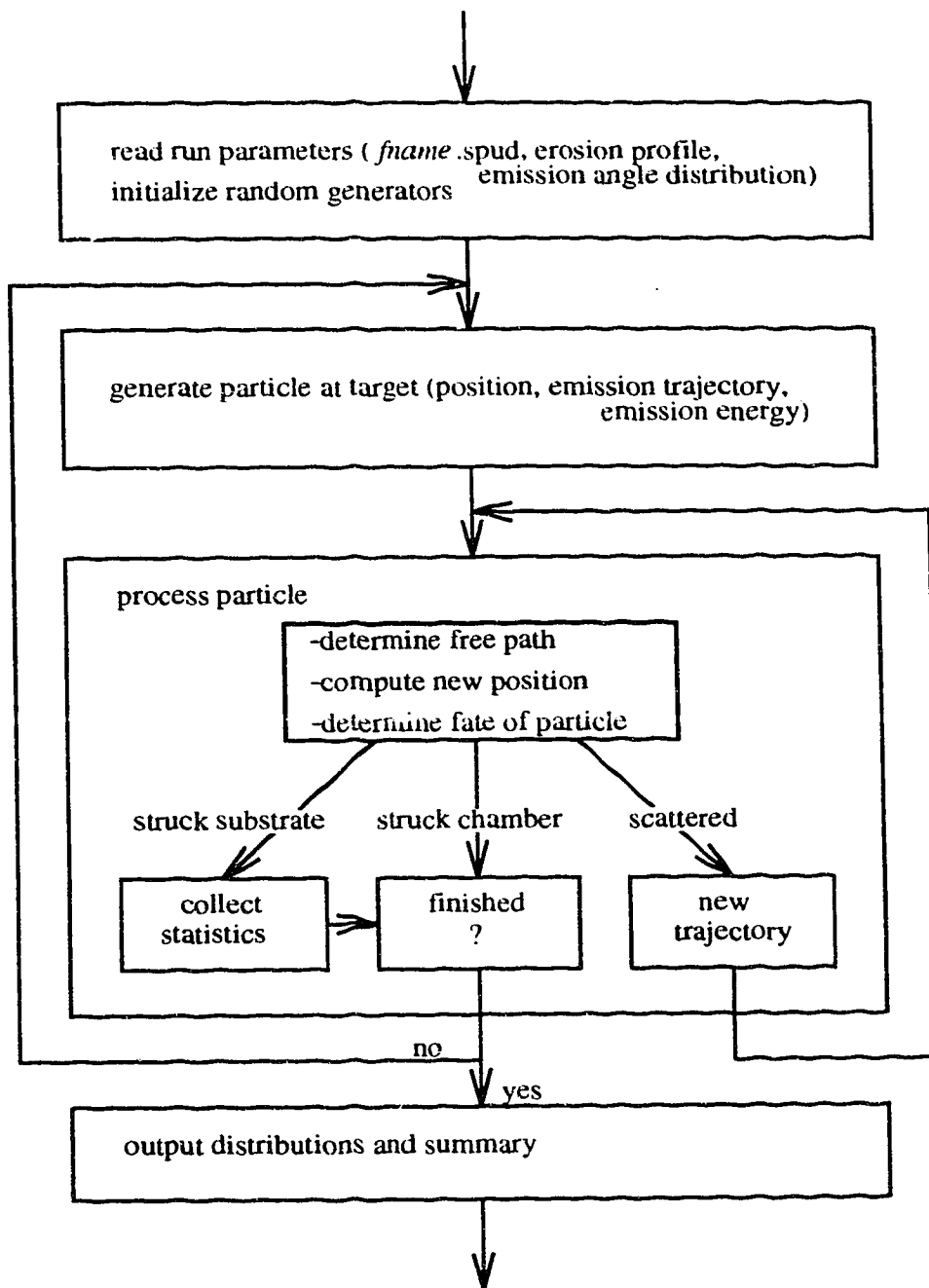


Figure B.61: Diagram of SIMSPUD execution.

Appendix C

SIMBAD Program Organization

SIMBAD consists of approximately 10000 lines of FORTRAN and C code, including auxiliary routines to translate output into PostScript format and to compute density profiles. The current version of SIMBAD is called *rec6* (revision 6 of a recursive surface diffusion algorithm) and has been primarily written by S.K. Dew and T. Smy but is based on the original (non-recursive) version written by M.J. Brett with assistance from R.N. Tait and K.L. Westra. It currently consists of 13 separately compiled files.

The program is invoked by the command

rec6 *fname*

where *fname* is the root name of the input files (the run parameters file, *fname.run*, the initial substrate profile, *fname.init*, and the incident angular distribution, *fname.ang*) and the output file (*fname.film*). Translation of the output to PostScript format (*fname.ps*) for viewing or printing is achieved by

plotfilm *fname*

and a density plot (*fname.dps*) is obtained by executing

plotdense *fname*

where *fname.parm* specifies a series of **.film** files for averaging and density computation parameters.

Appendix C. SIMBAD Program Organization

The sequence of SIMBAD execution is described in Figure C.62. As with SIMSPUD, the main loop is repeated until a specified number of particles have been generated or collected. Fates which depend on the type of disc (film, ion, or precursor), are indicated by different styles of lines (solid, dashed, or dotted, respectively). Common execution sequences are indicated by thick solid lines. The resulting output from SIMBAD is a series of positions of disc centres along with some summary statistics.

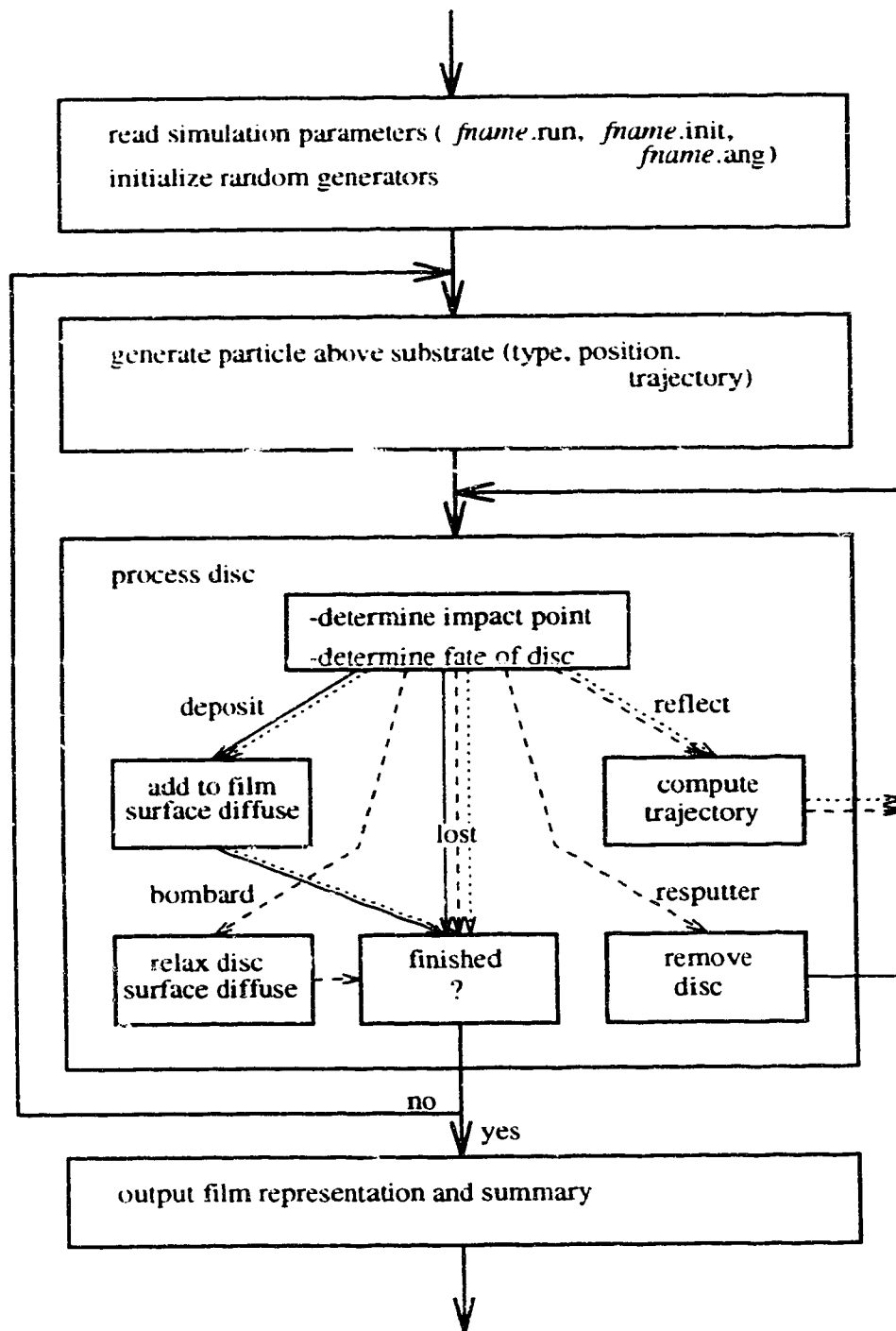


Figure C.62: Diagram of SIMBAD execution.